


MITSUBISHI HEAVY INDUSTRIES, LTD.
16-5, KONAN 2-CHOME, MINATO-KU
TOKYO, JAPAN

December 19, 2008

Document Control Desk
U.S. Nuclear Regulatory Commission
Washington, DC 20555-0001

Attention: Mr. Jeffrey A. Ciocco

Docket No. 52-021
MHI Ref: UAP-HF-08299

Subject: MHI's Partial Responses to the NRC's Requests for Additional Information on Topical Report MUAP-07008-P(0) "Mitsubishi Fuel Design Criteria and Methodology"

Reference: 1) Letter from the NRC (ML082760492) to Y. Ogata (MHI), "Mitsubishi Heavy Industries, Inc.-Request for Additional Information on Topical Report MUAP-07008-P, Revision 0, "Mitsubishi Fuel Design Criteria and Methodology" dated on November 20, 2008

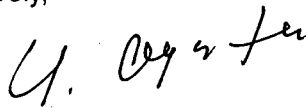
With this letter, Mitsubishi Heavy Industries, Ltd. ("MHI") transmits to the U.S. Nuclear Regulatory Commission ("NRC") partial responses entitled "MHI's Partial Responses to the NRC's Requests for Additional Information on Topical Report MUAP-07008-P(0) Mitsubishi Fuel Design Criteria and Methodology". In the enclosed document, MHI provides the responses for RAI's item 1 through 32, 36, 37 and 38 of those in Reference 1 within the allotted 30 day response time-frame that is given from the date of the formal RAI issuance. All other responses to the RAI's listed in Reference 1 will be provided on January 30, 2009.

As indicated in the enclosed materials, this document contains information that MHI considers proprietary, and therefore should be withheld from public disclosure pursuant to 10 C.F.R. § 2.390 (a)(4) as trade secrets and commercial or financial information which is privileged or confidential. A non-proprietary version of the document is also being submitted in this package (Enclosure 3). In the non-proprietary version, the proprietary information, bracketed in the proprietary version, is replaced by the designation "[]".

This letter includes a copy of the proprietary version (Enclosure 2), a copy of non-proprietary version (Enclosure 3), and the Affidavit of Yoshiki Ogata (Enclosure 1) which identifies the reasons MHI respectfully requests that all materials designated as "Proprietary" in Enclosure 2 be withheld from public disclosure pursuant to 10 C.F.R. § 2.390 (a)(4).

Please contact Dr. C. Keith Paulson, Senior Technical Manager, Mitsubishi Nuclear Energy Systems, Inc. if the NRC has questions concerning any aspect of this submittal. His contact information is provided below.

Sincerely,



Yoshiki Ogata,
General Manager- APWR Promoting Department
Mitsubishi Heavy Industries, LTD.

DOB1
NRO

Enclosures:

1. Affidavit of Yoshiki Ogata
2. MHI's Partial Responses to the NRC's Requests for Additional Information on Topical Report MUAP-07008-P(0) "Mitsubishi Fuel Design Criteria and Methodology" (proprietary)
3. MHI's Partial Responses to the NRC's Requests for Additional Information on Topical Report MUAP-07008-P(0) "Mitsubishi Fuel Design Criteria and Methodology" (non-proprietary)
4. CD1:"Attachment of Responses to RAI's item 1,9,12 and 18 of NRC Requests in ML082760492 (UAP-HF-08299 Rev.0)"

The files contained in this CD1 are listed in Attachment 1.

CC: J. A. Ciocco
C. K. Paulson

Contact Information

C. Keith Paulson, Senior Technical Manager
Mitsubishi Nuclear Energy Systems, Inc.
300 Oxford Drive, Suite 301
Monroeville, PA 15146
E-mail: ck_paulson@mnes-us.com
Telephone: (412) 373 - 6466

ENCLOSURE 1

Docket No.52-021
MHI Ref: UAP-HF-08299

MITSUBISHI HEAVY INDUSTRIES, LTD.

AFFIDAVIT

I, Yoshiki Ogata, being duly sworn according to law, depose and state as follows:

1. I am General Manager, APWR Promoting Department, of Mitsubishi Heavy Industries, Ltd ("MHI"), and have been delegated the function of reviewing MHI's US-APWR documentation to determine whether it contains information that should be withheld from disclosure pursuant to 10 C.F.R. § 2.390 (a)(4) as trade secrets and commercial or financial information which is privileged or confidential.
2. In accordance with my responsibilities, I have reviewed the enclosed "MHI's Partial Responses to the NRC's Requests for Additional Information on Topical Report MUAP-07034-P(0) FINDS: Mitsubishi PWR Fuel Assemblies Seismic Analysis Code" and have determined that portions of the report contain proprietary information that should be withheld from public disclosure. Those pages containing proprietary information are identified with the label "Proprietary" on the top of the page and the proprietary information has been bracketed with an open and closed bracket as shown here "[]". The first page of the technical report indicates that all information identified as "Proprietary" should be withheld from public disclosure pursuant to 10 C.F.R. § 2.390 (a).
3. The information in the report identified as proprietary by MHI has in the past been, and will continue to be, held in confidence by MHI and its disclosure outside the company is limited to regulatory bodies, customers and potential customers, and their agents, suppliers, and licensees, and others with a legitimate need for the information, and is always subject to suitable measures to protect it from unauthorized use or disclosure.
4. The basis for holding the referenced information confidential is that it describes the unique code and files developed by MHI for the fuel of the US-APWR and also contains information provided to MHI under license from the Japanese Government. These code and files were developed at significant cost to MHI, since they required the performance of detailed calculations, analyses, and testing extending over several years. The referenced information is not available in public sources and could not be gathered readily from other publicly available information. MHI knows of no way the information could be lawfully acquired by organizations or individuals outside of MHI and the Japanese Government.
5. The referenced information is being furnished to the Nuclear Regulatory Commission ("NRC") in confidence and solely for the purpose of supporting the NRC staff's review of MHI's Application for certification of its US-APWR Standard Plant Design.
6. Public disclosure of the referenced information would assist competitors of MHI in their design of new nuclear power plants without the costs or risks associated with the design of new fuel systems and components. Disclosure of the information identified as proprietary would therefore have negative impacts on the competitive position of MHI in

the U.S. nuclear plant market.

I declare under penalty of perjury that the foregoing affidavit and the matters stated therein are true and correct to the best of my knowledge, information and belief.

Executed on this 19th day of December, 2008.

A handwritten signature in black ink, appearing to read "Y. Ogata". The signature is written in a cursive style with a large initial "Y" and a long horizontal stroke extending to the right.

Yoshiki Ogata,
General Manager- APWR Promoting Department
Mitsubishi Heavy Industries, LTD.

Enclosure 3

UAP-HF-08299, Rev.0

**MHI's Partial Responses to the NRC's Requests for Additional
Information on Topical Report MUAP-07008-P(0) "Mitsubishi Fuel
Design Criteria and Methodology"**

December 2008
(Non Proprietary)

INTRODUCTION

This report documents MHI's responses to the NRC's Request for Additional Information (RAI) dated November 20 2008 concerning the Topical Report MUAP-07008-P(0) "Mitsubishi Fuel Design Criteria and Methodology".

RAI 1

The cladding strain criterion for normal operation in Section 3.2.2 states that "shall be less than 1% relative to the un-irradiated condition".

- a. Does this strain criterion include elastic plus plastic strain or just plastic strain?
- b. Provide an example FINE calculation of cladding strain for a limiting anticipated operational occurrence (AOO) event for the advanced pressurized-water reactor (APWR) including the input and output such that an independent calculation can be performed with the U.S. Nuclear Regulatory Commission (NRC) fuel performance FRAPCON-3 code for comparison purposes. Describe how power histories and AOO events are determined for this analysis. How is the burn-up level determined at which maximum cladding strain is calculated?
- c. Provide example calculations of cladding strain both at a 10 GWd/MTU burn-up level below and 10 GWd/MTU above the burn-up level where maximum strain is calculated in b above. This will demonstrate that the burn-up level selected results in calculated maximum cladding strain.

RAI 1 RESPONSE

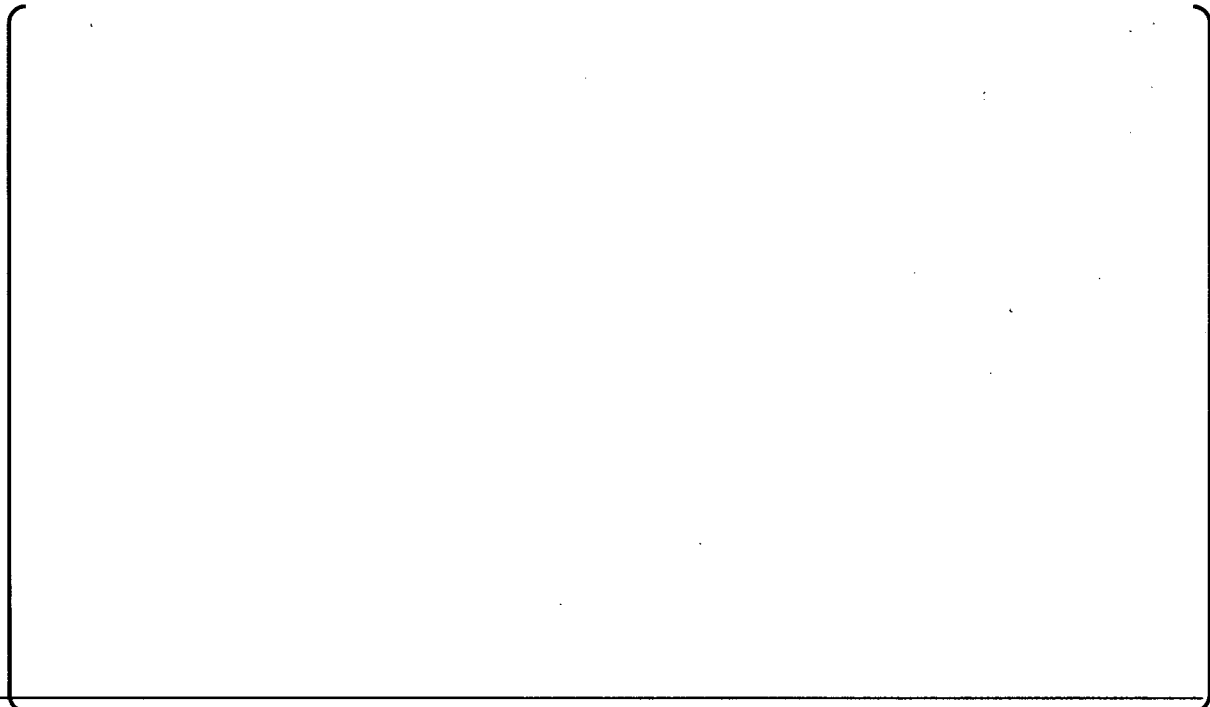
- RAI 1a

The strain evaluated for normal operation is the total strain, and includes the elastic and plastic strains.

The following description of the evaluation of the cladding strain criterion for normal operation is given in Section 3.8.2 of Reference 1a-1:

The cladding strain during normal operation is primarily due to PCMI and determined by the pellet densification, swelling and thermal expansion as well as by the cladding creep. The power variation during normal operation is generally very moderate, and the zirconium based alloy cladding readily deforms due to creep. There is therefore little possibility that the zirconium based alloy cladding could experience an unstable condition, with subsequent deformation beyond the one percent limit. Though the integrity of the cladding will be maintained until the cladding strain during normal operation reaches several percent, limiting the strain increment to 1% relative to the un-irradiated state is conservatively used as the criterion to limit PCMI during normal operation.

The following figure shows the result of a strain evaluation for normal operation. The data shown in the figure are the strains calculated at hot operating conditions. The strains at hot zero power conditions at EOL are also shown in the figure. The strain criterion for normal operation is evaluated using the difference between the BOL strain (0.0; as-built) and the EOL strain at the hot full power condition. Note that in this example the calculated strain is compressive, and that the criterion is a 1% limit for a tensile strain.



- RAI 1b

The FINE code input and output for the cladding strain evaluation will be provided via a CD-ROM. Sections 3.1.2, 3.2.1(2) and 3.8.2 of Reference 1a-1 describe the following regarding the power history, AOOs and burnup level considered in the evaluation of the cladding strain criterion during an AOO:

Some characteristic power histories are known to be most limiting with respect to margin to the fuel rod design limits. These limiting histories may be the highest or lowest power rods in a cycle or the highest burnup fuel rods in a cycle, depending on the fuel rod design criterion to be assessed. In general, a single fuel rod power history is not limiting for all fuel criteria, so a set of limiting characteristic power histories are typically assessed in the fuel rod design. These power histories bracket the range of fuel rod power histories for the fuel region, and provide the basis for assessing fuel rod performance relative to the established specified acceptable fuel design limits (SAFDLs).

Based on the Mitsubishi fuel rod design evaluation experience, the following power history types for each fuel type are selected and assessed as part of the process for defining the limiting rods for each criterion.

[]

The selection of the limiting AOO events, with respect to each fuel rod performance criterion addressed in the fuel system design, is described in "Transient and Accident Analysis" (Chapter 15 of Reference 1b-1). The assessment of the impact of the limiting event on the local power duty is determined by reactor core analysis. The limiting AOO events are selected in "Transient and Accident Analysis" (Chapter 15 of Reference 1b-1) from the perspective of fuel performance that is most important for each fuel system design criterion.

The design assessment of the AOO is performed using the local linear power density for the selected events determined in the reactor core analysis. The design maximum local linear power density (Local Power Limits: L.P.L.), consistent with the reactor core analysis results, are a function of the [] and the []
The L.P.L. are included in the fuel rod evaluation and are defined as follows:

$$\text{L.P.L.} = [\quad]$$

[]

For power transients associated with AOOs, the change in the cladding strain from normal operation to the maximum power of the AOO is evaluated as the total tensile strain change (elastic and inelastic). The strain change during the AOO is principally due to the pellet expansion resulting from the pellet thermal expansion and fission gas bubble swelling. The strain change is therefore independent of the hold time for the AOOs.

The evaluation of the cladding strain change during an AOO considers the irradiation behavior based on the power history for normal operation and the power condition associated with AOOs at every time step during fuel life, as shown schematically in Figure 1b-1. The limiting strain is determined as the maximum strain change during an AOO through the entire fuel rod irradiation history. Typically the maximum strain change occurs at mid-life or later, after the fuel-clad gap has closed at normal operation conditions.

Since the strain change during the AOO is principally due to the pellet expansion during the AOO (due to the pellet thermal expansion and fission gas bubble swelling), the most significant uncertainties for the strain change evaluation are those that tend to increase the pellet temperatures. The other significant uncertainties for the cladding strain change evaluation are those which tend to increase the PCMI during normal operation. Table 1b-1 shows results for the evaluation of the upper bound cladding strain change during AOOs, using the same uncertainty parameters as for the fatigue analysis in Section 3.6.2 of Reference 1a-1. The uncertainties that tend to increase the pellet temperatures are items (1), (2) and (8) in Table 1b-1 and the uncertainties that tend to increase the PCMI during normal operation are items (3), (4), (5), (6) and (7) in Table 1b-1. The total uncertainty in table 1b-1 is () for the UO_2 and $(U,Gd)O_2$ limiting rods, respectively, including model and manufacturing uncertainties.

Table 1b-1 Cladding strain change during AOOs evaluation, including uncertainties

unit: [%]

--

*No densification for this uncertainty evaluation

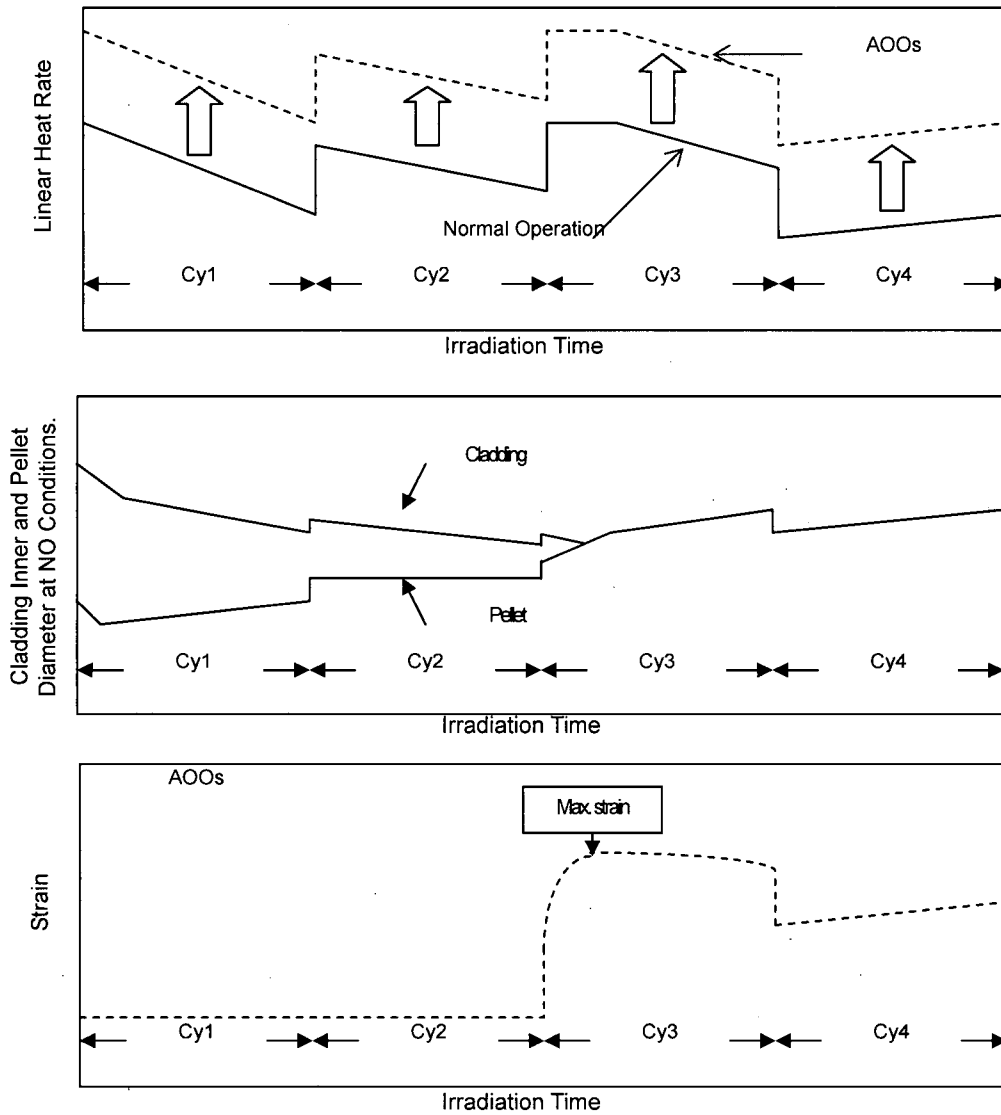


Figure 1b-1 Schematic illustration of the behavior of the cladding strain change during AOs as a function of irradiation exposure

Table 1c-1(1/2) Cladding strain change during AOOs results for the UO₂ limiting rod

Time Step	Rod BU (MWd/MTU)	Local LHGR (kW/ft)		Strain (%)	Remark
		NO	AOO	Best Estimated	

Table 1c-1(2/2) Cladding strain change during AOOs results for the UO₂ limiting rod

Time Step	Rod BU (MWd/MTU)	Local LHGR (kW/ft)		Strain (%)	Remark
		NO	AOO	Best Estimated	

Table 1c-2(1/2) Cladding strain change during AOOs results for the (U,Gd)O₂ limiting rod

Time Step.	Rod BU (MWd/MTU)	Local LHGR (kW/ft)		Strain (%)	Remark
		NO	AOO	Best Estimated	

Table 1c-2(2/2) Cladding strain change during AOOs results for the (U,Gd)O₂ limiting rod

Time Step	Rod BU (MWd/MTU)	Local LHGR (kW/ft)		Strain (%)	Remark
		NO	AOO	Best Estimated	

RAI 2

Section 3.2.3 states that Section III of the American Society of Mechanical Engineers pressure vessel standard will be used and that stress intensity will be determined based on unirradiated yield strength and ultimate tensile strengths for the fuel rod. Confirm that unirradiated yield and ultimate tensile strengths will be used for guide thimbles and grid spacers.

RAI 2 RESPONSE

Un-irradiated yield and ultimate tensile strengths of the guide thimbles are described as Re-Crystallized annealed Zircaloy-4 material in Sec B.1.3 of Appendix B in Reference 2-1 and are used in the stress intensity evaluations as described in Section 4.1.2 of Reference 2-1. A summary of the values is as follows:

- Yield Strength

Minimum yield strength of 35000 psi at room temperature is recommended by ASTM B353 Grade R60804. For the design values of elevated temperatures, the following equation is determined by Mitsubishi to meet the lower bound value at room temperature and the test data at hot conditions.

$$\text{Unirradiated design values} = \left(\begin{array}{l} \\ \end{array} \right)$$

(70 deg. F ≤ T ≤ 700 deg.F)

where

T: temperature (deg.F)

- Ultimate Tensile Strength

Minimum ultimate tensile strength of 60000 psi at room temperature is recommended by ASTM B353 Grade R60804. For the design values at elevated temperatures, the following equation is determined by Mitsubishi to meet the lower bound value at room temperature and the test data at hot conditions:

$$\text{Unirradiated design values} = \left(\begin{array}{l} \\ \end{array} \right)$$

(70 deg.F ≤ T ≤ 700 deg.F)

where

T: temperature (deg.F)

Above yield strength and ultimate tensile strength are used in the stress intensity evaluation for the control rod guide thimbles. For the grid spacers, the integrity is evaluated based on the load – deflection curve of the grid spacer based on impact test results for the grid spacer.

RAI 3

Section 3.2.4 describes the cladding fatigue methodology. In Figure 3.2.4-1, what is the significance of the line section labeled "Design curve corrected by max. mean stress"? Which curve is used in the FINE methodology?

RAI 3 RESPONSE

The US-APWR fuel rod design methodology uses the "Design curve corrected by max. mean stress" as the design curve. Figure 3.2.4-1 is identical to Figure 9 in the O'Donnell & Langer paper⁽³⁻¹⁾. The paper describes the basis for the maximum mean stress correction.

The cladding strain criterion for normal operation in Section 3.2.2 states that "shall be less than 1% relative to the un-irradiated condition".

RAI 4

The following questions address Fretting Wear, Design Criteria, in Section 3.2.5.

- a. A limit on fretting wear is provided in terms of percentage of wall thickness. In evaluating cladding stress/strain, is this reduction in the cladding wall thickness assumed?
- b. This section states that the level of fretting wear for a given design is based on both long term hydraulic-flow tests and analytical predictions. Were these flow tests performed on a complete assembly mockup of the APWR assemblies, and if not, what were the differences from an actual APWR assembly? Provide the range of flow conditions (rate and pressure) for these tests and the range of flow conditions in the APWR.
- c. How are the spacer spring forces determined for these flow tests? Provide the irradiation data used to determine spring force relaxation as a function of fast fluence used for the analytical input.
- d. Provide fretting wear predictions compared to actual ex-reactor flow fretting tests and observed in-reactor wear.

RAI 4 RESPONSE

- RAI 4a

The US-APWR fuel rod design methodology is in compliance with SRP Rev.3 Ch.4.2 II 1 A iii, which states that the stress and fatigue limits should assume the existence of the fretting wear. The fuel rod design methodology assumes a () reduction of wall thickness in the cladding stress, cladding strain change during AOOs and fatigue evaluations to meet this requirement. The cladding strain during normal operation is determined primarily by the pellet behavior and the affect of fretting wear is negligible.

In addition, the cladding wear is on the outer surface of the cladding, and affects only a small and local part of the cladding. Assuming that the fretting wear shape is a hyperbolic notch in a plane plate, the stress concentration factor has been calculated to be less than () for a notch with a total depth of () of the cladding wall thickness. The fretting wear therefore has a very small effect on the cladding stress evaluations.

The results of the US-APWR strain evaluations show that the effect of the () reduction of the cladding thickness is negligible for both normal operation and AOOs.

- RAI 4b

Flow tests with a full scale US-APWR fuel assembly have not yet been performed. However, a test using a bundle with 5x5 grid spacers and 4-span configuration has been conducted. The test result is shown in Section C.3.3 of Appendix C of Reference 4-1. The span lengths correspond to those of the lower three spans of a 17x17 conventional fuel assembly.

Several 5x5 grid spacers were prepared by cutting them from full-sized 17x17 Zircaloy-4 grid spacers. Test conditions for these tests were as follows.

Duration : 500 hours
Coolant : Water
Coolant flow velocity : 18 ft/sec (5.5 m/sec)
Temperature : Room temperature
Pressure : Atmospheric pressure

Temperature and pressure were selected to be room temperature and atmospheric pressure for simplicity of the test set-up and to perform comparative tests. Also due to the higher coolant density one would expect increased fuel rod response compared to that at reactor temperature and pressure.

For the fretting wear, the following parameters are primary.

- Span length
- Characteristics of the grid spacer
- Flow conditions of coolant

The span lengths in the US-APWR fuel assembly are essentially the same as those in the 17x17 conventional fuel assembly. For the grid spacers, the material and the dimple configuration of the middle grid spacers used in US-APWR are the same as those used in a conventional fuel assembly and the spring characteristics are very similar. The flow velocity is essentially identical to that experienced in conventional reactors. Therefore, the test results can be used in the fretting wear evaluation for the US-APWR fuel assembly.

A full scale flow test of the US-APWR fuel assembly will be performed in the 1st half of 2009 for confirmation. The test conditions are as follows and will be the same as in past tests except that the duration will be 1000 hours:

< Long term hydraulic test conditions for fuel rod cladding wear of the US-APWR >

Duration : 1000 hours
Coolant : Water
Coolant flow velocity : 18 ft/sec (5.5 m/sec)
Temperature : 300 deg.F (150 deg.C)
Pressure : Over 85 psi (0.59 MPa)

As a part of the hydraulic tests with US-APWR fuel assembly, the vibration response of fuel rods will be measured under various flow velocities up to the velocity mentioned above to be confirmed that no excessive vibration occurs in the fuel rods.

- RAI 4c

The grid spacer's spring force or cell size to be used in the long term hydraulic test are determined based on the relaxation characteristics of grid spacer springs as shown in Figure 4c-1 and 4c-2. The characteristics and figures are discussed in detail in subsection 4.4 of Reference 4-1. Based on these relaxation characteristics, the spring force for EOL conditions in the test is to be [] % of the initial spring force. In addition to EOL sized cells, BOL sized cells, just-contact cell size (0.374 in. /9.5 mm) and gapped cell conditions are also included in the test to obtain comparative data.

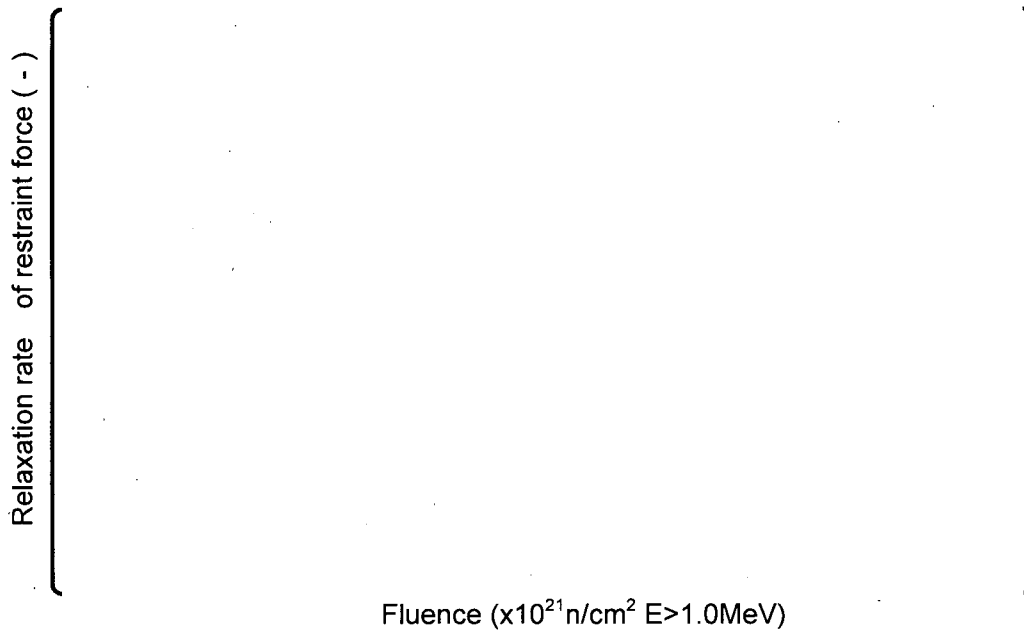


Figure 4c-1 Grid Spacer Spring Relaxation Rate (US Reactor Data)

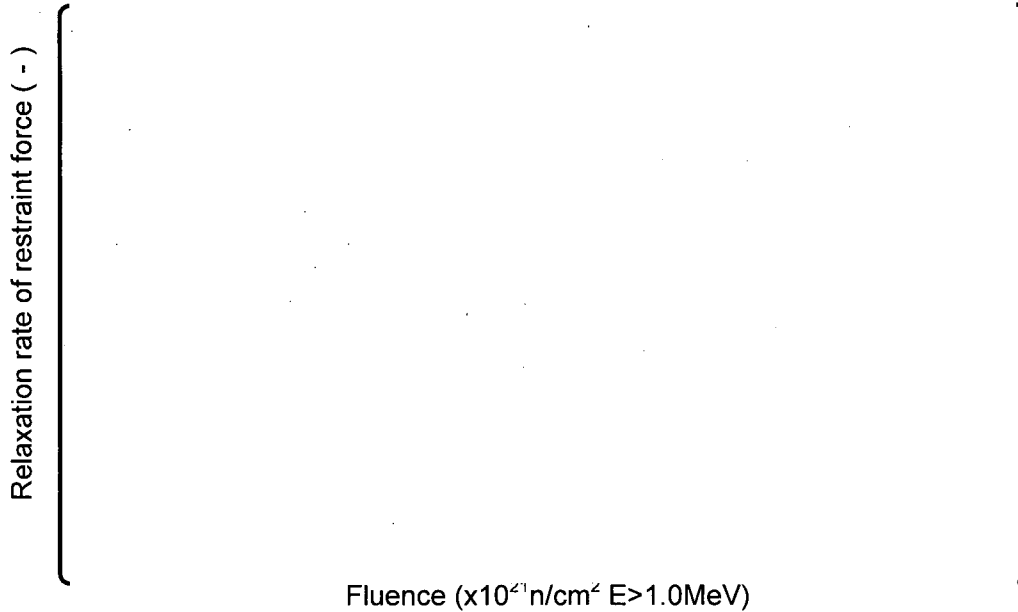


Figure 4c-2 Grid Spacer Spring Relaxation Rate (Japanese Reactor Data)

- RAI 4d

The fretting wear calculations for the ex-reactor tests with a 5x5 bundle and a 12-ft full scale fuel assemblies are shown together with the test results in section C.3.3 and C.4 of Appendix C of Reference 4-1, respectively.

According to the visual inspection of the fuel rods after the irradiation of burn-up of over 50 GWd/t, no fretting mark has been observed. The fuel rods were withdrawn from the fuel assembly with Inconel grid spacers irradiated in Japanese PWR plant. No significant wear was calculated for the fuel rod in the fuel assembly with Inconel grid spacers by the analysis at the burn-up level mentioned above as same with the result of visual inspection.

RAI 5

The following addresses cladding corrosion in Section 3.2.6.

- a. No limit is provided for cladding oxide thickness as Section 4.2 of the current Standard Review Plan suggests to prevent oxide spallation. Provide a proposed limit along with a justification for the limit. Also, the corrosion data supplied in the submittal for verification of the corrosion model only extends to a rod average burn-up of 56.6 GWd/MTU while it is requested that the code be applied up to rod average burn-up of 65 GWd/MTU. Provide additional oxide thickness data up to the requested burn-up level. (See RAI number 38)
- b. The MHI justification for the hydrogen limit is based on total elongation data to prevent brittle fracture provided in Section B.3.3.5. Cladding failure due to brittle fracture (failure prior to any measureable plastic strain), below the yield strength (60 percent to 85 percent of yield strength), has been observed in References 1 and 2 with measured total elongations between 1 to 3.6 percent from seven separate specimens (three axial tensile and four burst test specimens). These data suggest that total elongation is a poor measure of Zircaloy ductility to prevent brittle fracture. Comparison of mechanical test data from irradiated cladding to in-reactor RIA and PCI test failures suggest that uniform elongation is a better measure of strain capability and failure strain. Mechanical test data also suggest that mechanical test type (those that simulate the biaxial mechanical loads due to in-reactor PCMI) and gauge length/width is important for irradiated zirconium alloys (Reference 3).

Provide uniform elongation data versus hydrogen level (define how the hydrogen is determined) and versus fast fluence for irradiated cladding to verify that the cladding remains ductile at the proposed hydrogen limit. In the data provided, eliminate those data where hydrogen was artificially charged in the Zircaloy matrix resulting in a uniform hydrogen distribution through the cladding thickness.

Provide a description of the test methods and specimen geometry from which each set of the uniform elongation data were taken, as specimen geometry has a significant impact as discussed in Reference 3.

Also, the hydrogen data supplied in the submittal for verification of the hydrogen pickup model only extends to a rod average burn-up of 54 GWd/MTU while it is requested that the code be applied up to a rod average burn-up of 65 GWd/MTU. Provide additional hydrogen data up to the requested burn-up level. (See RAI number 38)

RAI 5 RESPONSE

- RAI 5a

Yield strength, UTS and total elongation data for irradiated Zircaloy-4 and ZIRLO are shown in Figure 5a-1. These data show that ZIRLO has essentially the same material properties as Zircaloy-4.

Figure 5a-2 shows the results of high-temperature tensile tests of irradiated cladding. These data show that the total elongation decreases as the hydrogen absorption increases up to approximately [] but this effect saturates at higher hydrogen concentrations and the total elongation exceeds the 1 % criterion for hydrogen concentrations up to []. This shows that the 1 % total strain criterion is conservative up to hydrogen concentrations of []

MHI data for ZIRLO™ cladding corrosion show no sign of oxide spallation for oxide thicknesses up to the maximum measured oxide thickness of [] as shown in Figure 5a-3. The Zr-4 oxide thickness data indicate no spallation for oxide thicknesses up to the maximum measured oxide thickness of [] and one instance of oxide spallation for low tin Zr-4, at an oxide thickness of []. MHI proposes to use an oxide thickness limit of [] which is consistent with the MHI hydrogen uptake limit of [] using the MHI value of [] for the hydrogen pickup fraction. The additional hydrogen data is described in the response of RAI number 38.

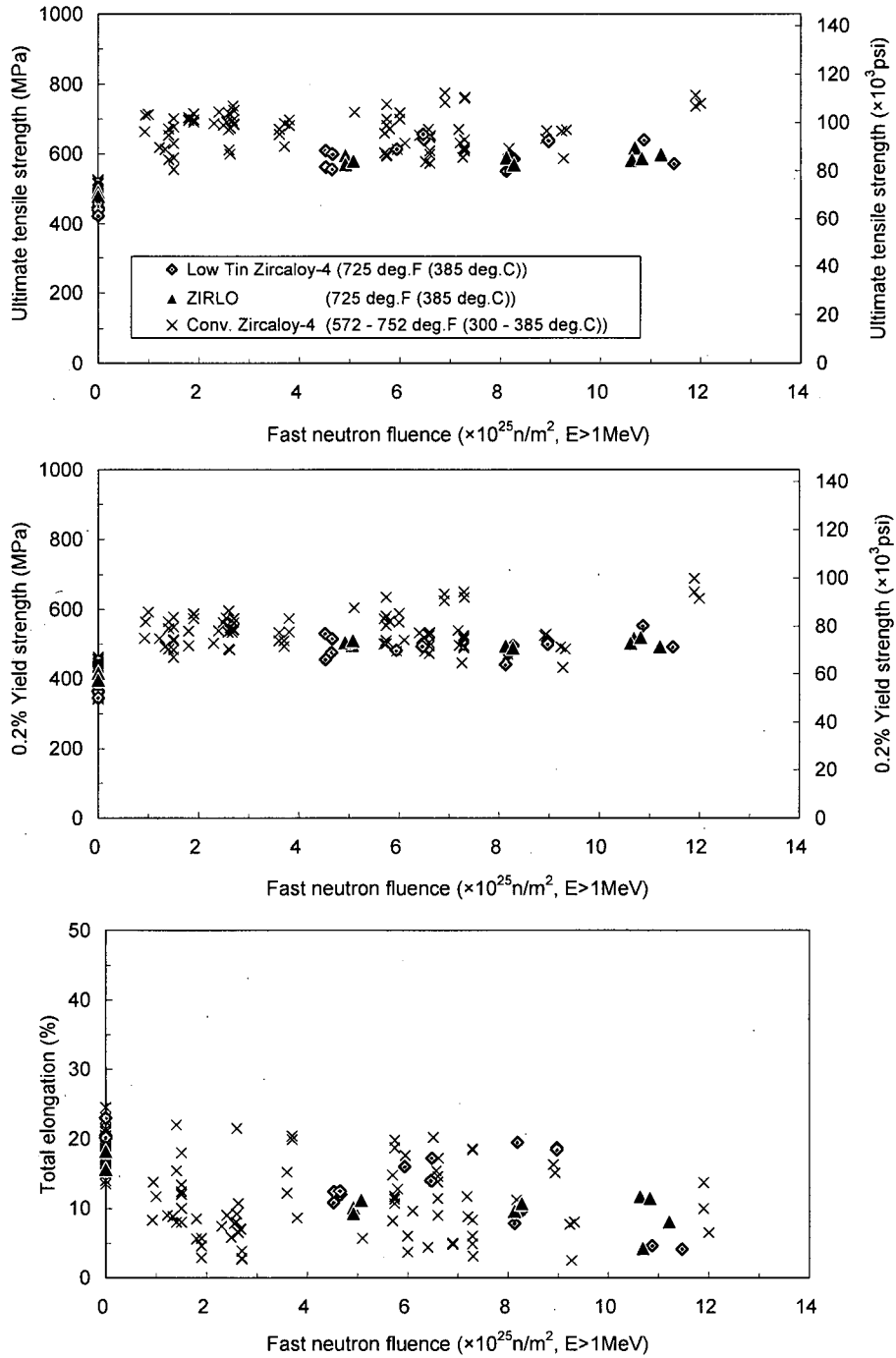


Figure 5a-1 Relationship between mechanical properties and fast neutron fluence

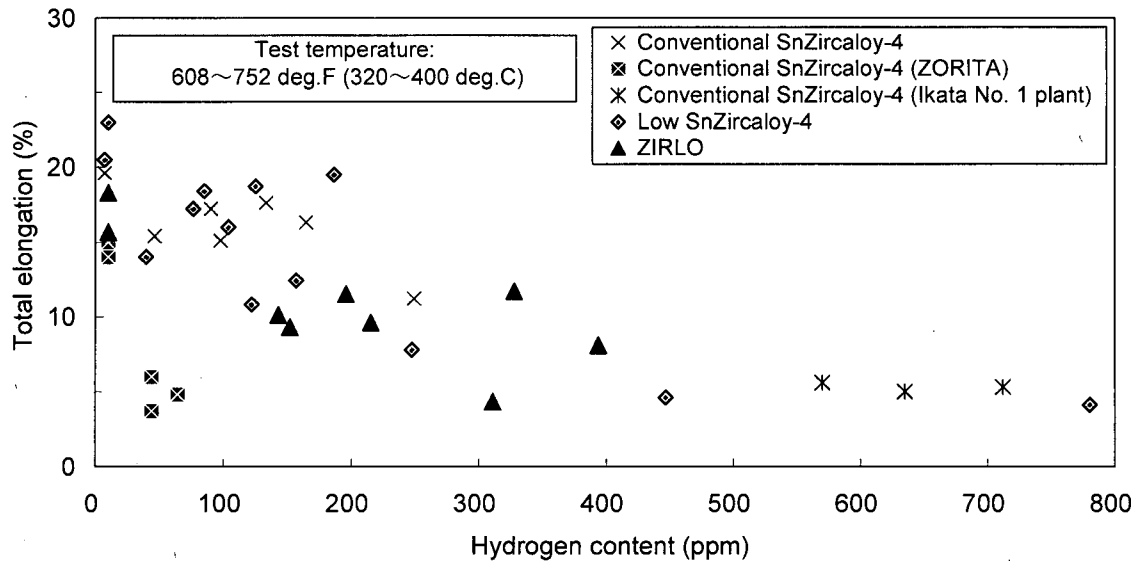


Figure 5a-2 Relationship between cladding hydrogen content and total elongation

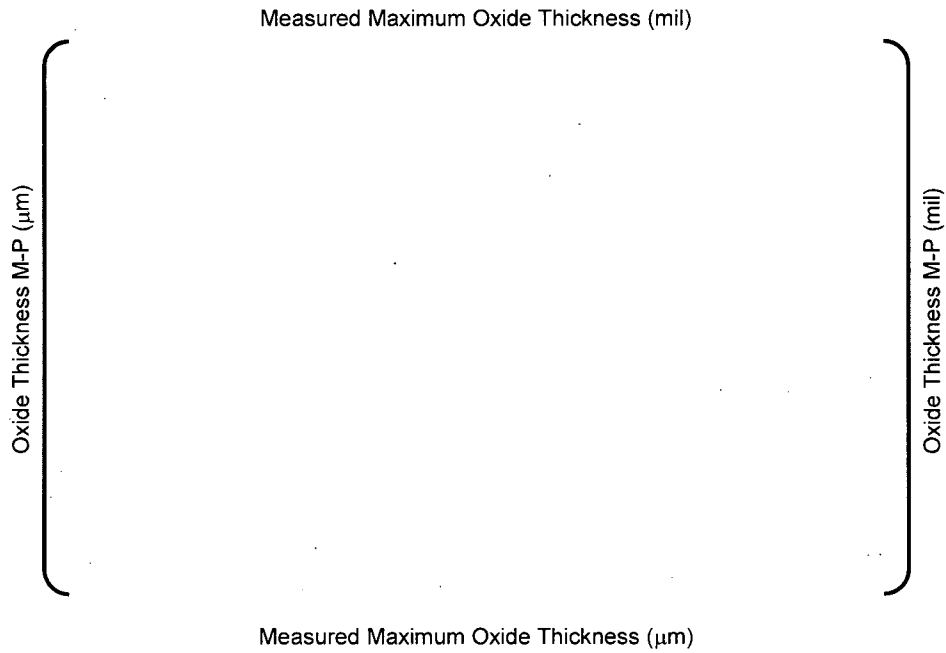


Figure 5a-3 Oxide thickness M-P versus measured maximum (peak) oxide thickness

- **RAI 5b**

Figure 5b-1 shows the irradiated cladding uniform elongation as a function of fast neutron fluence. Figure 5b-2 shows the irradiated cladding uniform elongation against average hydrogen content. Uniform elongation data for the cladding irradiated in Vandelllos 2, with rod burnups up to 74 GWd/MTU, with atypically high power in the last cycle, are included in both Figures.

These mechanical property data have been obtained from uniaxial tensile tests. Two types of tensile test specimen geometries have been used, and Figure 5b-3 shows the specimen geometries used for these tensile tests.

These data show that there is no significant degradation of the uniform elongation with increasing fluence or hydrogen content, with a minimum uniform elongation of slightly [] There is one Zirlo data point with a relatively lower uniform elongation at a fluence of 14.5×10^{25} n/m² and a hydrogen content of approximately [] is described in Appendix.

The hydrogen concentrations for the data with hydrogen contents of approximately [] shown in Figure 5b-2 have been obtained by the Studsvik Laboratory's hot vacuum extraction method. These hydrogen measurements were performed on specimens axially adjacent to the tensile specimens. Only when the hydrogen data adjacent to the specimen are not available, the hydrogen content has been determined from the measured oxide thickness, using the [] derived from the measured data shown in Figure 5b-4.

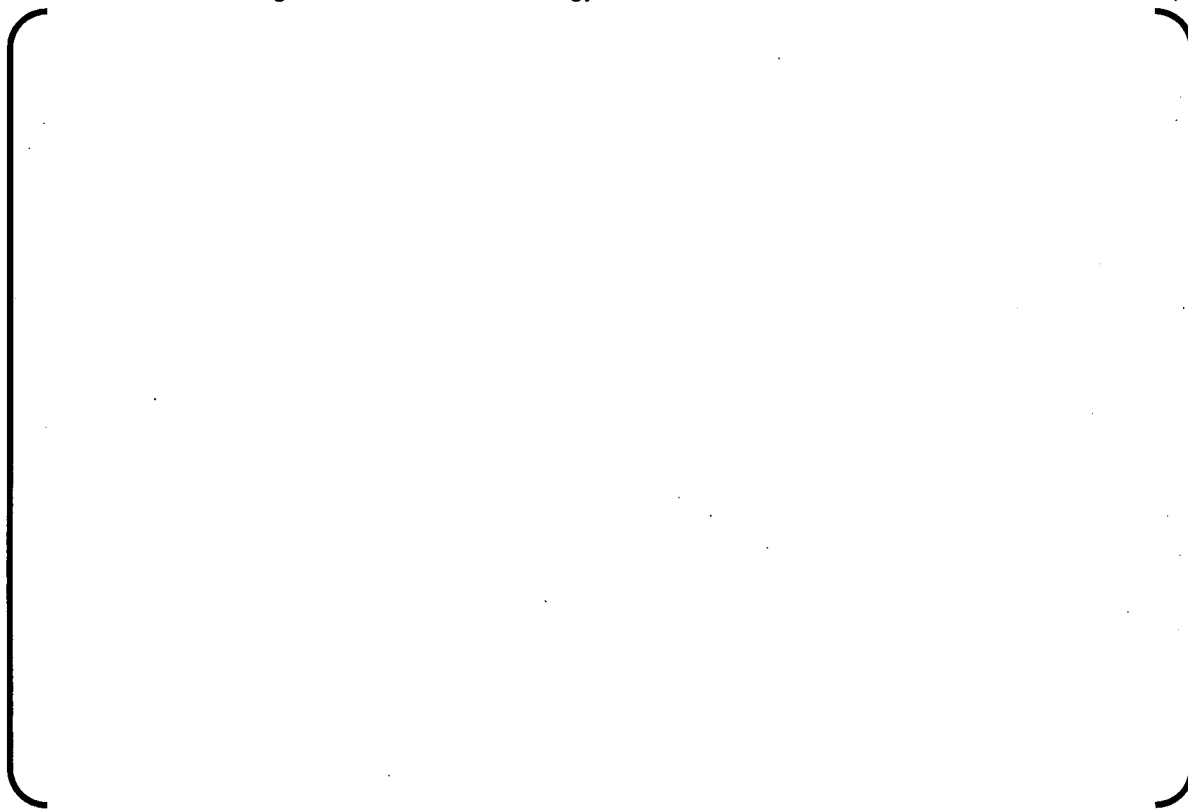
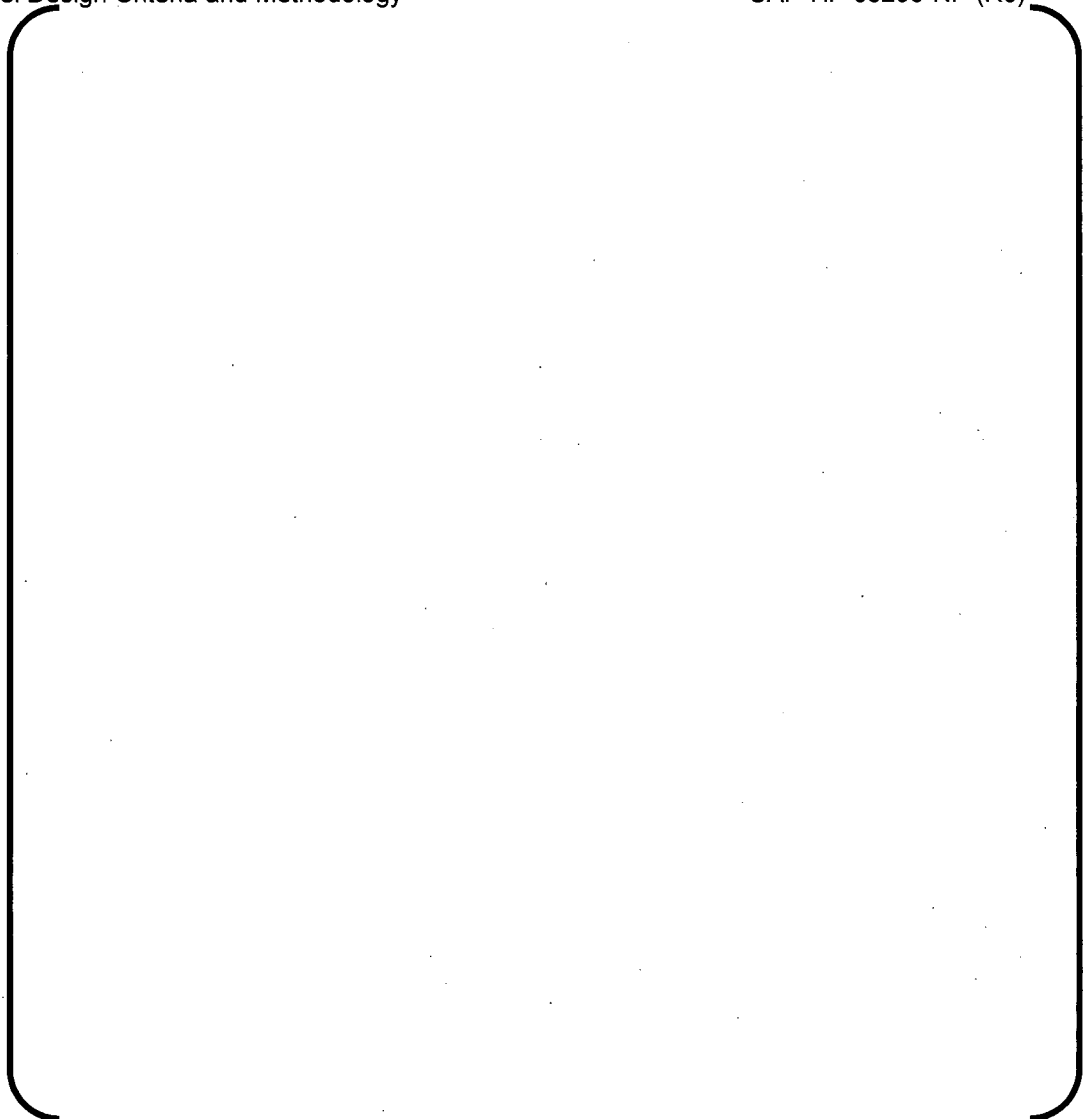


Figure 5b-1 Irradiated cladding uniform elongation vs. fast neutron fluence^(5b-1)



Figure 5b-2 Irradiated cladding uniform elongation vs. hydrogen content^(5b-1)



(b) Tube type specimen
Figure 5b-3 Axial tensile test specimen geometry

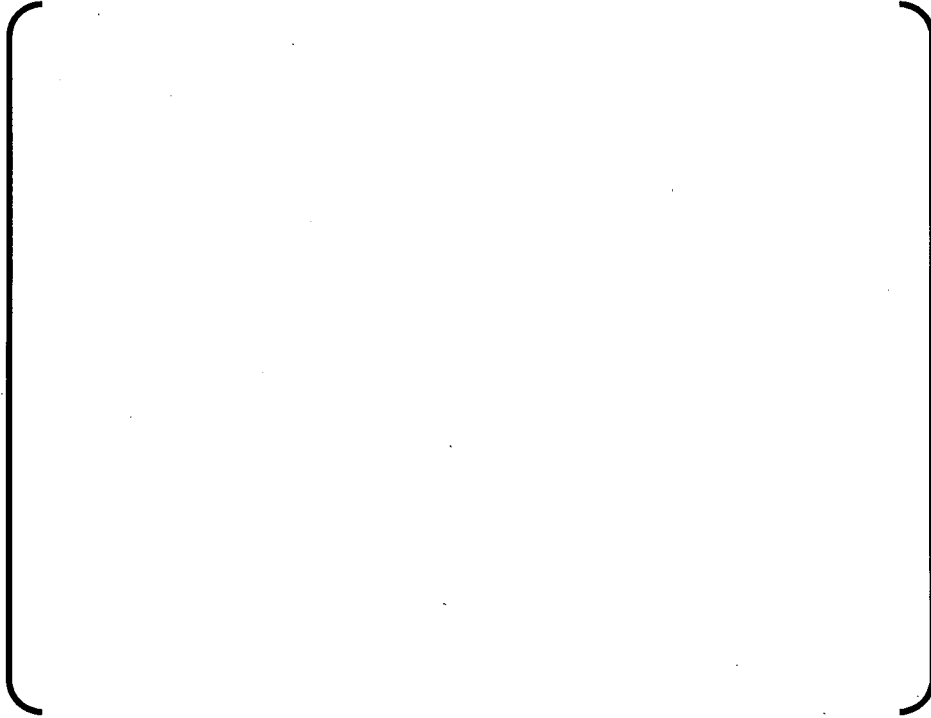


Figure 5b- 4 Hydrogen pick up data

Appnedix 5b

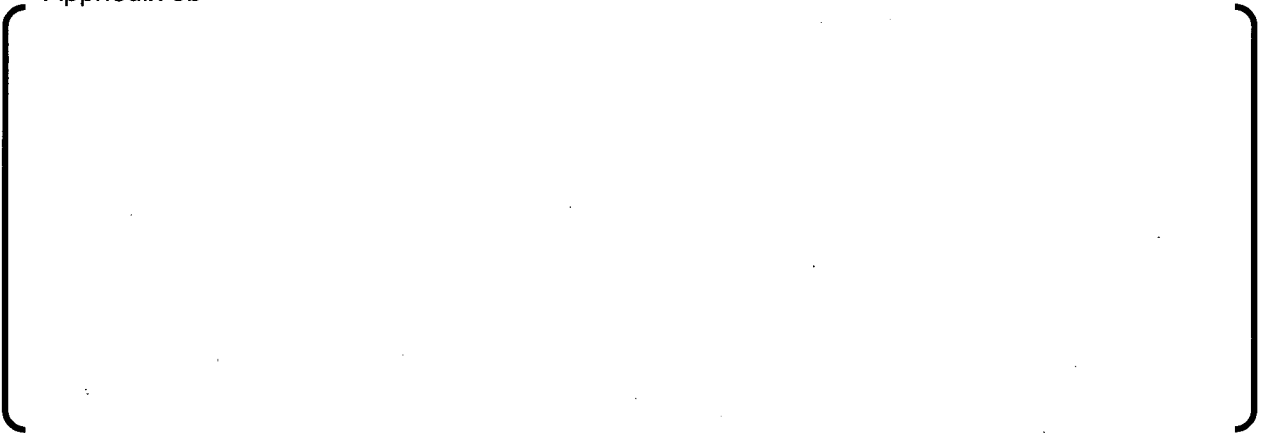
A large, empty rectangular area enclosed by a thick black bracket on the left and right sides, spanning most of the page's width. It appears to be a placeholder for content that is not present on this page.



Figure 5b- 5 Axial Tensile Test Specimen (ZIRLO, Vandellos 5CY)

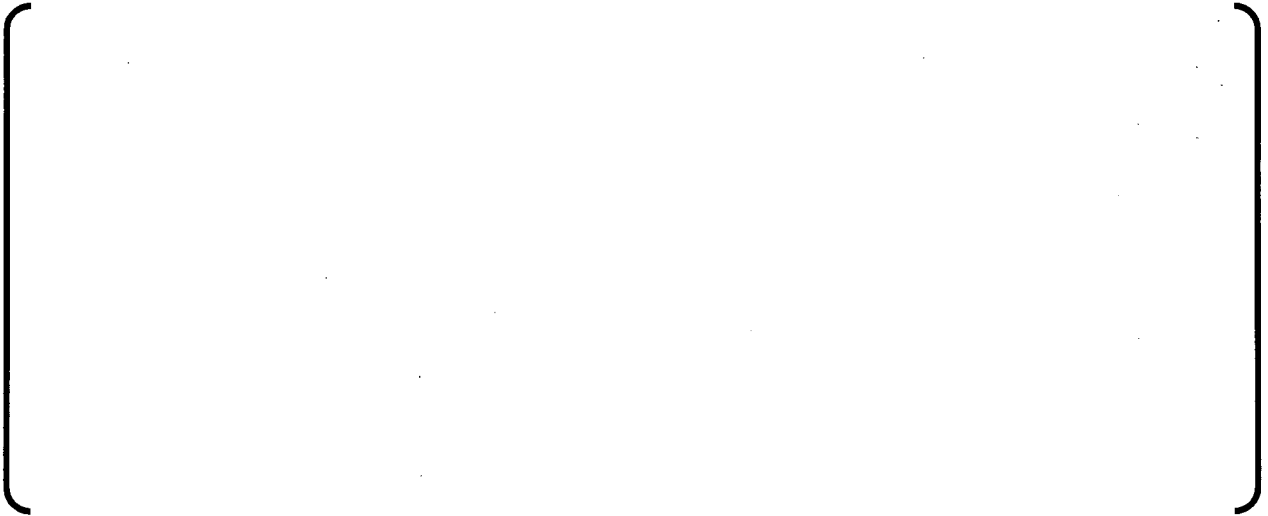


Figure 5b- 6 Hydrogen Distribution in 5cy irradiated ZIRLO cladding in Vandellos

RAI 6

Provide the data and correlation for APWR assembly growth as a function of burn-up or fast fluence used to determine APWR assembly growth and the uncertainties in this correlation. How do the designs from which these data were determined differ from that proposed for the APWR? In particular, what are the differences in the number of spacers, spacer springs and assembly holddown forces or any other fabrication/design differences that may impact rod or assembly growth? How are the assembly and/or rod growth correlations combined to determine that the gaps are adequate in Sections 3.2.7.1 and 3.2.7.2 with a high degree of confidence? If this is a statistical determination, provide a description and example of the statistical analyses used.

RAI 6 RESPONSE

1. Fuel assembly growth evaluation

The fuel assembly growth evaluation is discussed in detail in Section 4.3.2 of Reference 6-1.

The growth of the US-APWR assembly is evaluated using a design curve based on assembly growth data obtained from fuel assemblies in which only Inconel grid spacers are used. The design curve (B.E. + $k\sigma$) is a 95% probability at a 95% confidence level upper bound of the data and is shown in Figure 6-1.

Based on the conservative all Inconel grid fuel assembly upper bound growth, the predicted growth is approximately { } % at 60 GWD/MTU fuel assembly burnup, which is less than the assembly growth limit of { } % required to prevent the interference between the fuel assembly and the upper core plates.

The differences in design between US-APWR fuel assembly and the conventional fuel assembly that may impact fuel rod or fuel assembly growth are as follows.

- The number of grid spacers and material of grid spacers

The US-APWR fuel assembly has 9 Zircaloy-4 grid spacers and 2 Inconel grid spacers while the conventional fuel assembly in Figure 6-1 consists of 9 Inconel grid spacers. Since the relaxation of grid spacer spring force is considered to have more effect on the assembly growth than the number of spacers, the evaluation obtained by this data is conservative for the estimation of the upper bound US-APWR fuel assembly growth.

- Holddown force

The holddown force of conventional fuel assembly is { } lbf ({ } N) which compares closely to the { } lbf ({ } N) for US-APWR fuel assembly.

The hydraulic force of conventional fuel assembly is { } lbf ({ } N) is smaller compared with { } lbf ({ } N) for US-APWR fuel assembly. However, based on the assembly growth data from two types of fuel assemblies with different number of grid

spacers in Japanese PWR plant, the effect of hydraulic force on fuel assembly growth is negligible.

The dead weight of US-APWR fuel assembly is [] lbf ([] N). It is larger than that of conventional fuel assembly and suppresses the fuel assembly growth.

Therefore, the difference of holddown force is negligible for the assembly growth evaluation of the US-APWR fuel assembly.

2. Fuel rod growth evaluation

The fuel rod growth evaluation is discussed in detail in section 4.3.3 of Reference 6-1.

The initial total gap is designed to be sufficient to accommodate the maximum anticipated fuel rod growth in combination with the minimum fuel assembly growth, with appropriate consideration of manufacturing tolerances.

Figure 6-2 shows total gap change for various 17x17 fuel assemblies including ones with Zircaloy-4 spacer grids. The best estimate line and a [] level upper bound line are also shown in the figure.

For the US-APWR fuel, the evaluation curve is set by correcting for the extended fuel length and the thermal expansion difference between the fuel rod and the control rod guide thimble, since the data of the figure are obtained from the 12ft fuel assemblies under cold conditions and the required total gap is more limiting at hot conditions.

As calculated below, the total gap change for the US-APWR fuel is estimated to be [] inch ([] mm) at 60 GWD/MTU lead assembly burnup, which is less than the as-fabricated minimum total gap of [] inch ([] mm). This confirms that clearance between the fuel rods and the top and bottom nozzles is maintained throughout the US-APWR assembly lifetime.

- Total gap change of conventional 12-ft fuel assembly at 60GWd/t : [] mm
- Correction for extended over all length from 12-ft to 14-ft : [] x 14/12 = [] mm
- Thermal expansion of fuel rod : [] mm x [] % = [] mm \cong [] mm
- Thermal expansion of guide thimble : [] mm x [] % = [] mm \cong [] mm
- Total rod gap change for the US-APWR assembly : [] = [] mm \rightarrow [] inches

The impact of grid spacer spring force of US-APWR fuel assembly on rod bow is described in the response for RAI 7.

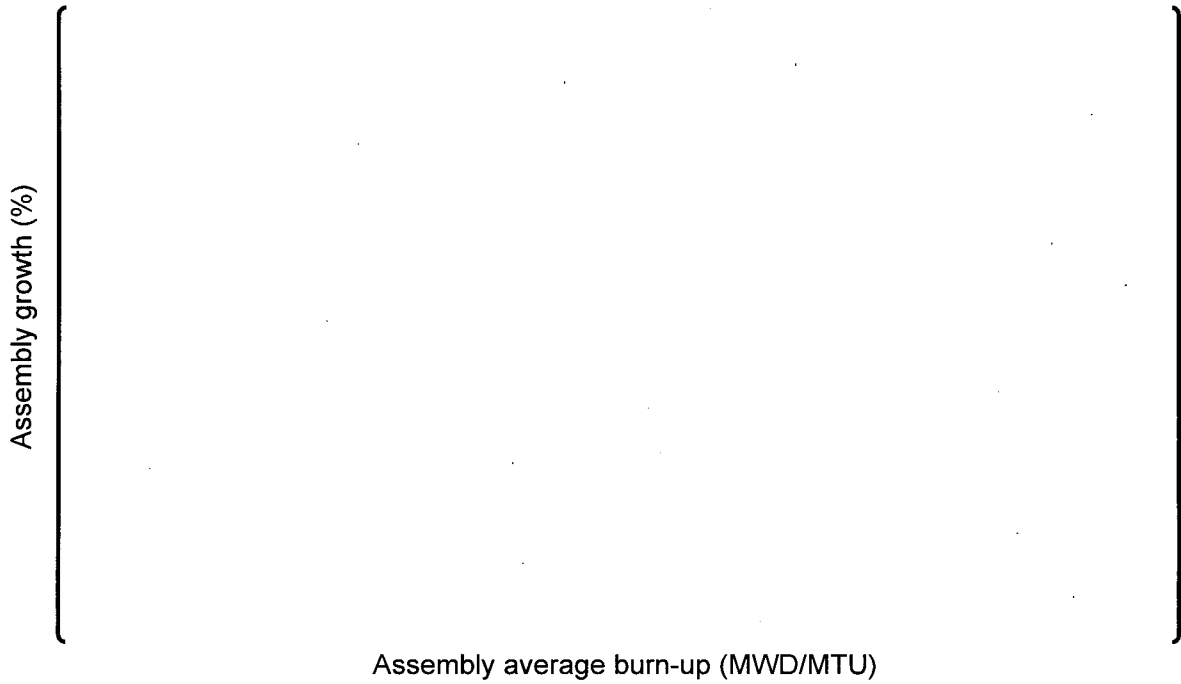


Figure 6-1 Mitsubishi 17×17 Fuel Assembly Growth Data with Inconel Grid Spacers

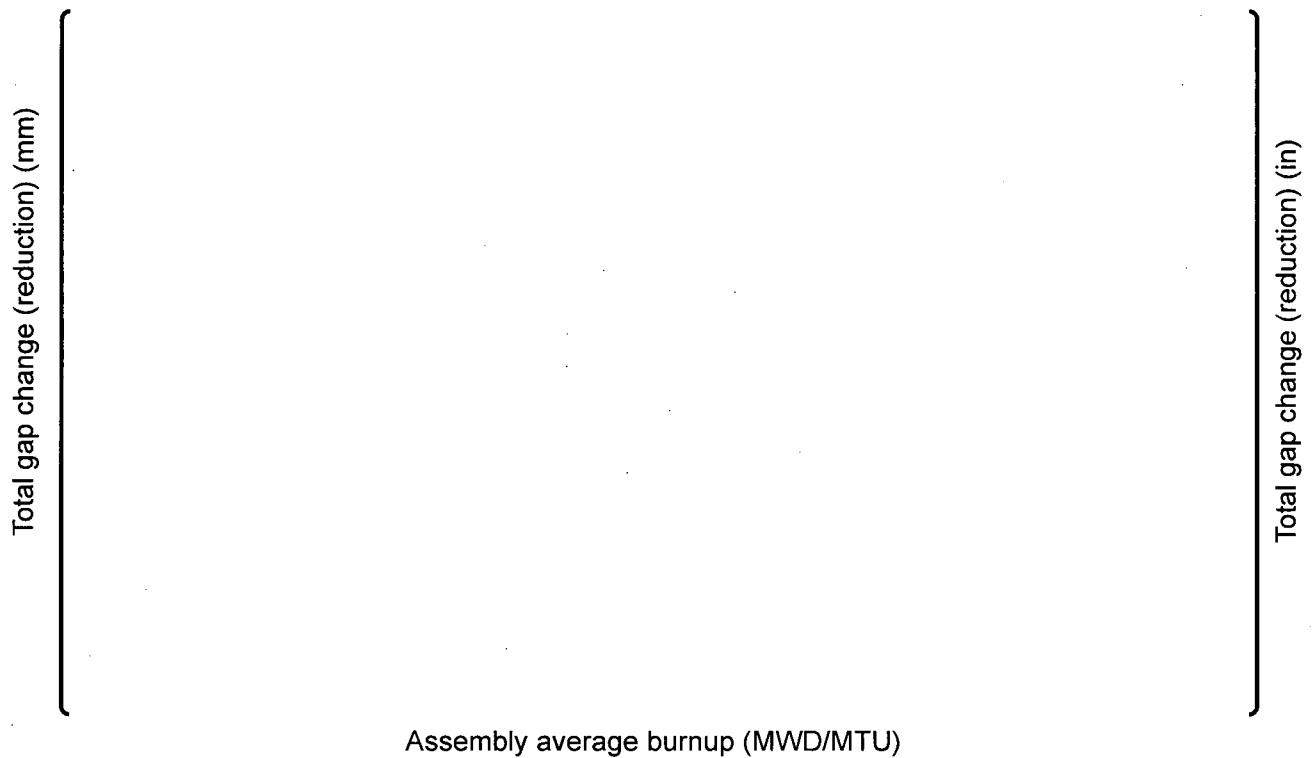


Figure 6-2 Total Gap Change of Mitsubishi 17x17 Fuel Assemblies

RAI 7

Provide the following;

- a) the rod bow data and correlation versus burn-up or fast fluence, and
- b) how the statistics were determined from this data used to estimate rod to rod spacing closure relevant to departure from nucleate boiling (Section 3.2.7.3). Are there design differences among the data that impact bow such as distance between spacers and grid spring forces? If so, indentify the design differences and their associated data. What are the grid spring forces for the APWR design and how do these compare to those spring forces from which the data were taken?

RAI 7 RESPONSE

- RAI 7a

The rod bow data is described in Section 4.3.1 of Reference 7-1.

The rod to rod spacing on all four faces of each fuel assembly has been image-analyzed from TV-tapes of irradiated fuel assemblies' visual inspections. The mean values and standard deviations of the rod to rod spacing are obtained for each span (the longitudinal space between consecutive grid spacers), and the rod to rod spacing closure rate is estimated from the worst span data. The design envelope for the rod to rod spacing closure at the worst span of each fuel assembly is established as a function of fuel assembly burnup.

Fuel rod bowing data from current Mitsubishi 17x17 fuel assemblies are shown in Figure 7a-1. The plotted data are derived from fuel assemblies with Inconel grid spacers and fuel assemblies uses Zircaloy-4 grid spacers. The relaxation rate is shown in Figure 4c-2.

- RAI 7b

The rod to rod spacing closure at EOL in the US-APWR fuel assembly is obtained from the data in Figure 7a-1. Those came from the conventional fuel assembly data with inconel grid spacers, and are considered to be conservative for the US-APWR design, because the fuel assemblies with inconel grid spacers tend to show larger fuel rod bowing due to a larger remaining grid spring force.

Each data point in Figure 7a-1 shows 0.3 percentile value for the each examined fuel assembly. The values are converted to the standard deviations for the DNB penalty estimation in the following manner.

1. Each 0.3 percentile value is converted to standard deviation by dividing by { } .
2. Obtain the linear fitting curve for the standard deviations vs. burnup by using a least square fitting method, and normalize each standard deviation data, dividing by the fitting curve value.

3. From the normalized standard deviations, a 95% probability at a 95% confidence level upper value is estimated by using Owen's k factor. Multiplying it to the fitting curve, the 95% probability at 95% confidence level upper value of the standard deviation of rod to rod spacing closure can be provided at an arbitrary burnup condition.
4. For the DNB penalty calculation, [] times of the above 95% probability at 95% confidence level value at EOL burnup condition is conservatively used as the standard deviation of rod to rod spacing closure.

It is assumed that the rod bowing of the US-APWR fuel can be estimated at the same level as the current Mitsubishi 17x17 fuel, for the following reasons:

- The data with Z2 type of Zircaloy-4 grid spacer in Figure 7a-1 shows effectively equal rod to rod spacing closure than is measured for 17x17 assemblies with Inconel grid spacers. The initial spring force for Inconel grid spacers is [] lbf ([] N) and is same as for Z2 type of Zircaloy-4 grid spacer. Z3 Zircaloy-4 grid spacer is used for US-APWR fuel assembly and the initial spring force is the same as for the Z2 grid spacer spring, and,
- Data shown in Figure 7a-1 are corrected for span length (distance between the grid spacers) of [] inch ([] mm), which is the span length averaged in the conventional 17x17 fuel assembly. Since the span lengths for the US-APWR fuel assembly are [] inch ([] mm), qualitatively speaking, the shorter span length leads to less rod bowing for the same bending moment condition.

The shorter span length and the grid spacer spring restraint force on the fuel rods in the US-APWR fuel assembly are adequately designed to reduce the fuel rod bowing and the consequent DNB penalty to an acceptable level.

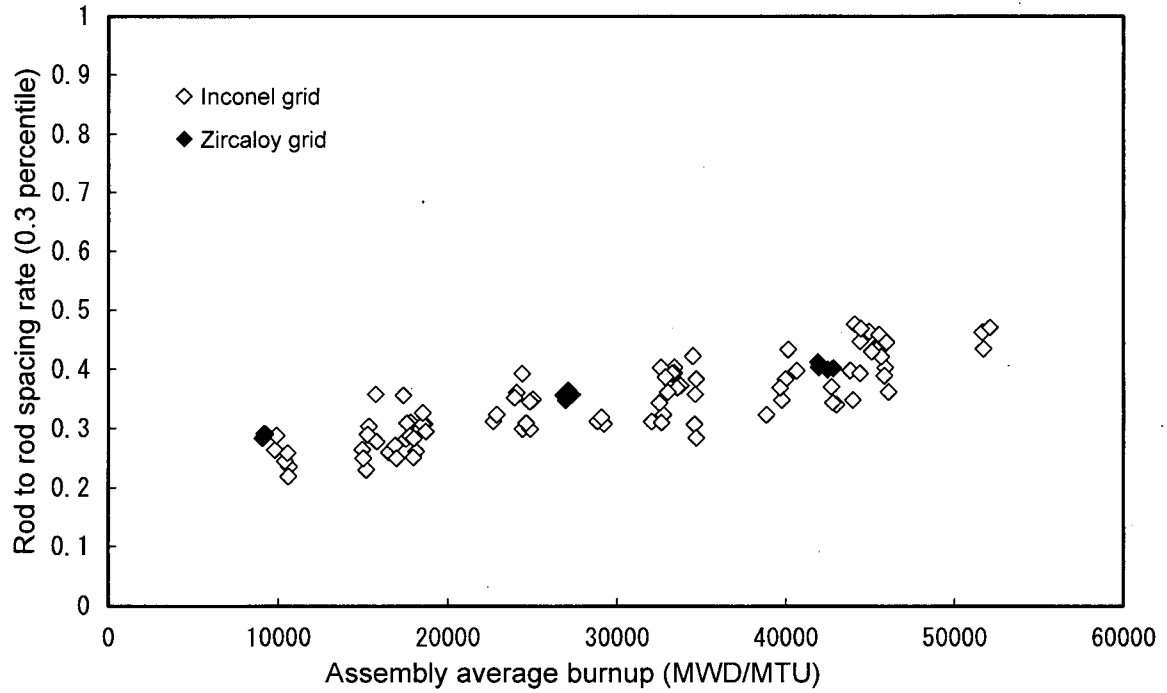


Figure 7a-1 Rod Bowing of Mitsubishi 17×17 Fuel Assemblies

RAI 8

Is there a limit on spacer grid irradiation growth for given designs (Section 3.2.7.4)? If so, what are the limits, and if not, provide justification for not establishing a limit. Provide data to demonstrate that grid spacer growth does not cause excessive interference for given designs.

RAI 8 RESPONSE

While the grid spacers shall maintain fuel rod to rod spacing during irradiation, they also contribute to locating the fuel assemblies in their correct core position. In addition, the dimensional change of the grid spacers shall not cause excessive interference with neighboring structures such as other fuel assemblies and neutron reflectors. The grid spacers' outer side growth data from foreign reactors are shown in Figure 8-1. To prevent the excessive interaction, one-sided growth length of the grid spacer is estimated based on the data and to be confirmed that the growth length is within half clearance in adjacent fuel assemblies. It is too conservative to consider that all fuel assemblies in core are end of life condition. Therefore, as discussed in Subsection 4.4.4 of Reference 8-1, the core average one-sided growth of the grid spacer for US-APWR fuel assembly is estimated to be [] inch () mm, which is within the limit of 0.02 inch (0.5 mm), the half clearance between adjacent fuel assemblies.

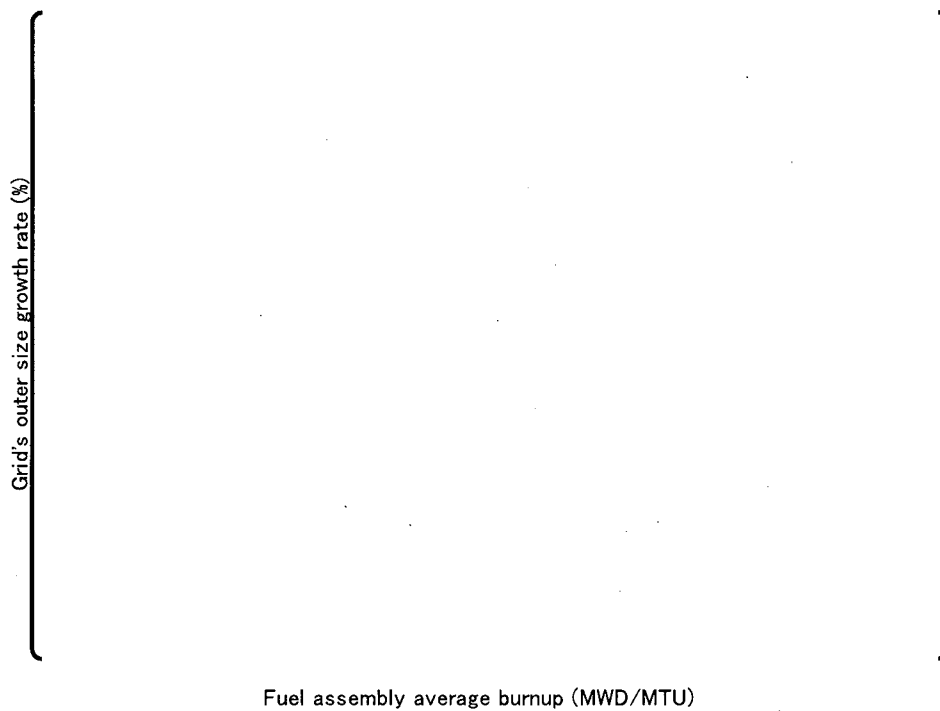


Figure 8-1 Grid spacer envelope growth data

RAI 9

Provide the following descriptions; a) how the cladding liftoff pressure limit is determined with the FINE code and b) how the FINE code is used to predict rod pressures to assure that no rod in the APWR fuel core will exceed this limit (Section 3.2.8). Specifically address the following:

- a. How is the liftoff internal pressure limit determined from the cladding creep and fuel swelling models including their uncertainties? Provide an example of this calculation. The fuel swelling model appears to overpredict the data on average. How is this overpredictive bias (non-conservatism) accounted for in this analysis? Justify the uncertainty used for fuel swelling based on model to data comparisons. Also, see RAI number 29 that relates to the estimated uncertainty for cladding creep.
- b. How are power histories determined for the rod pressure calculation (these should be determined based on the peak power rods)? Do they include AOO power events? Also, how is the limiting AOO event for the APWR determined for this analysis?
- c. Provide the F_Q and $F_{\Delta H}$ values (are they burn-up dependent?) as well as the average power rating for the APWR core in Kilowatts per foot (kW/ft). Provide a limiting power history for the APWR.
- d. Provide an example limiting FINE calculation of rod pressure for the APWR including the input and output such that an independent calculation can be performed with the NRC FRAPCON-3 code for comparison purposes.
- e. Describe how rod power, fabrication and FINE model uncertainties are included in the FINE prediction of rod pressure to provide assurance that this calculation will bound all rods in the core with a high probability that the pressure limit is not exceeded?

RAI 9 RESPONSE

- RAI 9a

The following description of the determination of the liftoff internal pressure limit is based on Section 3.3.2 (a) of Reference 1a-1:

The assessment of the liftoff pressure limit, using the FINE code, considers the power histories which give high internal pressures and high cladding creep rates, including the power history which gives the highest rod internal pressure. These power histories are based on the actual core analysis. The FINE code analyses determining the liftoff pressure limit analytically are performed by () () using these power histories. These pressure analyses determine the internal pressure when liftoff occurs for each power history, and the lowest internal pressure with liftoff is determined.

Using the FINE code results, the liftoff pressure is calculated as

$$(\text{Liftoff pressure}) = (\quad \quad \quad)$$

If liftoff occurs with no pellet-cladding contact, the liftoff pressure is determined from the change in the pellet-cladding gap, with the liftoff pressure given by the rod internal pressure when the gap starts to increase.

In the parameter survey to estimate the liftoff pressure, the () () and () () to create a hypothetical lift-off state. This survey matrix has significantly larger range than the fabrication specifications and model uncertainties. Nevertheless, due to the low power density and large plenum volume in the US-APWR, almost all of the rod internal pressures in the survey matrix are less than the system pressure. The best estimate minimum liftoff pressure is () which is the liftoff pressure calculated for the maximum burnup 3 cycle fuel rod using both a () and a () ()

[]

The calculated liftoff pressure decreases as () used in the calculation increases. The maximum () used in the determination of the liftoff pressure is (), which is significantly more than the US-APWR () fabrication specification, (). The bias in the liftoff pressure evaluation due to using () compensates for any non-conservatism due to using the best estimate fuel swelling rate, since the results for the liftoff pressure are significantly more sensitive to variations in () than to variations in the fuel swelling rate.

Uncertainties are accounted for in the liftoff pressure limit that is used for the US-APWR fuel design. The significant fabrication and model uncertainties which decrease the liftoff pressure are the uncertainties in the pellet swelling rate, the cladding creep rate and the cladding thickness. The effect of these uncertainties on the liftoff pressure is evaluated by varying the () as in the best estimate liftoff pressure evaluation, to determine the minimum liftoff pressure within the range of variation of these parameters.

The swelling rate affects when the pellet contacts with the cladding. Due to the low power density in the US-APWR core, for the hypothetical liftoff conditions () (), it is possible to reduce the fuel swelling rate to the point that pellet-cladding contact does not occur at any time in life for the rod with the minimum liftoff pressure. The swelling model uncertainty used in the liftoff pressure uncertainty evaluation is the smallest swelling rate for which pellet-cladding contact just occurs for the limiting rod. For the uncertainty evaluation shown below, this minimum swelling rate is () % $\Delta V/V$ per 10^{26} fissions/ m^3 , compared with the best estimate swelling rate of () % $\Delta V/V$ per 10^{26} fissions/ m^3 (9a-1). The uncertainty of the cladding thickness is based on the fabrication as described in Section 2 of Reference 1a-1.

The determination of the liftoff pressure uncertainties is shown in Table 9a-1. For the US-APWR fuel design, this process has determined that the liftoff pressure limit is conservatively bounded by (), the Japanese licensing value for the liftoff pressure limit.

It is confirmed that the rod internal pressure evaluated by the FINE code, with uncertainties, is below the liftoff pressure limit for all rods in the core. If rod internal pressure, including uncertainties, for any rod exceeds this limit, it is verified that liftoff does not occur for this specific power history. The applicability of this liftoff pressure limit is confirmed if there is any fuel design change in the fuel dimensions or materials.

Table 9a-1 US-APWR liftoff pressure uncertainty evaluation

--

- RAI 9b



The selection of the limiting AOO events is described in the response to RAI 1b.

The effects of power transients on the US-APWR rod internal pressure evaluation are small due to the low power density and large plenum volume. The results of the pressure analysis for power transients during both normal operation and AOOs show that the internal pressure in the limiting rod increases less than () compared with no-transient condition in the US-APWR. This evaluation has assumed that 1) an AOO event occurs at the end of life and that an operational transient event, such as axial power transient induced by a Xe oscillation, occurs at the end of each cycle and that 2) the hold time at the peak linear heat rate for the AOO event is () minutes.

- RAI 9c

The best estimate F_Q and $F_{\Delta H}$ values for the US-APWR equilibrium core are 1.82 and 1.52, respectively, as described in Appendix A of Reference 1a-1. Figure A-17 in Appendix A of Reference 1a-1 shows the burnup dependence of the US-APWR equilibrium core $F_{\Delta H}$. The limiting power history for the liftoff pressure criterion is the 2 cycle maximum burnup rod, as described in section 3.1.2 of Reference 1a-1 and as shown in Figure 3.1-1 in Reference 1a-1.

The average power rating for the US-APWR core is 4.65 kW/ft based on the densified active heated length as described in the Chapter 4 of Reference 1b-1.

- RAI 9d

The FINE input and output for the rod pressure evaluations are provided on the CD-ROM with the FINE input and output files for the response to RAI 1b.

- RAI 9e

The data provided in response to RAI 1b and RAI 9d give an example of the rod power histories used in the evaluation of the rod internal pressure criterion. In the US-APWR fuel design, the rod internal pressure is evaluated using the FINE code. The evaluation takes into account the uncertainties in the fuel fabrication and the fuel performance models. These uncertainties are considered statistically and the total uncertainty is evaluated by Square Root of the Sum of the Squares (SRSS) method at a 95 % probability at a 95 % confidence level. Table 3.3-1 in the Section 3.3.2 (a) of Reference 1a-1, shown below, shows the rod internal pressure evaluation results.

Table 3.3-1 Rod Internal Pressure Evaluation Results

A large, empty rectangular frame with rounded corners, positioned centrally on the page. It appears to be a placeholder for a table that has not been rendered or is otherwise missing from the document.

RAI 10

The NRC has not typically allowed fuel assembly liftoff in the United States such that the possible liftoff determined for the APWR for the pump-over-speed event may be an issue in this review (Section 3.2.9).

- a. Provide the results of the analyses for fuel assembly hydraulic lift forces described in Section 3.2.9 along with pressure drop data from flow tests of the APWR assembly at the flow rates applicable to this event.
- b. What are the resulting lift forces in the pump-over-speed event and how do they compare to the hold-down forces preventing movement of the assembly?
- c. How much is the assembly lifted from its seated position in this event?
- d. Provide the APWR analyses that demonstrate no inelastic deformation is present in the holddown spring for the pump-over-speed event.

RAI 10 RESPONSE

- RAI 10a, b, c, d

The fuel assembly liftoff evaluation is discussed in detail in Section 4.6 of Reference 10-1.

Since the overall length of the fuel assembly is increased by irradiation, the force of the holddown spring increases as it is irradiated. Consequently, the function of the holddown spring to prevent the fuel assembly liftoff is evaluated in the non-irradiated state where the spring force is the smallest. A mechanical force balance calculation, considering the fuel assembly weight, the holddown force, the hydraulic lift force and the buoyant force, is used to determine that the fuel assembly does not experience liftoff at the cold startup condition at the beginning of life.

Additional plastic deformation of the holddown spring does not occur, as long as the deflection of the holddown spring due to the liftoff at pump-over-speed condition is not beyond the maximum deflection at the cold startup condition. This is verified by the same mechanical balance calculation as used for normal operation and AOOs

- Function of the Holddown Springs

The holddown springs keep the fuel assembly from lifting off due to upward coolant flow during normal operation. The required force is the lift force plus the buoyancy minus the assembly weight. There is a large deflection of the holddown spring and hence there will be plastic deformation of the spring. The detailed behavior of the holddown spring is described below.

Figure 10-1 illustrates the change in holddown spring deflection for reactor conditions.

- Cold Condition

The upper core plate is lowered into position and bears on the fuel assembly, after the assembly has been positioned on the lower core support plate. The deflection of the spring, δC in Figure 10-1, is the difference between nominal overall length of the US-APWR fuel assembly including the holddown spring height and the distance from upper core plate to lower core support plates. The deflection of the spring with plastic deformation is expressed as point (a) in Figure 10-2.

- Hot Condition

The assembly length and the distance between the upper core and lower core support plates both increase due to thermal expansion in the hot condition. The thermal expansion of the fuel assembly is due to the expansion of the Zircaloy-4 control rod guide thimbles. Since the thermal expansion of the stainless steel core internals is greater than the Zircaloy-4 thermal expansion, the increase in length of the fuel, A in schematic diagram (a) in Figure 10-1, is less than the increase in the distance between the core plates, B in schematic diagram (b) in Figure 10-1. Hence the holddown spring deflection in the hot condition, $\delta H = \delta C - (B - A)$, point (b) in Figure 10-2, is less than it is in the cold condition. The force of the spring after it has experienced plastic deformation decreases linearly with a decrease in the deflection. The spring constant also decreases in the hot condition due to the decrease of the Young's modulus of the Inconel-718 spring as the temperature increases. Accordingly the load in the hot condition changes from point (a) to point (b) in Figure 10-2.

In addition, in the hot condition the lift and the buoyancy force both decrease due to the decrease of the coolant density. The decreased spring force in the hot condition is still large enough to prevent assembly liftoff.

Quantitative results for the force balance on the assembly at cold and hot conditions are given in Table 10-1. These quantitative results confirm that fuel assembly liftoff does not occur at the cold and hot conditions.

- Pump-Over-Speed Condition

If the fuel assembly lifts off due to the increase in flow at the pump-over-speed condition, the deflection of the springs will increase. As long as the deflection does not exceed point (c) in Figure 10-2, there will be no additional plastic deformation of the holddown springs.

Most realistic and probable evaluation results for the pump-over-speed condition are shown in Table 10-2. The lift-off height is shown as "L" in Figure 10-1. This value is obtained by dividing the additional spring force at the pump-over-speed condition by the spring stiffness as follows.

- Additional spring force at pump-over-speed condition:

$$\begin{aligned} &= \text{Downward spring force at pump-over-speed} - \text{Holddown force at hot full power} \\ &= \left[\quad \right] - \left[\quad \right] = \left[\quad \right] \text{ lbf} \quad \left(\left[\quad \right] \text{ N} \right) \end{aligned}$$

- The holddown spring stiffness = $\left[\quad \right] \text{ lbf/inch} \quad \left(\left[\quad \right] \text{ N/mm} \right)$

- The lifted height = $\left[\quad \right] = \left[\quad \right] \text{ inch} \quad \left(\left[\quad \right] \text{ mm} \right)$

As the result of the evaluation, the fuel assembly will liftoff at pump-over-speed conditions. The resulting deflection of the holddown springs during a pump-over-speed is less than the deflection at cold conditions, point (c) of Figure 10-2, and therefore there will be no additional plastic deformation of the holddown springs. The influence of lift-off on RCC insertion is discussed below.

Confirmation of the holddown force evaluation above will be obtained from the hydraulic test using the US-APWR mockup fuel assembly. The test is planned for the first half of 2009.

As shown in Figure 10-3, the lift-off height is smaller than the length of the critical diameter of the fuel guide pin and therefore the fuel assembly lateral position is maintained.

Therefore, the liftoff of the fuel assembly has no influence on the coolable geometry of the core and the insertion of control rods for safe reactor shutdown.

Table 10-1 Holddown Spring Evaluation at Cold and Hot Conditions

Unit: lbf (N)

Condition	Upward force*		Downward force			Evaluation
	Hydraulic lift force	Buoyancy	Dead weight	Required force in holddown spring	Holddown force per Assembly (Force per spring x 4 springs per assembly)	
	L	B	W	$R = L + B - W$	F	
Cold startup	[]					
Hot full power						

* Uncertainties in assembly shape and evaluation are included.

Table 10-2 Holddown Spring Evaluation at Pump-over-speed Condition

Unit: lbf (N)

Condition	Upward force*		Downward force		Limit force for no additional plastic Deformation**	Evaluation
	Hydraulic lift force	Buoyancy	Dead weight	Spring force		
	L	B	W	$R = L + B - W$		
Pump-over-speed	[]					

* Uncertainties in assembly shape and evaluation are included.

** Limit force is corresponding to the point (c) in the Figure 10-2.

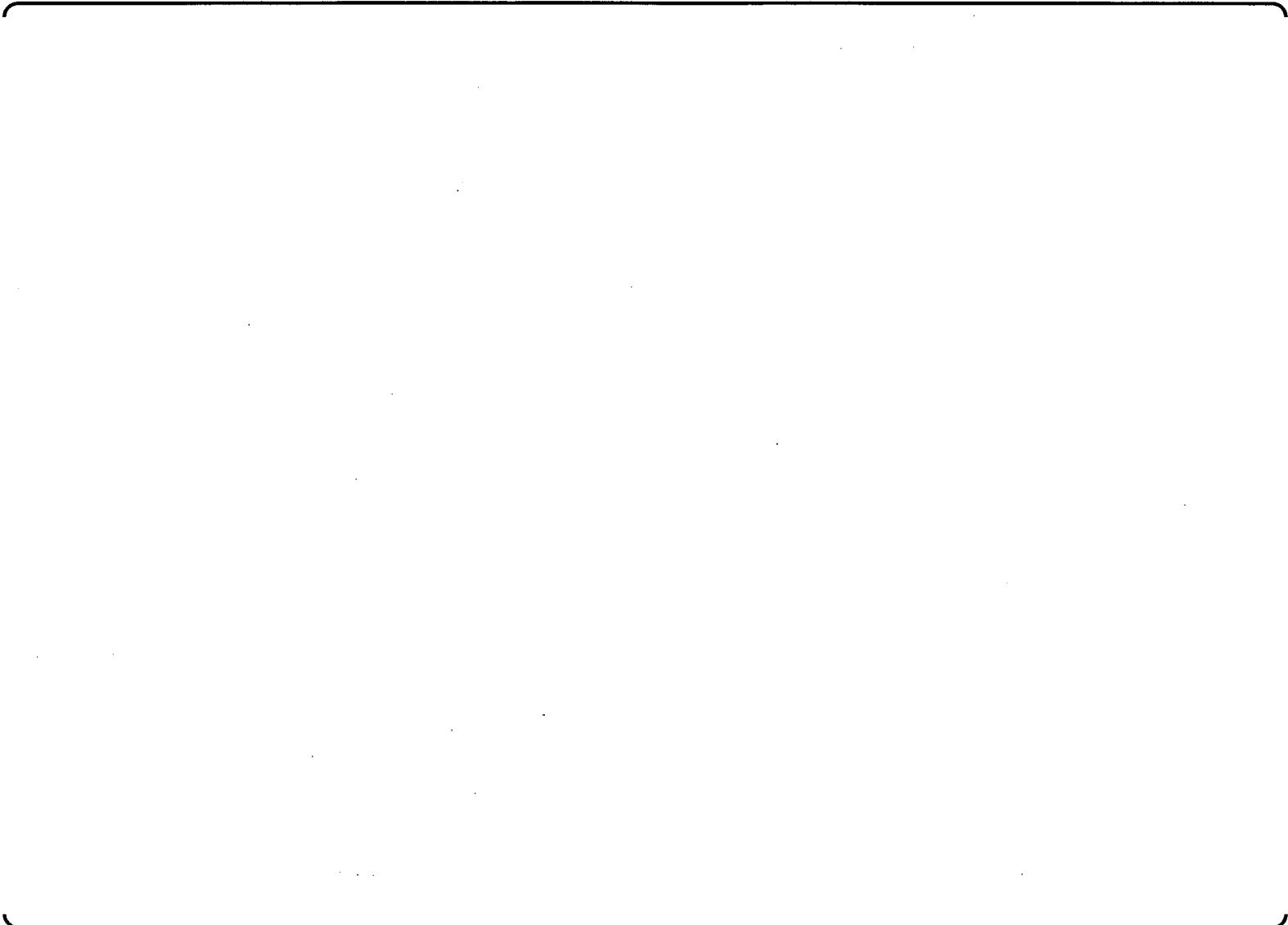


Figure 10-1 Holddown Spring Deformation

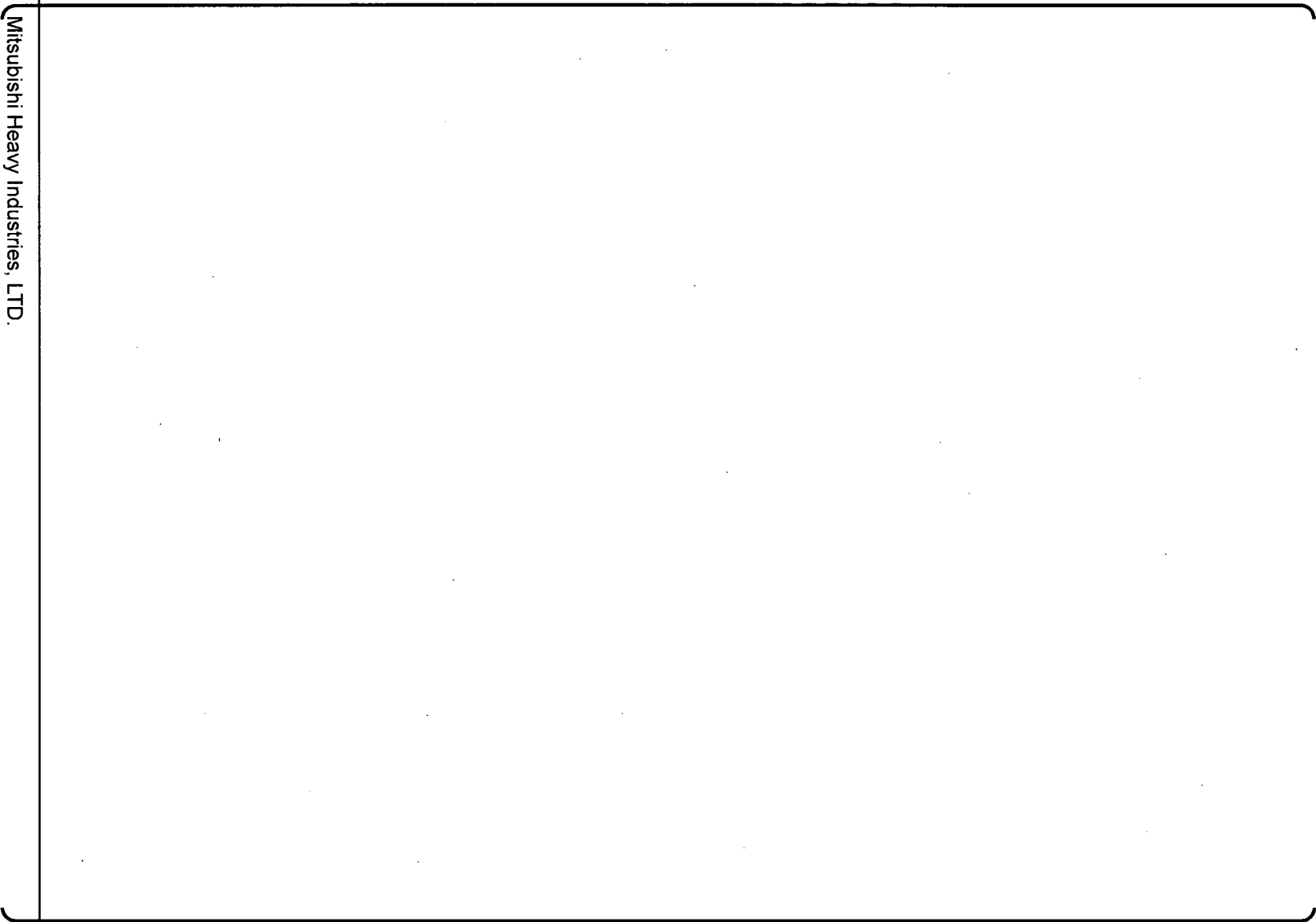


Figure 10-2 Spring Characteristics and the Holddown Force of Top Nozzle Spring



Figure 10-3 Fuel guide pin

RAI 11

What is the initial fill gas pressure of Mitsubishi fuel designs for which no cladding collapse has been observed and how many rods have been irradiated with this level of initial pressure (Section 3.3.2)? Please provide a lower limit for the initial fill gas pressure that is consistent with Mitsubishi fuel experience at this level of pressure.

RAI 11 RESPONSE

MHI has supplied more than 18000 fuel assemblies for use in commercial power reactors. MHI has not experienced any cladding collapse failure in its extensive experience since MHI began to use the 95% T.D. density pellet and pre-pressurization of the rods, with backfill pressures from []. In addition, about 300 fuel assemblies with the MHI high burnup rod design, with the 97% T.D. density fuel pellet and a [] backfill pressure, have been irradiated in a domestic PWR plant, with no experience of cladding collapse failure.

In Japanese experience cladding collapse was observed in the 1st region of Mihama Unit 1 in early 1970. The fuel used in the 1st region of Mihama Unit 1 was fabricated by Westinghouse, and had 94%T.D. pellets with no helium backfill pressure, the same as the Ginna fuel that experienced cladding collapse. These fuel pellets had high in-reactor densification due to insufficient densification when they were sintered at fabrication. The cladding collapse in the Mihama Unit 1 Region 1 fuel was a consequence of both the unstable low density pellets and no pre-pressurization.

The fabrication, operating condition and cladding collapse data for the Mihama Unit 1 Region 1 fuel are summarized below:

Reactor(Fuel region) : Mihama Unit 1 (Region 1)
Core average heat rate : 4.65 kW/ft
Inlet coolant temperature : []
Fuel type : 14x14
Active fuel length : 120 inch
Pellet density : 94 %T.D. ⁽¹¹⁻¹⁾
Pellet sintering temperature : []
Helium backfill pressure : None
Initial cladding ovality : Figure 11-1
(Typical distribution of 14x14 fuel cladding was assumed)
Observed collapse time : []
Fraction of observed collapse rods per fuel region : 1.0 % ⁽¹¹⁻¹⁾

The pellet density is increased to 97% T.D for the US-APWR fuel and it is expected that densification and the formation of axial gaps in the fuel stack will be an even smaller effect for the US-APWR fuel than it is for the MHI fuel with the 95% T.D. pellet. In addition, the US-APWR fuel is pre-pressurized by helium to a backfill pressure of []. Therefore MHI does not expect that there will be any cladding creep collapse failures for the US-APWR fuel.

In addition, MHI has applied its analytic creep collapse evaluation to US-APWR design. The detailed basis of the creep collapse analysis and the results for the US-APWR fuel are given in Reference 1a-1 App. D. This creep collapse analysis methodology has been verified and validated to be conservative without model uncertainties. The Reference 1a-1 analysis confirms that there is a negligible probability of creep collapse for the US-APWR fuel. To assure that this result will be applicable to the US-APWR fuel, the two parameters that specify the cladding ovality distribution in the analysis, [

]

Creep collapse failure of the US-APWR fuel has therefore been evaluated in terms of both the irradiation experience of the MHI fuel and the MHI analytical modeling of creep collapse. Both approaches show that the probability of cladding collapse failure is very low for the US-APWR fuel.

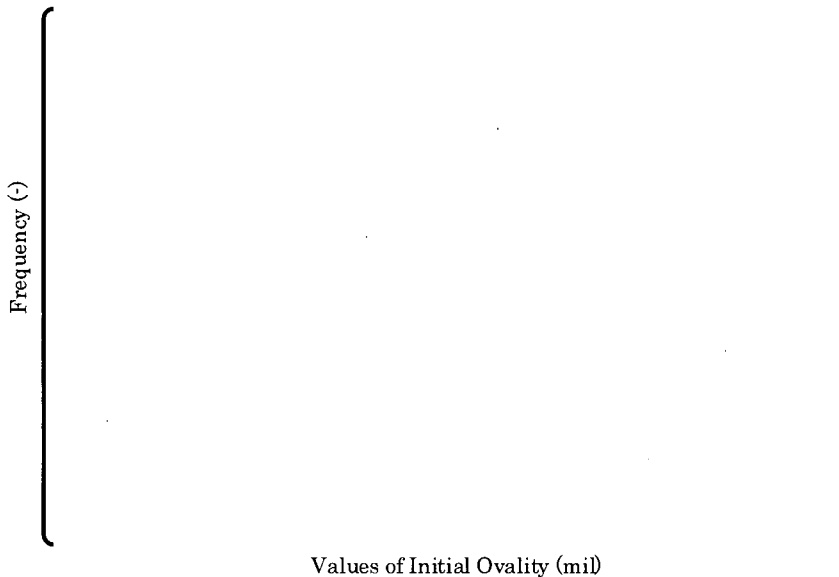


Figure11-1.Cladding ovality distribution

RAI 12

Provide an example limiting FINE calculation of best estimate fuel centerline predictions versus local linear power (similar to Figure 3.3.4-3) for the APWR at rod average burnups of 10 GWd/MTU, 30 GWd/MTU and 50 GWd/MTU. Include the input and output such that an independent calculation can be performed with the NRC FRAPCON-3 code for comparison purposes.

RAI 12 RESPONSE

The dependence of the fuel centerline temperature on the local linear heat rate at rod average burnups of 10 GWd/MTU (10025 MWd/MTU), 30 GWd/MTU (30728 MWd/MTU) and 50 GWd/MTU (49071 MWd/MTU) are shown in Figure 12-1. The fuel centerline temperature tends to increase with burnup at the same local linear heat rate due to the UO₂ thermal conductivity degradation as the burnup increases. There is also a smaller, 2nd order, effect of the radial power distribution variation with burnup, which tends to decrease the fuel centerline temperatures as the radial power distribution becomes more peaked at the pellet periphery with increasing burnup.

The FINE input and output files for the centerline temperature calculations at 10 GWd/MTU are provided on the CD-ROM with the FINE input and output files for the responses to RAI 1b and 9b.



Figure 12-1 Fuel centerline temperature versus local linear heat rate for the US-APWR
(At rod average burnups of 10 GWd/MTU, 30 GWd/MTU and 50 GWd/MTU)

RAI 13

Section 3.3.5 describes the criteria for fuel failure as a function of enthalpy rise. No correlation has been provided in the FINE documentation for fuel enthalpy as a function of temperature. Provide the correlation that is used in FINE to calculate fuel enthalpy.

RAI 13 RESPONSE

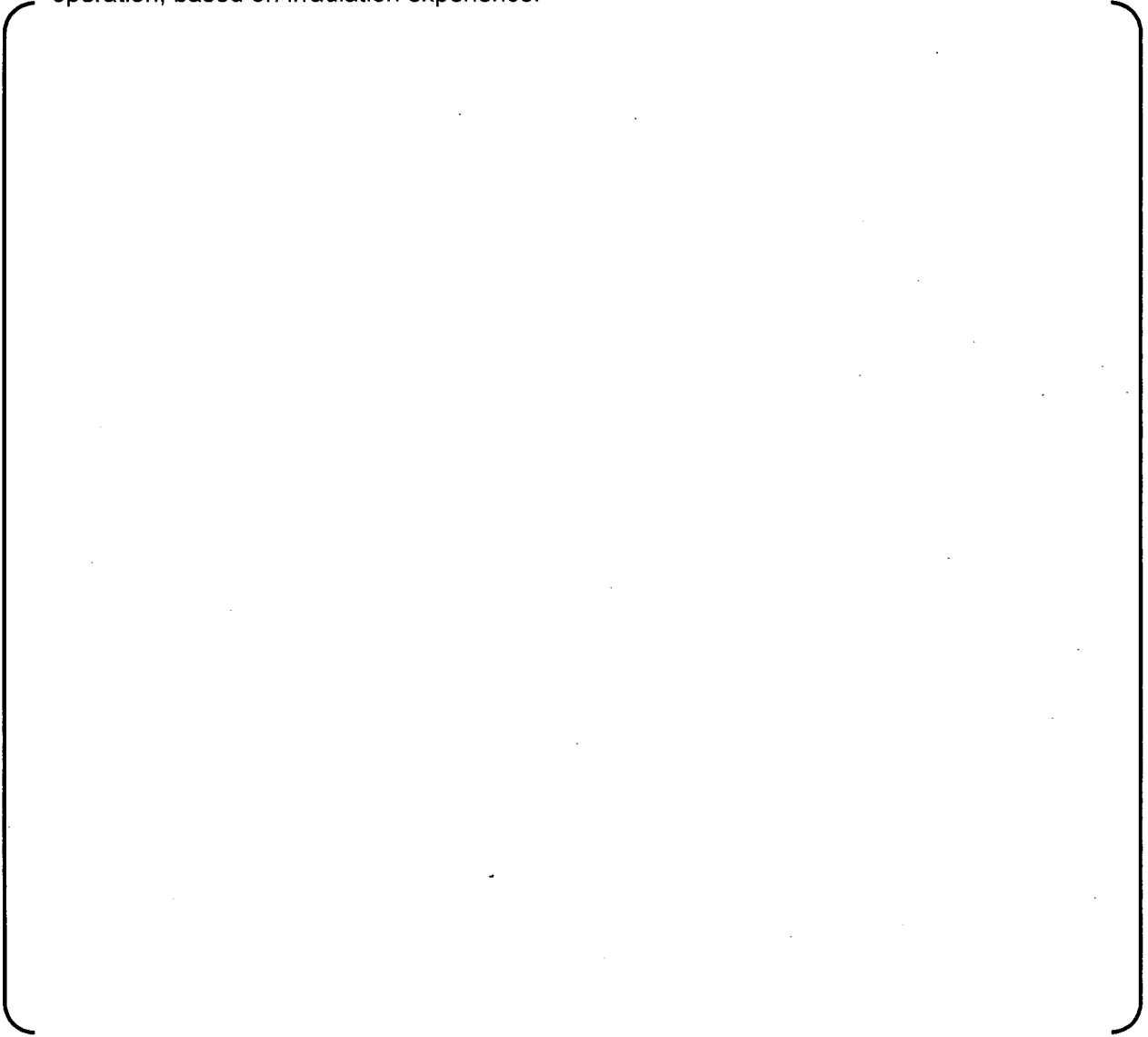
The fuel enthalpy is calculated by the VIPRE-01M code in the safety analyses of Section 15.4.8 of Reference 13-1, Spectrum of Rod Ejection Accidents. The specific heat capacity of the UO₂ pellet in VIPRE-01M is described in Reference 13-2 Appendix D "FUEL THERMAL PROPERTIES".

RAI 14

Are operational constraints placed on APWR fuel to limit PCI such as a limit on rate of power change within a given time span during normal operation? If so, what are these constraints (Section 3.3.6)? If not, justify a lack of constraint on rate of power change based on power ramp data.

RAI 14 RESPONSE

MHI recommends the following operational constraints to prevent PCI failure during normal operation, based on irradiation experience:





RAI 15

Provide the burst and ballooning (circumferential strain) relationships used for ZIRLO along with the data that are the basis for these relationships. Demonstrate how cladding strain is related to flow blockage for loss of coolant accident (LOCA) analyses (Sections 3.3.7 and 3.4.4).

RAI 15 RESPONSE

Since the cladding burst temperature is a function of the cladding hoop stress, the cladding strain at burst and flow blockage is also function of burst temperature. These models used in LOCA analysis are identical to those used for 17x17 fuel assemblies with ZIRLO™ cladding, which has been approved by the NRC (Reference 15-1). MHI uses these fuel rod models in the LOCA analysis in the same way as Westinghouse does in Reference 15-1, which was provided to the NRC on December 31, 2007. MHI referred to Reference 15-1 in Appendix A of the Reference 15-2.

RAI 16

Sections 3.3.8, 3.4.5 and Appendix D do not identify whether unirradiated properties (yield and ultimate tensile strengths) will be used for these analyses. Confirm that unirradiated properties will be used for these analyses.

RAI 16 RESPONSE

The unirradiated values are used as the design values except for the fuel cladding as described in table D.2.3-1.

The mechanical properties of Zircaloy-4 and Type 304 stainless steel are described in Appendix B of Reference 16-1.

RAI 17

Section 3.4.5 states that "Both grid spacer deformations are combined and the resulting deformation is compared with a limiting value which is experimentally defined to assure control rod insertion." Discuss the experimental test on grid spacers used to assure control rod insertion and the results (data) of these tests. Also, do the finite element analyses of the fuel assembly components discussed in Appendix D remain linear and elastic for these accidents? If the analyses are nonlinear or non-elastic, justify the use of superposition in combining stresses. If these assembly components experience plastic strains in these analyses, discuss whether ductile unirradiated material or irradiated material properties (with much less ductility) would represent the most limiting case.

RAI 17 RESPONSE

The behavior of PWR fuel assemblies and control rod insertion under seismic conditions has been studied in the Japanese government sponsored vibration test. The outline of the test and validation results for the Mitsubishi PWR fuel assemblies' seismic response analysis code FINDS have been reported in Section 5.4 of Reference 17-1.

In this test a 15x3 array of fuel assemblies was excited with the basic design earthquake ground motion waves. The tests were repeated with increasing acceleration levels, such as S1 wave, S2 wave, 1.2xS2 wave and 1.5xS2 wave. During the excitations, control rods were inserted into the fuel assemblies and the insertion times were measured. Figure 17-1 shows the results of the control rod insertion test that verify that the control rods would be inserted within the specified limit time for Japanese reactors even in the maximum acceleration case.

As is shown in Figure 17-2, the observed maximum grid spacer deformation was about 7 mm at the end of the tests.

After the series of the tests, the 15x3 array of fuel assemblies was excited by S2 wave again. As is shown in Figure 17-3, the control rod insertion time at the 2nd acceleration by S2 wave was almost equal to the time at the 1st acceleration by S2 wave in spite of the increment of the grid deformation. Therefore, the effect of grid spacer deformation on control rod insertion time is essentially small for the grid deformation level.

In the finite element analyses for the fuel assembly, the elastic beam is used for the top and bottom nozzles, fuel rods, and control rod guide thimbles.

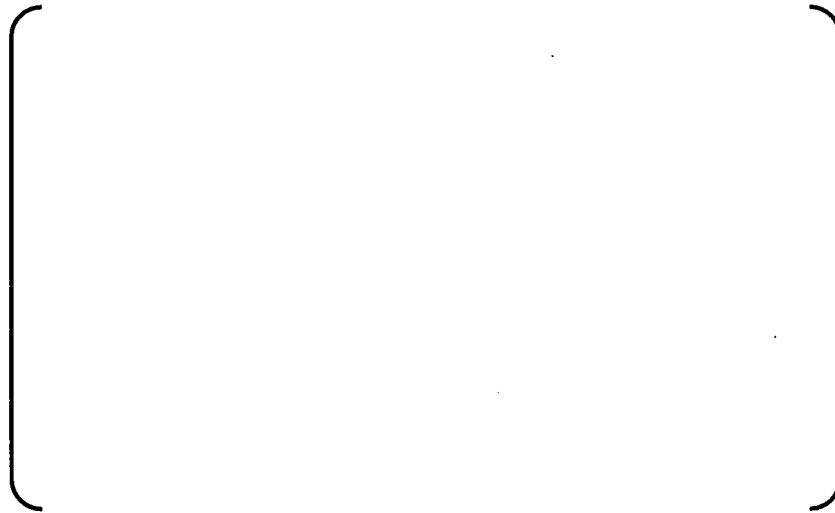


Figure 17-1 Relation between Test Model Response and Control Rod Insertion Delay Ratio⁽¹⁷⁻²⁾

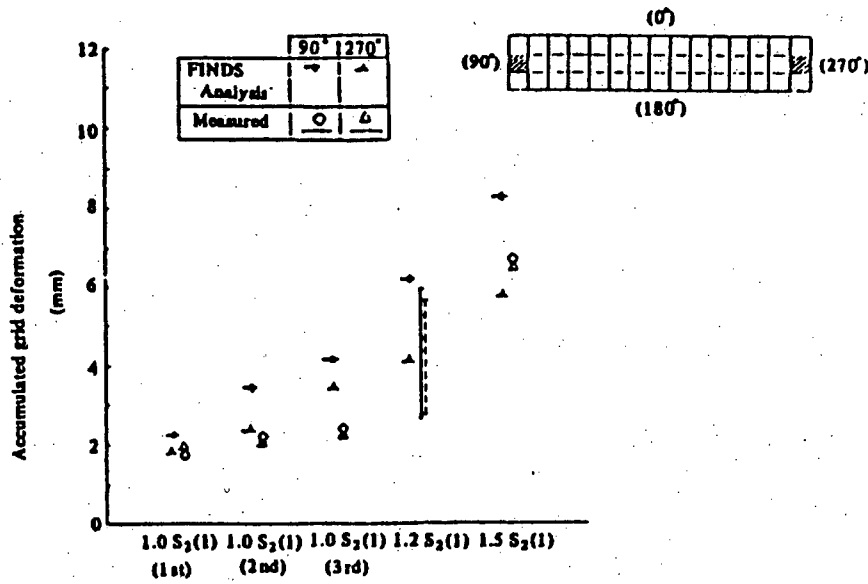


Figure 17-2 Grid Deformation Change of 5th Grid Spacer of Outermost Fuel Assemblies⁽¹⁷⁻³⁾

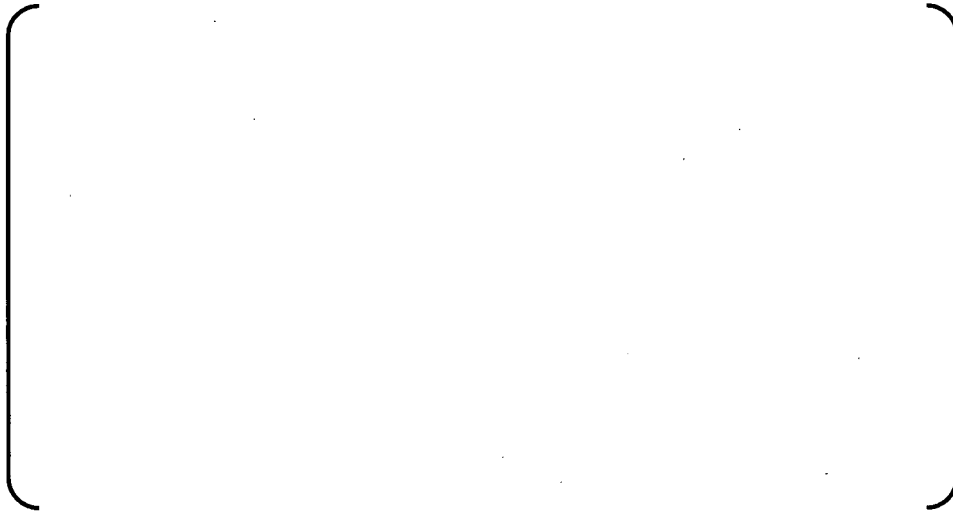


Figure 17-3 Influence of Grid Deformation on control rod Inserting Performance⁽¹⁷⁻²⁾

RAI 18

Will the FINE code or its models be used to determine initial conditions (such as stored energy, gap conductance, gas concentrations and rod pressures) for LOCA analyses? If so, provide an example FINE calculation of limiting rod initial LOCA conditions for the APWR including the input and output such that an independent calculation can be performed with the NRC FRAPCON-3 code for comparison purposes. If not, provide a description of how initial LOCA conditions are determined as a function of burnup.

RAI 18 RESPONSE

The FINE code is used to determine the initial conditions for LOCA analyses. The fuel average temperature is calculated at various burnups at the peak linear heat rate for normal operation. The peak linear heat rate is 12.1kW/ft up to 25 GWd/MTU and decreases with increasing burnup for rod average burnups above 25 GWd/MTU, following the burnup dependence of the total heat flux hot channel factor, F_Q .

Peak fuel temperature occurs at a local burnup of () GWd/MTU when the pellet to clad gap is a maximum. The limiting rod calculation results at () GWd/MTU (Table 18-1) are therefore used as the LOCA initial conditions.

The FINE input and output files for this case are provided on the CD-ROM with the FINE input and output files for the responses to RAI 1b, 9b and 12.

Table 18-1 Sample calculation results for LOCA initial conditions



RAI 19

The range of materials and irradiation conditions that are being requested for FINE need to be clearly stated.

- a. What burnup limit is being requested for FINE? Page 1-1 states that FINE is applicable to US-APWR fuel rod design with rod-average burnup to 62 GWd/t. However, Page 4-2 states the applicable range of FINE is a rod-average burnup of 65 GWd/t.
- b. Burn-up is given in units of GWD/t; what are the actual units? i.e., GWd/tU or GWd/tUO₂?
- c. The applicability range of linear heat generation rate for normal operation appears to be burn-up dependent. Discuss a revised applicability range versus burn-up based on fuel centerline temperature data (including added data comparisons from RAI number 33), FGR data (including added data comparisons from RAI number 34), and cladding strain data (including added data comparisons from RAI number 35).
- d. Clarify that FINE is being requested for licensing for:
 - i. Zircaloy-4, cold-worked, stress relieved (see RAI number 29.a)
 - ii. Zirlo™
 - iii. UO₂ of density up to 97 percent TD
 - iv. UO₂ with up to ten wt percent Gd₂O₃

RAI 19 RESPONSE

- RAI 19-a

[]

- RAI 19-b

Unless explicitly stated otherwise, the burnup units GWd/t in the report are GWd/MTU.

- RAI 19-c

A response to this RAI can be given only after completing the additional analyses requested in RAIs 33, 34 and 35.

- RAI 19-d

[]

RAI 20

Section 4.1.1 states that FINE uses a 2-D axisymmetric model with ten equal-area radial elements. However, the calculational mode, i.e., finite element or finite difference is not stated; what is the mode? Also, what is the justification for limiting the calculation to ten equal-area radial elements? How does the accuracy of the radial temperature distribution and FGR change with an additional number of radial elements?

RAI 20 RESPONSE

The FINE code fuel temperature calculation is done using the \int KdT method, with the fuel temperatures calculated using

$$\int_{T_s}^{T(r)} K(T') dT' = \int_r^{r_s} \frac{dr'}{r'} \int_0^{r'} r'' q'''(r'') dr'' \quad (20-1)$$

where

T_s is the temperature at the pellet surface

r_s is the pellet surface radius

$q'''(r)$ is the volumetric heat generation density

which is effectively a finite difference calculation of the fuel temperatures, with the integrations in the above equation done over a mesh of ten equal area radial rings.

The number of radial rings in the FINE code geometric model is fixed at ten. An independent generic evaluation has been done to determine the sensitivity of the \int KdT method to the number of radial rings. This generic evaluation considered pellet linear heat generation rates between 15 and 70 kW/m and typical radial power distributions for UO₂ fuel with pellet burnups up to 60 Mwd/kgU and 10wt% gadolinia-doped fuel with pellet burnups up to 20 Mwd/kgU.

The results of this evaluation show that the \int KdT results for the centerline temperature have very little sensitivity to the number of radial rings, and that the fuel temperatures calculated with a finite number of radial rings were always conservatively higher than the fuel temperatures calculated with an effectively infinite number of radial rings. For the UO₂ fuel radial power distributions, the centerline temperature predictions with ten radial rings are within () of those calculated for an effectively infinite number of radial rings for temperature rises across the pellet up to (). The maximum deviation between the centerline temperature results with ten radial rings and with an effectively infinite number of radial rings is (). For the gadolinia-doped fuel radial power distributions, the centerline temperature predictions with ten radial rings are within () of those calculated for an effectively infinite number of radial rings for temperature rises across the pellet up to () and the maximum deviation between the centerline temperature results with ten radial rings and with an effectively infinite number of radial rings is (). For both the UO₂ and gadolinia-doped fuel the differences in the fuel temperatures calculated with ten radial rings and with an effectively infinite number of radial rings is much less than the () fuel centerline temperature uncertainty used in the FINE design criteria evaluations. This generic evaluation therefore shows that the FINE pellet geometry, with ten radial rings, does not have any significant impact on the accuracy of the FINE predictions for

the fuel temperatures. Since the fuel temperatures are insensitive to the number of radial rings, it is expected that the fission gas release results will also be insensitive to the number of radial rings.

RAI 21

The following questions relate to understanding the cladding creep model

- a. On the bottom of page 4-40, the units for fast neutron flux are given as n/cm^2 . Should this be $n/cm^2/s$?
- b. The equations for $\dot{\epsilon}_{thermal}$ given in eq. 4.2.4.4-8 and eq. 4.2.4.4-12 are a function of $\dot{\epsilon}_{thermal}$. What values is $\dot{\epsilon}_{thermal}$ set to at time=0.
- c. How are negative values of σ_e handled when P_s is greater than P_f+P_{ct} ? Negative values of σ_e result in complex numbers for $\dot{\epsilon}_{thermal}$ and $\dot{\epsilon}_{irradiation}$.
- d. The values of $\dot{\epsilon}_{thermal}$ for Zircaloy-4 and ZIRLO are 1 to 2 orders of magnitude different for the same temperature. It appears the equation for $\dot{\epsilon}_{thermal}$ for ZIRLO (eq. 4.2.4.4-12) may be in error because the values are much greater than those for $\dot{\epsilon}_{thermal}$. Based on these observations, re-examine eq. 4.2.4.4-12 provided in the submittal for ZIRLO for possible errors. Also, confirm that in eq. 4.2.4.4-12 that σ should be σ_e , and that ϵ should be $\epsilon_{thermal}$.

RAI 21 RESPONSE

- RAI 21a

There is a typographical error on the bottom of page 4-40. The units for fast neutron flux are n/cm²/s.

- RAI 21b

()

- RAI 21c

There is a typographical error in the equation for σ_e in the topical report. The correct equation is

$$\sigma_e = \frac{2\sqrt{3} \cdot K^2 \cdot \ln K \cdot |P_f + P_{ct} - P_s|}{(K^2 - 1)^2} \quad (21-1)$$

and there is no possibility that complex numbers would be calculated in the calculation of the thermal and irradiation creep effective strain rates. The diametral strain rates are calculated from the effective strain rates using

$$\dot{\epsilon}_d = \frac{\sqrt{3}}{2} \cdot \dot{\epsilon}_e \cdot \text{sign}(P_f + P_{ct} - P_s) \quad (21-2)$$

where

$\dot{\epsilon}_d$: the diametral strain rate

$\dot{\epsilon}_e$: the effective strain rate

which gives compressive strains if P_s is greater than $P_f + P_{ct}$, and tensile strains if P_s is less than $P_f + P_{ct}$.

- RAI 21d

There is a typographical error in Eq. 4.2.4.4-8 for the Zr-4 thermal creep rate. The correct equation is

()
 i.e., the correct expression for the temperature dependence or exponent of $\epsilon_{\text{thermal}}$ on the right hand side of this equation is

()
 not

()

With this correction the FINE model for the thermal creep of unirradiated ZIRLO™ still predicts significantly more thermal creep than the FINE model for the thermal creep of Zr-4, but the difference is significantly smaller than stated in RAI 21d.

In equation 4.2.4.4-12, it is correct that σ is σ_e , and that ϵ is $\epsilon_{thermal}$.

RAI 22 RESPONSE

- RAI 22a

The units for the temperature variable T used in the expressions for the thermal conductivity of Helium, Xenon, Krypton, air, Nitrogen and Hydrogen, are °R. The units for the temperature variable T in the expression for the thermal conductivity of Argon is °F. The documentation will be revised to explicitly state the temperature units that are used in these equations as follows.

Xenon	[
Krypton	
Air	
Nitrogen	
Hydrogen	
Argon	
Helium	

- RAI 22b

There are several versions of MATPRO^{(22b-1),(22b-2),(22b-3)}. References (22b-1) and (22b-2) give the same correlations for the gas thermal conductivities, but Reference (22b-3) gives different correlations for the gas thermal conductivities:

(1) MATPRO (2001)^(22b-1) and MATPRO Version 11 Revision 2 (1981)^(22b-2):

The Reference (22b-1) and (22b-2) correlations of the thermal conductivities of Ar, Kr, N₂ and H₂ are as follows:

Argon	$K_{Ar} = 2.986 \times 10^{-4} T^{0.7224}$	(W/m/K)	T: K
Krypton	$K_{Kr} = 8.247 \times 10^{-5} T^{0.8363}$	(W/m/K)	T: K
Nitrogen	$K_{N_2} = 5.314 \times 10^{-4} T^{0.6898}$	(W/m/K)	T: K
Hydrogen	$K_{H_2} = 1.097 \times 10^{-3} T^{0.8785}$	(W/m/K)	T: K

(2) MATPRO-Version 11 (1979)^(22b-3):

Argon	$K_{Ar} = 3.421 \times 10^{-4} T^{0.701}$	(W/m/K)	T: K
Krypton	$K_{Kr} = 8.247 \times 10^{-5} T^{0.8363}$	(W/m/K)	T: K
Nitrogen	$K_{N_2} = 2.091 \times 10^{-4} T^{0.846}$	(W/m/K)	T: K
Hydrogen	$K_{H_2} = 1.6355 \times 10^{-3} T^{0.8213}$	(W/m/K)	T: K

Figure 22b-1 compares the thermal conductivity of gases in the temperature range expected for actual fuel use. The gas conductivities used in the FINE code are most similar to those given in MATPRO Version 11(1979).

The largest difference between the FINE code correlations and the MATPRO correlations occurs for Hydrogen. However, Hydrogen is a very minor component of the fuel rod gases, since the fuel rod is pre-pressurized with Helium and, and the fission gases, Xenon and Krypton, are the other dominant components of the gas in the pellet-cladding gap. The difference between the FINE and MATPRO correlations for K_{H_2} will therefore not have any significant impact on the US-APWR fuel rod evaluations.

On the other hand, there is a small difference between the FINE and MATPRO correlations for K_{Kr} , a relatively significant component of the fuel rod gap gases. At 700 deg.F the FINE correlation gives $K_{Kr} = (\quad)$ whereas the MATPRO (2001) and MATPRO Version 11 Revision 2 (1981) correlation gives $K_{Kr} = 1.06 \times 10^{-2}$ BTU/Hr/ft/deg.F, an approximately (\quad) difference. However, at end of life a typical value for the Krypton mole fraction in the US-APWR gap gases is (\quad) and this (\quad) difference in the values for K_{Kr} will not have a significant effect on the temperature rise across the pellet-cladding gap.

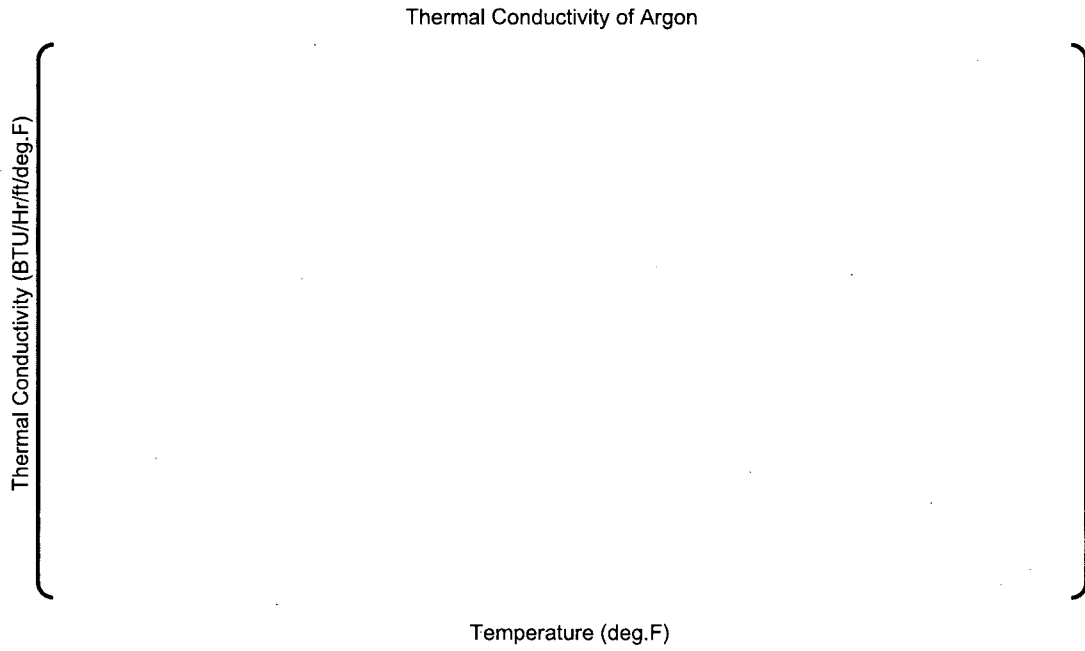


Figure 22b-1 (1) Thermal Conductivity of Argon

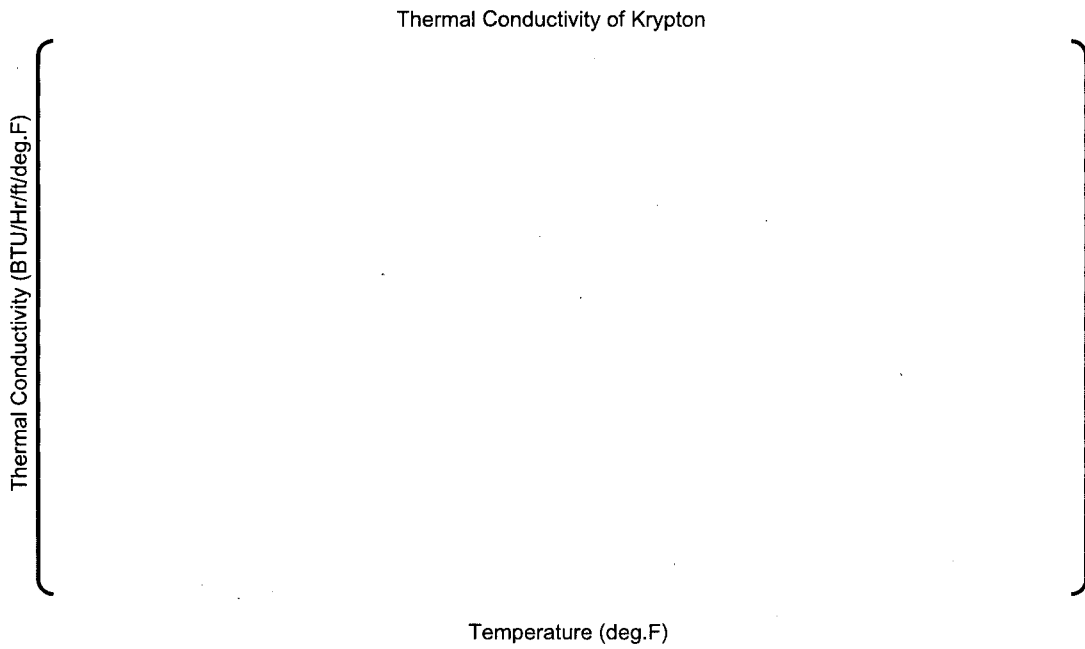


Figure 22b-1 (2) Thermal Conductivity of Krypton

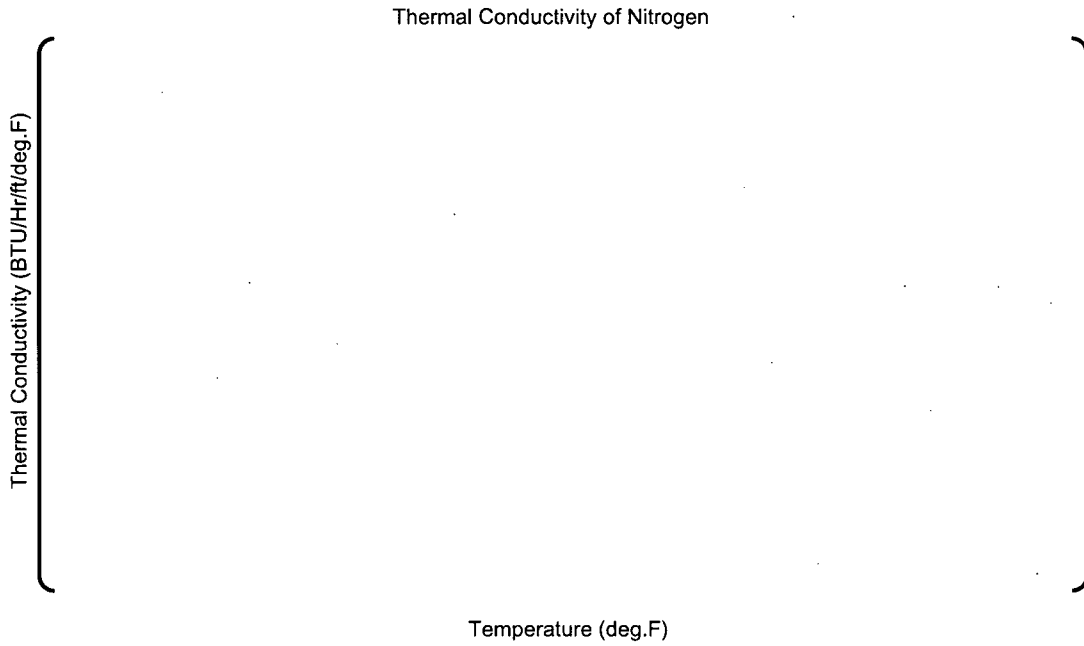


Figure 22b-1 (3) Thermal Conductivity of Nitrogen

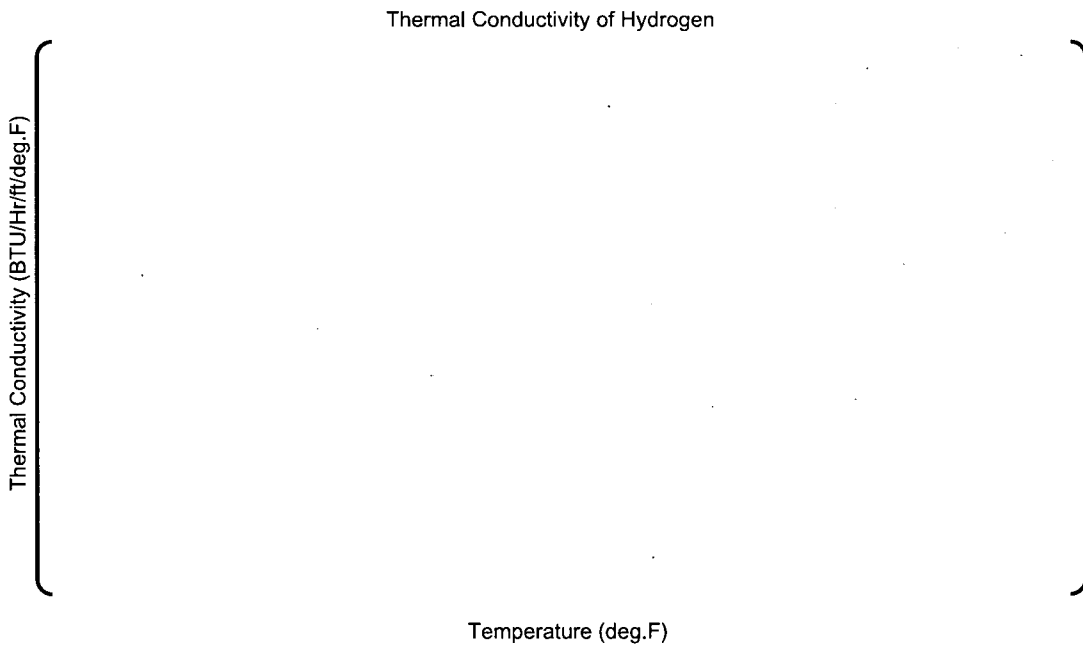


Figure 22b-1 (4) Thermal Conductivity of Hydrogen

RAI 23

The following questions relate to understanding the gap conductance equations given on page 4-12.

- a. The variable, EXO, is defined as the surface roughness multiplier and is shown as an input variable on page C-8. What is the meaning of this variable, how is its value selected for licensing calculations, and what is a typical value for this variable?
- b. Open gap conductance (Sec 4.2.1.3) is defined by eq. 4.2.1.3-3. In this equation $hgap_1$ is the "standard" $kgas/x$ where x is the open gap size. However, what is the basis for $hgap_2$? Is the purpose of $hgap_2$ to specify a minimum gap for very large gaps?

RAI 23 RESPONSE

- RAI 23a

The FINE code equation for the gap conductance is based on Dean's equation ^(23a-1). The term given by " " is the effective minimum gap, which includes the effect of the combined surface roughness of both the cladding inner surface and the pellet surface. The variable EXO is the multiplier factor and is determined from the fabrication specification. In the US-APWR design, the specification limits for the cladding inner surface roughness and the pellet surface roughness are () and (), respectively. The effective mean gap based on the treatment in Dean's paper and the US-APWR specification is () so that the multiplier factor, EXO, is () which is equal to () divided by 14.4.

- RAI 23b

Figure 23b-1 shows the typical behavior of the gap conductance as a function of the diametral gap between the cladding and the pellet. The maximum of $hgap_1$ and $hgap_2$ is used in the FINE code to calculate the temperature rise across an open gap between the cladding and the pellet. For the results shown in Figure 23b-1 the gap conductance given by $hgap_1$ would be used for diametral gaps less than approximately 4 mils (approximately 100 μm) and the gap conductance given by $hgap_2$ would be used for larger diametral gaps.

Figure 23b-2 compares the predictions of the FINE code with respect to the measured temperature data as a function of gap size. The FINE code thermal models, including $hgap_2$, are verified by these data.

The expression for $hgap_2$ was derived from thermocouple fuel centerline temperature data and melt radius data ^(23b-1).

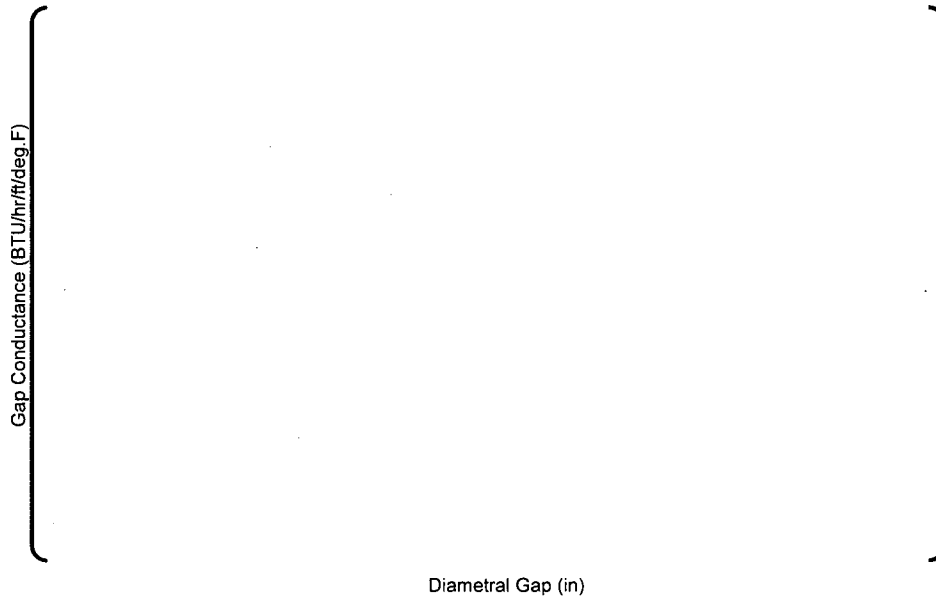


Figure 23b-1 Typical gap conductance dependence on gap size

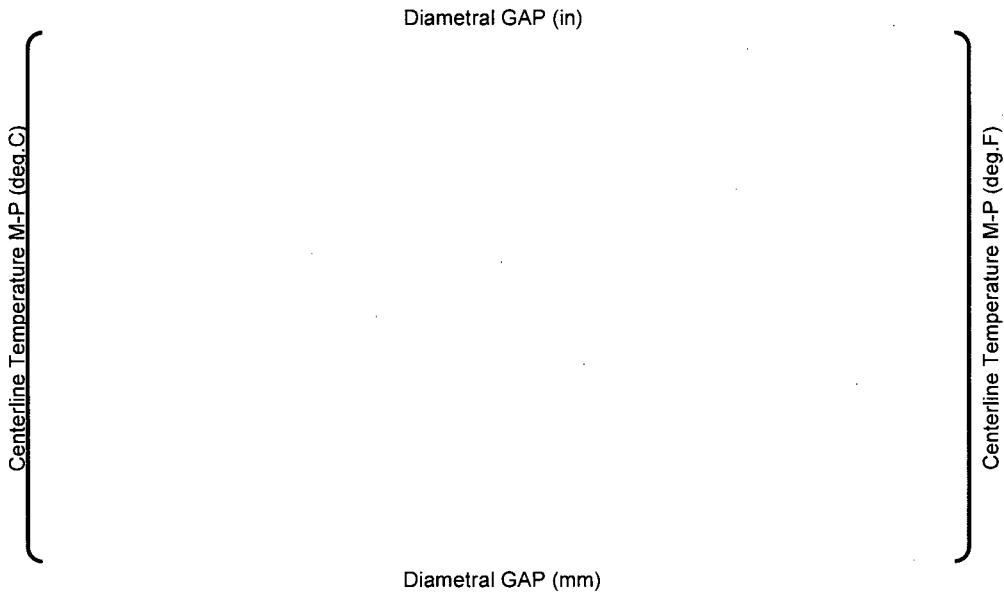


Figure 23b-2 Comparison of FINE code centerline temperature predictions with the measured data as a function of the diametral gap size

RAI 24

For the cladding corrosion model given on Page 4-34, the units on b are given as $(\text{mg}/\text{dm}^2)^3/\text{day}$. Should these units be $(\text{mg}/\text{dm}^2)/\text{day}$? What is the primary coolant outlet temperature for the APWR during normal operation at 100 percent power? How does this outlet temperature compare to those in current Mitsubishi plants from which the ZIRLO corrosion data were obtained (Figures 4.3.5-1 and 4.3.5-2) and the value(s) used?

RAI 24 RESPONSE

For the cladding corrosion model given by Eq. 4.2.4.1-2 on Page 4-34, the units on b should be $(\text{mg}/\text{dm}^2)/\text{day}$, as stated in the RAI. A MUAP-07008-P, Rev. 1 topical report will be issued with the correct units for b.

The US-APWR coolant conditions and a comparison with the coolant conditions for the plants where the ZIRLO™ corrosion data have been obtained are shown in Table 24-1 below. The US-APWR coolant conditions are bounded by the coolant conditions of the ZIRLO corrosion database.

Table 24-1 Comparison of US-APWR Coolant Conditions with ZIRLO™ Corrosion Data Plant Coolant Conditions.



RAI 25

For the pellet densification model given on page 4-29, the value for Ts (densification parameter) is not given. Is a constant value used for this, or is this parameter provided in the input? If so, what is the physical basis for this parameter?

RAI 25 RESPONSE

In the original development of the FINE code densification model the Ts parameter was defined by the pellet sintering temperature during fabrication. It was found, in further development of the densification model, that the Ts parameter is not always correctly defined by the pellet fabrication sintering temperature. The Ts value now used in the FINE code densification model is determined from the density change measured in a resintering test at 1700 deg.C for 24 hours, such that the Ts value is adjusted to simulate the density change in the resintering test. In the design evaluations, where necessary the density change results of the resintering tests are statistically treated and the input values for the design evaluation are determined based on Regulatory Guide 1.126 ⁽²⁵⁻¹⁾.

The standard value for Ts in the licensing analysis is shown in the FINE inputs provided in the CD-ROM as "XDEN".

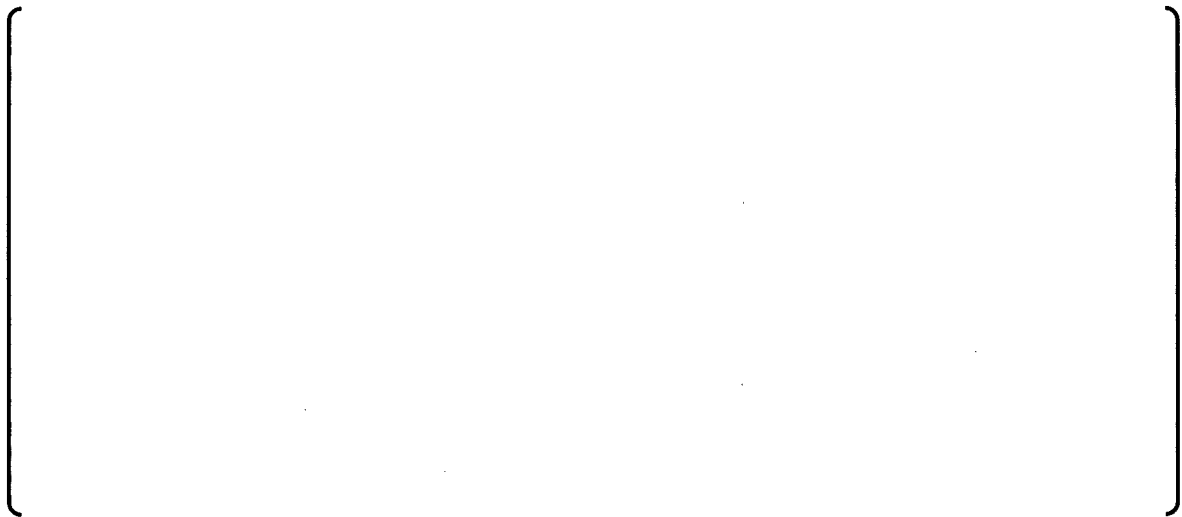
RAI 26

The cladding ID oxidation data provided in Section 4.2.4.5 implies that essentially no oxide formation occurs until some contact is experienced between the fuel and cladding at around 27 to 30 GWd/MTU. However, this disagrees with ID oxide data provided by others (L. Desgranges, Thermal Performance of High Burn-Up LWR Fuel Seminar Proceedings, Cadarache, France, 1998, pg 187) and (Walker et al., JNM 245, pg 169) that show ID oxide formation at burnups of 10 and 15 GWd/MTU. Have metallographic examinations been performed on commercial rods at lower burnups to determine whether an ID oxide exists, and if so, how many rods have been examined at peak axial power (central) locations and low burnup to verify no oxide exists on the ID at lower burnup levels?

RAI 26 RESPONSE

MHI has no experience of oxide formation on the cladding ID prior to fuel-clad contact. Metallographic examinations of low burnup commercial fuel rods have been performed by MHI. The fabrication and irradiation conditions for the fuel examined are given in Table 26-1. Optical photomicrographs of cross-sections of the KTN-3 and KON-1 rods are shown in Figure 26-1 as an example of the representative behavior of the low burnup fuel. The results of these metallographic examinations confirm that there is no oxide formation on the cladding ID at these low burnups, prior to fuel-clad contact. Figure 26-2 shows the comparison of these data with the data in Reference 9a-1. These low burnup Takahama (KTN-3) and Ohi (KON-1) data are consistent with the data shown in Figure 4.2.4.5-1 of Reference 9a-1.

Table 26-1 Fabrication and irradiation conditions for the low burn-up metallographic data



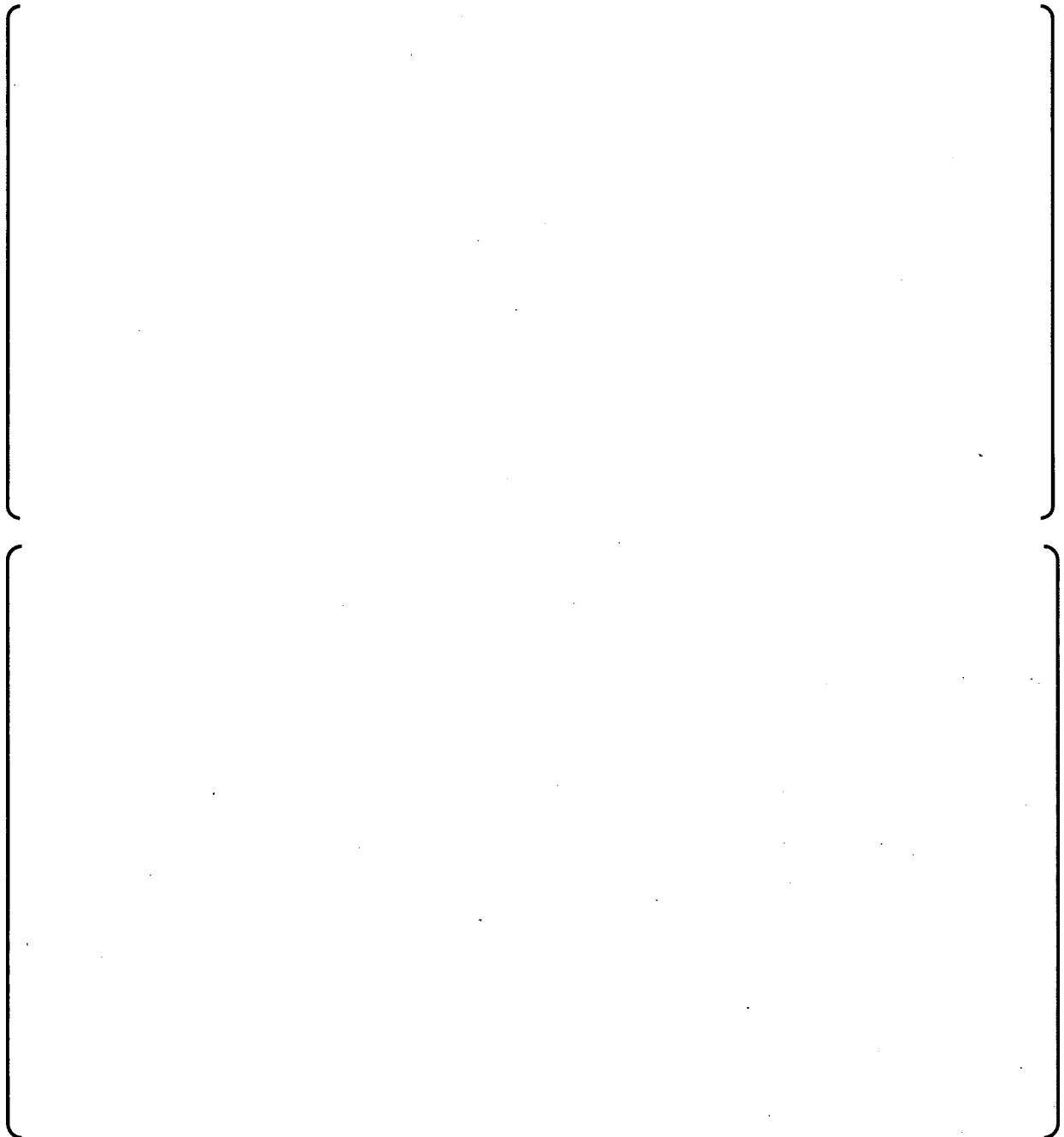


Figure 26-1 Optical photomicrographs of the cladding ID and pellet OD cross-sections

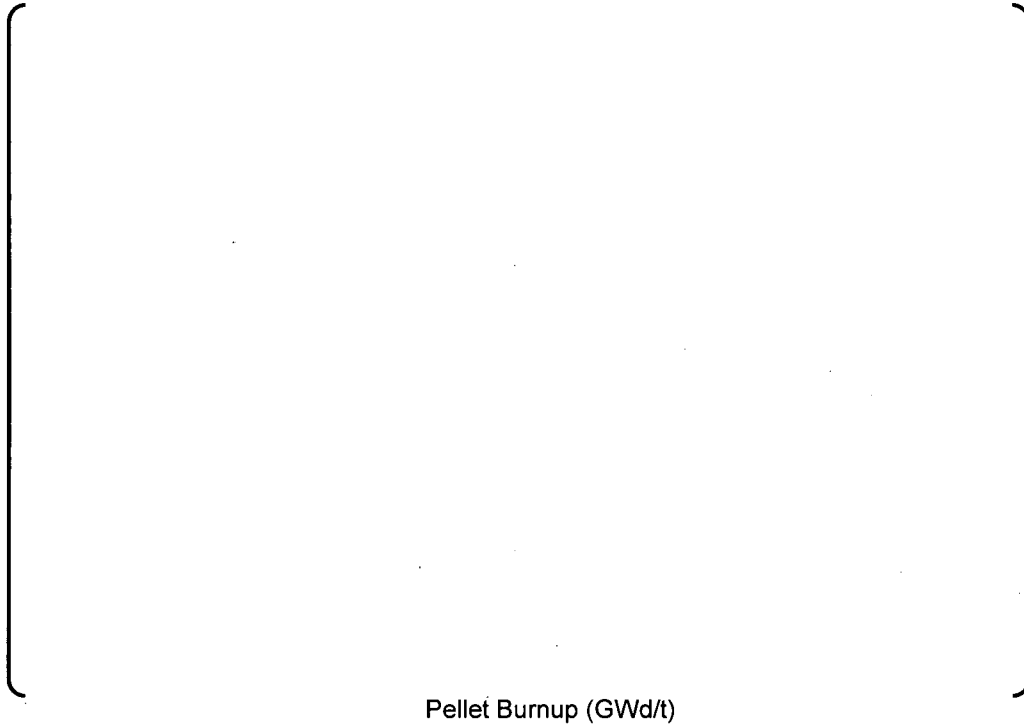


Figure 26-2 Comparison of the Takahama and Ohi data with the Reference 9a-1 Figure 4.2.4.5-1 data

RAI 27

A look-up routine is used for the radial power profile as described on Page 4-55. In addition to the sample radial power distribution table provided, provide a sample radial power distribution for 2 wt percent ^{235}U , and for $\text{UO}_2\text{-Gd}_2\text{O}_3$ fuel at 2 wtpercent Gd_2O_3 and at 8 wt percent Gd_2O_3 . For the gadolinia fuel, provide more details on radial power in the low burn-up range while the gadolinia is burning out.

RAI 27 RESPONSE

Rather than providing the requested radial power distributions, Tables 27-1 and 27-2 give the radial power distributions for the gadolinia concentrations used in the US-APWR design, 6 and 10 wt% Gd_2O_3 with a ^{235}U enrichment of 2.95 wt%. These are typical radial power distributions for the gadolinia fuel actually used in the US-APWR, and should give sufficient information to meet the concerns identified in this RAI. In these Tables, Ring 1 is the center ring, Ring 10 is the outermost ring, and all the radial rings have the same volume.

Table 27-1. 6wt% Gadolina doped fuel radial power distribution, 2.95 wt% ²³⁵U

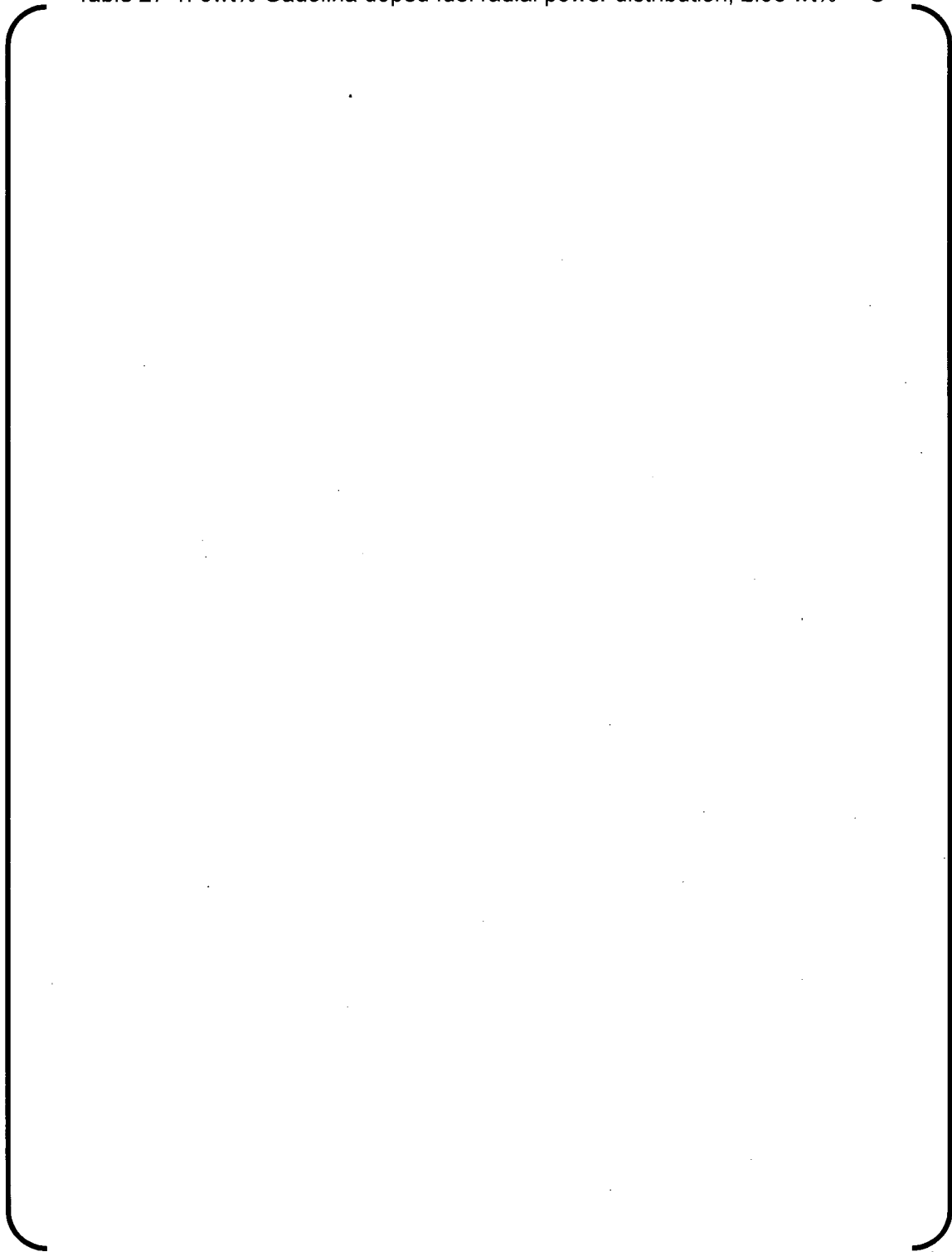
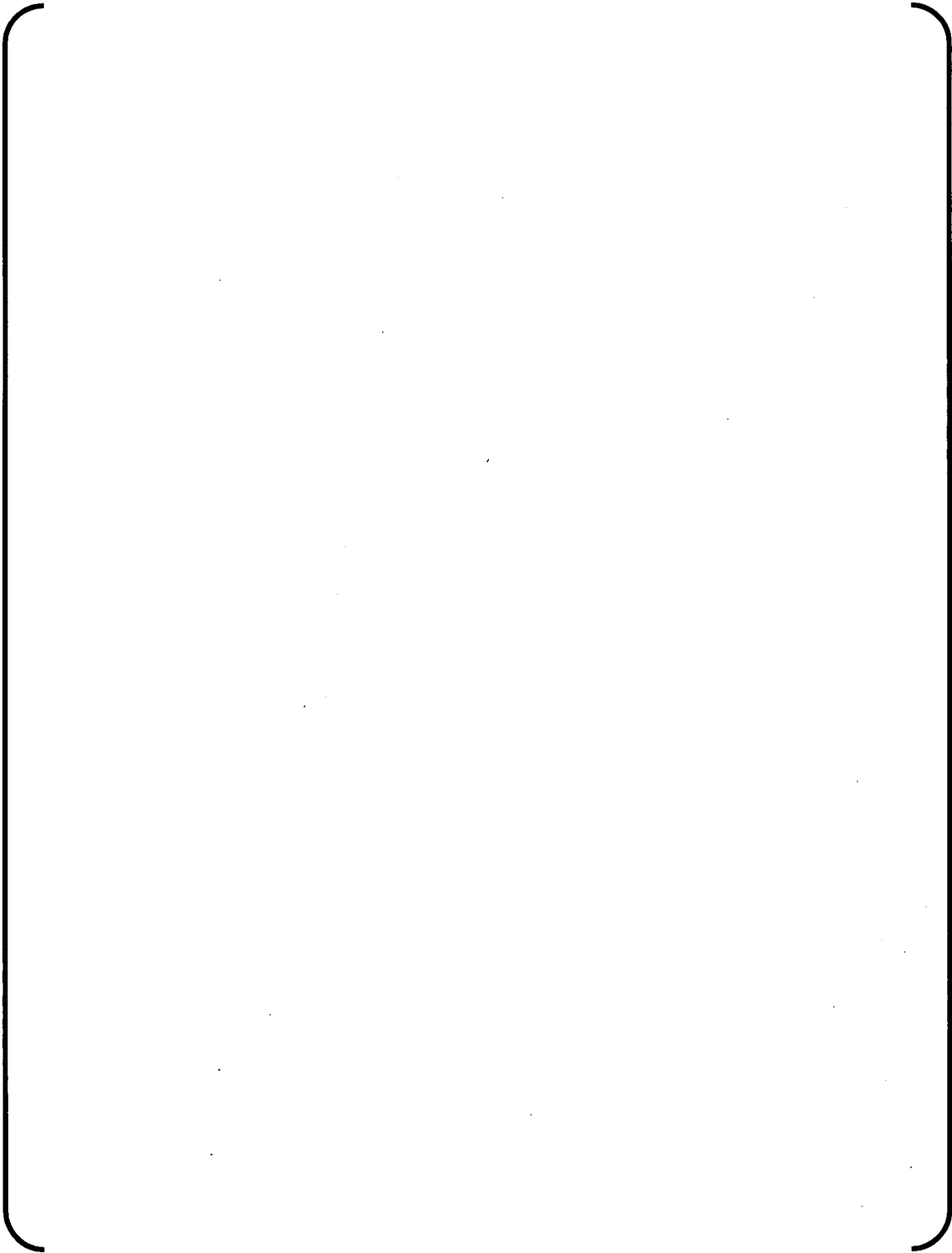


Table 27-2. 10wt% Gadolina doped fuel radial power distribution, 2.95 wt% ²³⁵U



RAI 28

In order to better understand the FINE prediction of rim thermal conductivity provide predicted rim thermal conductivity as a function of burn-up from 50 GWd/MTU up to 140 GWd/MTU at three temperatures of 500°C, 600°C and 700°C assuming an initial as-fabricated density of 97 percent TD. Also, provide the fuel centerline temperature as a function of burn-up for a constant linear heat generation rate of 8 kW/ft up to a pellet average burn-up of 65 GWd/MTU with and without (no rim effect, no porosity change in rim) the rim being present. Provide a comparison of the FINE calculated rim conductivity to those measured in the High Burn-up Rim Project (HBRP).

RAI 28 RESPONSE

The FINE model results for the rim region thermal conductivity as a function of burnup from 50 GWd/MTU to 140 GWd/MTU, at 500, 600 and 700 deg. C and assuming an initial pellet density of 97%TD, is shown in Figure 28-1. In the FINE model the effect of the rim formation on the thermal conductivity is due to the rim region porosity, which increases with burnup. The total porosity in the rim region is the sum of the rim porosity, the residual fabrication porosity and the gas bubble porosity. Bakker's equation⁽²⁸⁻¹⁾ is used to correct the thermal conductivity for 95% TD fuel to account for the actual total porosity in the rim region.

The FINE code results for the centerline temperature as a function of burnup with and without the rim effect are shown in Figure 28-2. The centerline temperatures have been calculated assuming a constant rod power of 8 kW/ft and a flat axial power shape, (

MHI's Responses to the NRC's RAI on
Topical Report MUAP-07008-P(0)
"Mitsubishi Fuel Design Criteria and Methodology"

UAP-HF-08299-NP (R0)

(

)



Figure 28-1 Thermal conductivity in the rim region

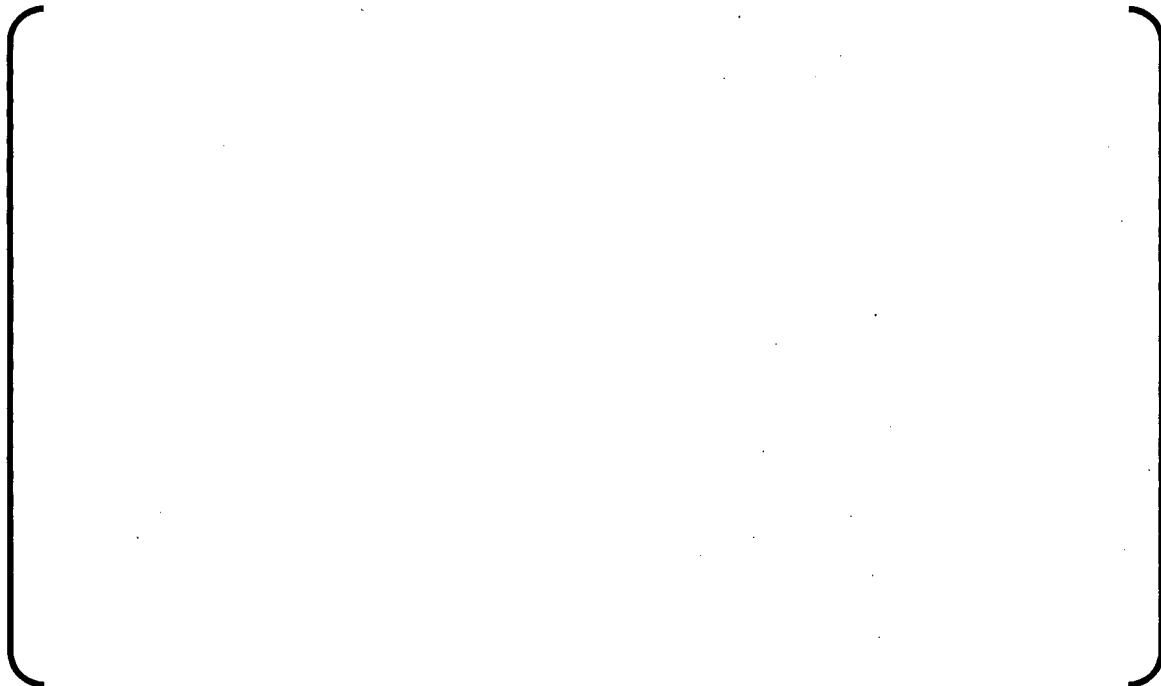


Figure 28-2 Fuel centerline temperature versus burnup with or without the rim region models for a rod power of 8 kW/ft throughout life

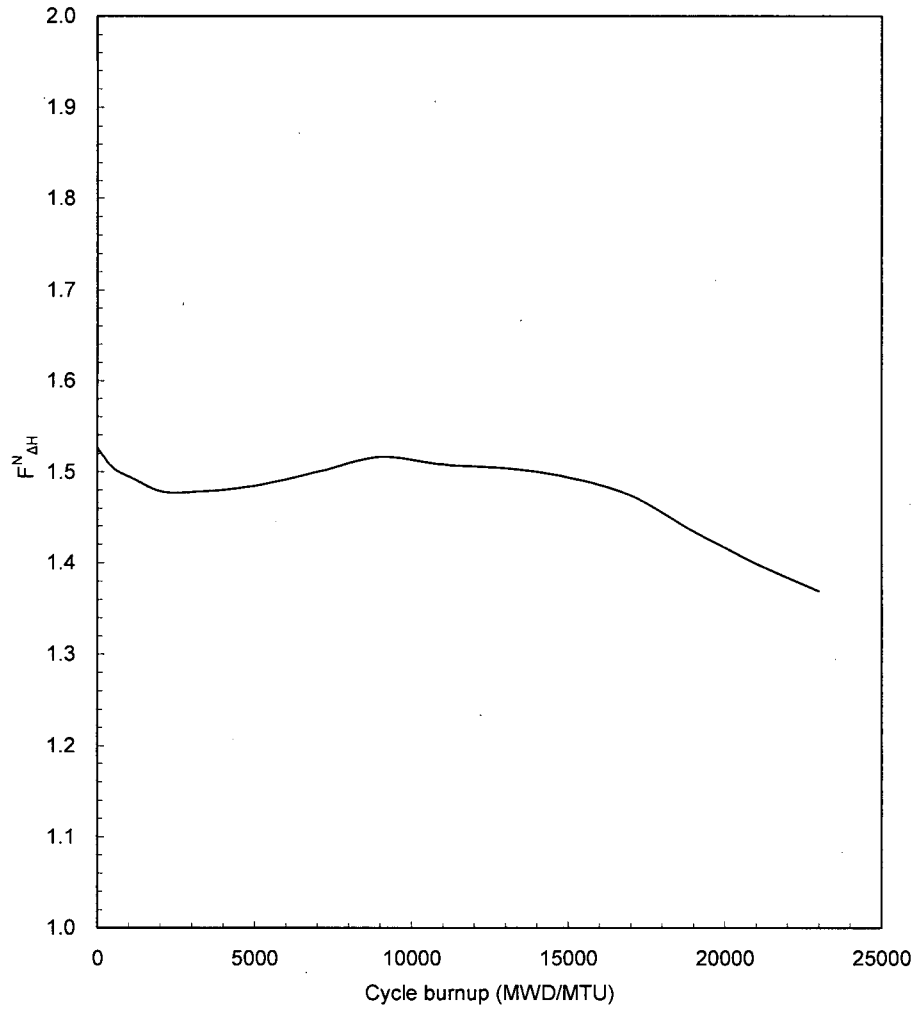


Figure 28-3 $F_{\Delta H}^N$ versus Core Depletion (HFP, ARO *)
from MUAP-07016 Figure A-17



Figure 28-4 Fuel centerline temperature versus burnup with or without the rim region models for a rod power of 7.5 kW/ft throughout life



Figure 28-5 Comparison of thermal Conductivity as a function of burnup with HBRP data

RAI 29

The following discusses the Zircaloy-4 (Zr-4) and ZIRLO creep model separately.

- a. The document states that Zr-4 cladding irradiation creep data were only obtained from cladding diameter measurements when the fuel-cladding gap remained open (top of page 4-41). The fuel cladding gap in most PWR fuel rods in the US is closed by a burn-up of 35 to 40 GWd/MTU while some of the Zr-4 irradiation creep data used for irradiation creep model verification is from 3-cycle fuel. What is the burn-up level of this 3-cycle fuel? If it is above 35 GWd/MTU demonstrate that the gaps have remained open in this 3-cycle fuel. If only ZIRLO clad fuel is to be licensed in US applications and the Zr-4 model is only used in code verification and validation comparisons (where Zr-4 cladding has been used) this RAI (29.a) can be ignored. If not, respond to this RAI.
- b. The irradiation creep data used to develop the ZIRLO creep model (Table 4.2.4.4-1) are from only 11 full length rods and 20 segmented rods up to 23 GWd/MTU (gap closure is unlikely) from two reactors. Provide this ZIRLO irradiation creep data as follows identifying the two different reactors in these plots with different symbols.
 - i. predicted versus measured
 - ii. predicted-minus-measured versus fluence
 - iii. predicted-minus-measured versus measured

Further, Section 4.3.8 states that the uncertainty in the creep model excluded the segmented rods and bottom and top span (skewed profile) rods. Justify the elimination of these rods from the uncertainty determination. This results in a very small number of rods from which the uncertainty is determined. This is of concern because this may underestimate the uncertainty in the creep model. For example, this will not accurately measure the batch to batch variability in creep due to fabrication differences.

RAI 29 RESPONSE

- RAI 29-a

()

- RAI 29-b

[]

To evaluate whether there is any bias as a function of the main parameters of the creep model, comparisons have been made for 1) the variation of the ratio of the measured to calculated diameter change as a function of fast neutron fluence; 2) the difference between the measured and the calculated diameter change as a function of the fast neutron fluence; 3) the ratio of the measured to the calculated diameter change as a function of the measured diameter change; and 4) the difference between the measured and the calculated diameter change as a function of the measured diameter change. Figure 29b-2 shows the ratio of the measured diameter change to the predicted diameter change as a function of fluence, Figure 29b-3 shows the measured minus predicted diameter change as a function of fluence, Figure 29b-4 shows the ratio of the measured diameter change to the predicted diameter change as a function of the measured diameter change, and Figure 29b-5 shows the difference between the measured and predicted diameter change as a function of the measured diameter change. There is no significant bias or trend in any of these four Figures.

[]





Figure 29b-1 Comparison of measured rod diameter decrease data with the FINE code predictions



Figure 29b-2 Measured / Calculated (Predicted) diameter change versus fluence



Figure 29b-3 Measured - Calculated (Predicted) diameter change versus fluence

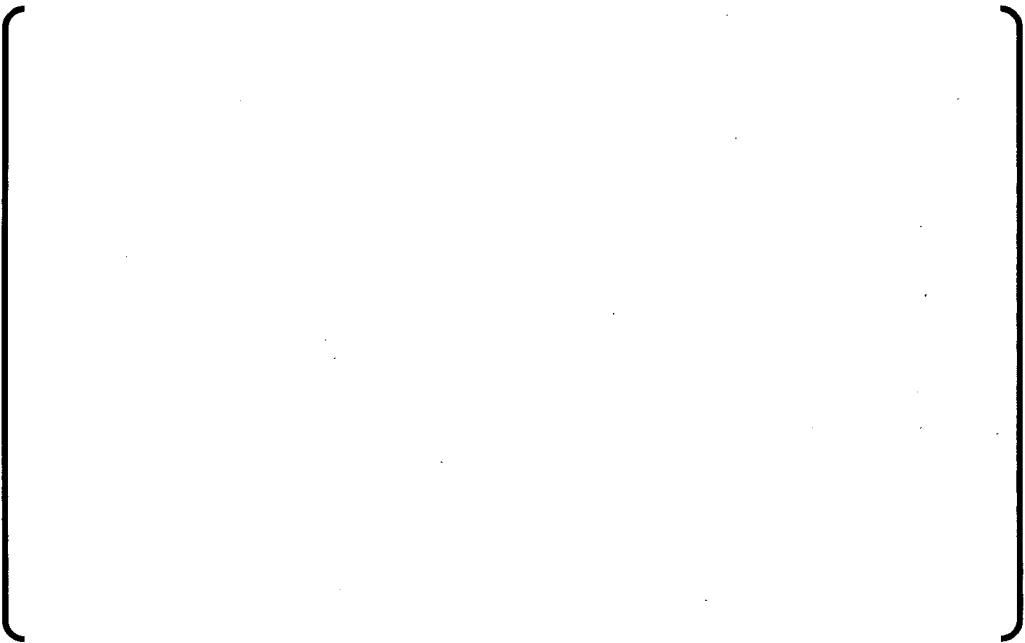


Figure 29b-4 Measured / Calculated (Predicted) diameter change versus measured diameter decrease



Figure 29b-5 Measured - Calculated (Predicted) diameter change versus measured diameter decrease

RAI 30

The following questions relate to understanding the FGR (FGR) model in Section 4.2.2.1.

- a. How is C_{i-1} used in equation 4.2.2.1-2 determined?
- b. How is the production rate of 30 atoms per 100 fissions converted to the value used in β in mol/cm³/hr?
- c. Is the term F_{ri} (eq. 4.2.2.1-9) applied to every radial pellet ring where burn-up is greater than 62.2 GWd/MTU, or only to those that have been previously identified to be within the rim region?
- d. Equation 4.2.2.1-9 describes how the fraction of FGR is calculated for each pellet ring. How are these fractions combined to calculate the fraction of FGR from each axial segment, and how are the fractions released from each axial segment combined to calculation the fraction of FGR from the entire rod?

RAI 30 RESPONSE

- RAI 30a

C_{i-1} is the concentration (mol/cm³) of the fission gas accumulated in the pellet ring at time t_{i-1} . The fission gas contained within a pellet ring is initialized to zero at the beginning of life. If there has not been any fission gas release from the pellet ring, the fission gas accumulated in the pellet ring at t_{i-1} is given by the sum of the fission gas production rate in each time step multiplied by the time step duration:

No prior fission gas release:
$$C_{i-1} = \sum_{j=1}^{i-1} \beta_j \cdot \Delta t_j \quad (\text{eq. 30-1})$$

On the other hand, if fission gas is released in the time step from t_{i-2} to t_{i-1} , C_{i-1} is calculated using Eq. 4.2.2.1-2 of Reference 9a-1 (with i replaced by $i-1$):

$$\Delta RD_{i-1} = \beta_{i-1} \cdot \Delta t_{i-1} - \left(C_{i-1}^* + \frac{\beta_{i-1}}{KD_{i-1}} - C_{i-2} \right) \{ 1 - \exp(-KD_{i-1} \cdot \Delta t_{i-1}) \} \quad (\text{eq. 30-2})$$

where

- ΔRD_{i-1} : fission gas release during Δt_{i-1} (mol/cm³)
- β_{i-1} : fission gas production rate during Δt_{i-1} (mol/cm³/hr)
- C_{i-2} : accumulated fission gas concentration in grain at t_{i-2} (mol/cm³)
- C_{i-1}^* : Retainable fission gas in the grain boundary at t_{i-1} (mol/cm³)
- KD_{i-1} : fission gas release rate per unit time at t_{i-1} (/hr)

to obtain the diffusion release during this time step, with ΔRD_{i-1} and KD_{i-1} calculated using Eqs. 4.2.2.1-3 and 4.2.2.1-4 of Reference 9a-1. Eq. 4.2.2.1-5 of reference 9a-1 is used to calculate the release due to recoil and knockout during this time step, ΔRK^{i-1} , and Eq. 4.2.2.1-8 of Reference 9a-1 is used to calculate the release from the Rim region during this time step, $\Delta F_{rim\ i-1}$. These calculations are performed for each pellet ring in each axial segment. C_{i-1} is then calculated using

$$\left[\quad \quad \quad \right] \quad (\text{eq. 30-3})$$

where

$PROD_{i-2}$: the produced fission gas up to step $i-2$; $PROD_{i-2} = \sum_{j=1}^{i-2} \beta_j \cdot \Delta t_j$

$\Delta PROD_{i-1}$: the produced fission gas during step $i-1$; $\Delta PROD_{i-1} = \beta_{i-1} \cdot \Delta t_{i-1}$

$RELEASE_{i-2}$: the total fission gas released up to step $i-2$

ΔRD_{i-1} : fission gas release during Δt_{i-1} due to diffusion release

ΔRK^{i-1} : fission gas release due to recoil and knockout during step $i-1$

$\Delta F_{rim,i-1}$: fission gas release from the Rim region during step i-1

In this way the total fission gas production and the total fission gas release up to the current time step are calculated and stored in the FINE code. These values are then used to calculate the diffusion fission gas release rate in the current time step, from t_{i-1} to t_i .

- RAI 30-b

The basic equation is :

$$\beta = HFLX \cdot SURFAREA \cdot \frac{1}{HGRT} \cdot \frac{1}{R} \cdot \frac{1}{VOL} \left[\quad \right] \quad (\text{eq. 30-4})$$

where

β : fission gas production rate (mol/cm³/hr)

HFLX : heat flux (BTU/ft²/hr)

HGRT : heat generation per fission (BTU/fission). The FINE code assumes [] MeV per fission as a default value.

SURFAREA : heat exchange surface area (ft²)

R : Avogadro number (n/mol)

VOL : fuel volume (cm³)

The β value for each ring in each axial segment is calculated by weighting the volume of each ring by the volume of the whole axial segment, and taking into account the radial power distribution:

$$\beta_i = \beta \cdot \frac{RINGVOL}{VOL} \cdot NRM.PWRDIST \quad (\text{eq.30-5})$$

where

β_i : fission gas production rate in ring i (mol/cm³/hr)

RINGVOL : Ring volume (normally 10 equal volume pellet rings in each axial segment) (cm³)

NRM.PWRDIST : Normalized radial power distribution (ratio of ring power to segment power)

- RAI 30c

The FINE code calculates the Rim fission gas release for each pellet ring for which the ring average burnup exceeds the Rim threshold burnup of 62.2 GWd/MTU and the ring average temperature is less than [] deg.F. Normally the burnup at the pellet periphery is much higher than in the interior of the pellet, and the fission gas release due to the Rim release model is limited to the pellet peripheral region.

- RAI 30d

As described above, both the produced and released fission gas are calculated for each ring in each axial segment. When the FINE code calculates the total fission gas release fraction from the fuel rod, both the produced and released fission gases are accumulated from all the rings in all the segments, and the total fission gas release fraction is calculated as the ratio of the total fission gas release to the total fission gas produced. The rod total fission gas release fraction in time step i is therefore calculated as:

$$FGR_i = \frac{ACCUMRELEASE_i}{ACCUMPROD_i} \quad (\text{eq.30-6})$$

where

(in case of the equal segment volume and the equal ring volume)

$$ACCUMPROD_i = \sum_{j=1}^i \sum_{seg=1}^{NT} \sum_{ring=1}^{10} (\beta_{seg,ring} \cdot \Delta t_j)$$

$$ACCUMRELEASE_i = \sum_{j=1}^i \sum_{seg=1}^{NT} \sum_{ring=1}^{10} (\Delta RD_{seg,ring,j} + \Delta RK_{seg,ring,j} + \Delta Frim_{seg,ring,j})$$

RAI 31

For the helium model described in Section 4.2.2.2, how is the helium solubility model used to determine the amount of helium present in the fuel rod free volume?

RAI 31 RESPONSE

The Helium in the rod void volume is calculated using the Helium generation, release and absorption models described in Section 4.2.2 of Reference 9a-1. The helium solubility model reduces the amount of helium in the rod, so that the mols of He in the rod is given by

He (accounting for solubility) = He (without solubility) – So*(Fuel mass in grams)

where So is the solubility.

The quantity He (without solubility) is the sum of the initial helium in the rod from the pre-pressurization during fabrication and the helium generated by fission and released to the fuel rod void volume. The helium generated by fission and released to the fuel rod void volume is calculated from the Reference 9a-1 equations 4.2.2.2-1 and 4.2.2.2-2, as described in Section 4.2.2 of Reference 9a-1. The application of the helium model uncertainty in the evaluation of the rod internal pressure lift-off criterion is obtained by considering an uncertainty case that uses the upper bound Helium model, as shown in the response to RAI 9e.

RAI 32

Table 4.2.6-1 notes that a given percentage of the fuel volume is void volume due to pellet chamfer and pellet chips. How is the volume attributed to pellet chips determined and how does this compare to that calculated from the chamfer? Provide specific data on how this volume from pellet chips is determined. (see RAI numbr 37)

RAI 32 RESPONSE



RAI 33

The code verification and validation data for fuel temperatures utilizes a significant number of rods that were irradiated between 30 and 40 years ago. These were state of the art irradiations and temperature measurements 30 years ago but there are much better characterized Halden irradiations available at this time. In addition, the other rods used for verification, other than the two rods from IFA-562, are all unknown to PNNL and NRC and appear to be between 10 to 20 years old. Also, the data set used to verify the fuel temperatures for UO₂-Gd₂O₃ fuel is limited to only 3 rods. The following request would extend the verification and validation database for FINE using additional Halden rods irradiated at high power (lower burnups), at moderate powers up to high burnups and additional gadolinia rods with measured fuel temperatures. This additional data will also provide a better estimate of code calculational uncertainties in temperature as a function of burnup and power.

- a. In relation to verification and validation at high powers and low burnup provide FINE temperature predictions of the IFA-677.1 Rods 2 and 6 (most recent data provided in HWR-819) and the IFA-681 Rods 1 and 5 (most recent data provided in HWR-832). Fuel centerline temperature predictions and data should be plotted versus time or burnup.
- b. In relation to verification and validation at high burn-up levels, provide FINE temperature predictions of IFA-597.3 Rod 8 that was irradiated up to moderate rod powers at a burn-up of ~ 70 GWd/MTU and IFA-515 Rods A1 and B1 that were irradiated to low powers but burn-ups extended up to 80 GWd/MTU. The IFA-597.3 Rod 8 test also measured FGR by rod puncture so this rod can be used to verify both fuel temperatures and FGR at relatively high local burn-ups; provide predicted FGR for this rod. Fuel centerline temperature predictions and data should be plotted versus time or burn-up.
- c. In relation to verifying and validating predicted fuel temperatures for UO₂-Gd₂O₃ fuel provide FINE temperature predictions of IFA-636 Rods 2 and 4 that were irradiated up to 25 GWd/MTU (data provided in HWR-817) and of IFA-681 Rods 2, 4 and 6 (data provided in HWR-832). Fuel centerline predictions and data should be plotted versus time or burnup.
- d. The uncertainty in the FINE prediction appears to increase with increasing linear heat generation rate (Figure 4.3.1.1-2) such that the constant upper-bound value used by FINE may not bound the higher heat rate data with a high degree of confidence. This is of particular concern because most licensing analyses are performed at the higher linear heat generation rates. Provide measured-minus-predicted fuel temperature versus linear heat generation rate and burnup for each set of rods in a., b. and c. above, similar to the plots in Figures 4.3.1.1-1 and 4.3.1.1-2 (separating out UO₂ and UO₂-Gd₂O₃ rods) and include the FINE assumed upper-bound uncertainty in these figures. Recalculate the standard deviation, mean and upper-bound for all of the fuel centerline temperature data including those in a., b., and c. above.
- e. Calculate the standard deviation, mean and upper-bound for only those measured temperature data above 1300°C and plot predicted- minus- measured versus fuel burnup for this high temperature data

RAI 33 RESPONSE

- RAI 33a

MHI will provide the results by 30th January 2009.

- RAI 33b

MHI will provide the results by 30th January 2009.

- RAI 33c

MHI will provide the results by 30th January 2009.

- RAI 33d

MHI will provide the results by 30th January 2009.

()

- RAI 33e

MHI will provide the results by 30th January 2009.

RAI 34

The code verification data for FGR contains a large quantity of data with a mixture of high and older moderate quality data. The use of this data set leads to several observations, comments, and requests. Some of the moderate quality data with high release (>5 percent) is underpredicted by an amount greater than the upperbound uncertainty used for FINE predictions. In addition, the FINE code predictions versus burn-up appear to follow the Vitanza threshold versus burn-up (Figure 4.2.3.3-3); however, Halden in recent years has discovered that the Vitanza model underpredicts the threshold in rods with local burn-ups greater than 50 GWd/MTU. The IFA-429 Rod DH predicted and measured gas release values (based on in-reactor pressure) are based on old data while more recent experimental data (end-of-life puncture FGR) is available for this rod than that presented in the submittal. Finally, there are three sets of high quality data that are absent from the FINE verification database. Therefore, to supplement the provided data and analyses, provide predictions of FGR for the following rods

- a. Two Babcock & Wilcox Co. segmented fuel rods that were irradiated in Arkansas Nuclear Unit 1 to 62 GWd/MTU burn-up and then power ramp tested in Studsvik R2 resulting in measured cladding deformation and FGR following the power ramp (data presented in Proceedings of 1994 ANS International Topical Meeting on Light Water Reactor Fuel Performance, West Palm Beach, Florida, p. 343).
- b. Halden IFA-597.3 Rod 8 that was re-fabricated by Halden from a BWR fuel rod commercially irradiated in Ringhal's 1 to ~68 GWd/MTU at discharge and then re-irradiated in Halden to ~71 GWd/MTU at a moderately high linear heat generation rate between 21 to 31 Kilowatts per meter for this high burn-up level (see RAI number 9.b above). The latter rod was a boiling water reactor (BWR) rod but the difference between BWR and pressurized water reactor (PWR) rods is not significant at this burn-up level because the fuel-cladding gap is closed and this data is particularly valuable because fuel temperatures were measured as well as FGR.
- c. Halden IFA-534.14 Rods 18 and 19 were irradiated in Gosgen PWR to ~ 59 GWd/MTU burn-up, re-fabricated with pressure instrumentation, and then re-irradiated in Halden to ~63 GWd/MTU. These two rods had different fuel grain sizes and FGR was measured by rod puncture (data in HWR-558 and in the OECD NEA database).
- d. Provide a revised prediction of the IFA-429 Rod DH based on the latest power history and FGR puncture data (data in HWR-668).
- e. Recalculate the standard deviation, mean and upper-bound for all of the FGR data including those in a., b., c, and d. above.
- f. Calculate the standard deviation, mean and upper-bound for only those with measured release data ≥ 5 percent and plot predicted-minus-measured versus fuel burn-up for this high release data. The peak rod pressure rods in a core usually have predicted release values greater than five percent such that the accuracy of predicting these data is of primary concern.

RAI 34 RESPONSE

- RAI 34a

MHI will provide the results by 30th January 2009.

- RAI 34b

MHI will provide the results by 30th January 2009.

- RAI 34c

MHI will provide the results by 30th January 2009.

- RAI 34d

MHI will provide the results by 30th January 2009.

- RAI 34e

MHI will provide the results by 30th January 2009.

()

- RAI 34f

MHI will provide the results by 30th January 2009.

RAI 35

The code verification data for prediction of cladding strains during power ramps is very limited to only 2 test rods at ~ 30 GWd/MTU. There are several ramp test programs that have measured cladding plastic strains greater than 0.3 percent as a result of power ramping, such as RISØ FGP3 ANF rods, B&W Studsvik, Super-Ramp, and Over-Ramp rods. Provide comparisons of FINE predicted strains to this or other data from rods (such as those from Vandellos) subjected to power ramps with measured plastic strains (hoop and axial) greater than 0.3 percent to verify the code's ability to predict cladding deformation. Identify those rods where gas bubble swelling has contributed to predicted deformation.

RAI 35 RESPONSE

MHI will provide the results by 30th January 2009.

RAI 36

The tables and figures in Section 4.3.3 provide measured and predicted fuel densities. How were the fuel densities measured post-irradiation? The FINE code appears on average to overpredict fuel density. Identify those licensing analyses where an overprediction in density will result in a non-conservative analysis. Discuss how this potential non-conservatism is compensated for in the licensing analysis.

RAI 36 RESPONSE

The fuel density measurement methods are summarized in Table 36-1, which shows measurement methods for the both the pre-irradiation characterization and the post-irradiation densities in Table 4.3.3-1 of Reference 9a-1. The post-irradiation density data have been obtained by either the mercury pycnometry or the liquid immersion methods.

Mercury pycnometry is a volume displacement technique. The sample is put into a sample chamber filled with mercury and the weight of the displaced mercury is measured. Since the volume of displaced mercury is the volume of the sample, the density of the sample can be calculated, as follows:

$$V_s = ((W_2 - W_1) - (W_3 - W_1 - W_s)) / D_{Hg}$$

$$D_s = W_s / V_s$$

W_1 : Weight of the sample chamber without mercury.

W_2 : Weight of the sample chamber with mercury.

W_3 : Weight of the sample chamber including the sample and mercury.

W_s : Weight of the sample.

D_{Hg} : Density of mercury.

V_s : Volume of the sample.

D_s : Density of the sample.

The liquid immersion method is based on Archimedes principle. The weight of the sample is measured in air and in the immersion liquid. Since the volume of the sample is determined from the difference of the weight and the density of the immersion liquid, the density of the sample can be deduced. Meta-xylene, water, bromoform, etc., are used for the immersion liquid.

$$V_s = (W_1 - W_2) / D_L$$

$$D_s = W_s / V_s$$

W_1 : Weight of the sample in air.

W_2 : Weight of the sample in liquid.

W_s : Weight of the sample.

D_L : Density of immersion liquid.

V_s : Volume of the sample.

D_s : Density of the sample.

MHI's Responses to the NRC's RAI on
Topical Report MUAP-07008-P(0)
"Mitsubishi Fuel Design Criteria and Methodology"

UAP-HF-08299-NP (R0)



Table 36-1 Density measurement methods



Table 36-2(1) Pellet Density Measurements and Predictions



Table 36-2(2) Pellet Density Measurements and Predictions



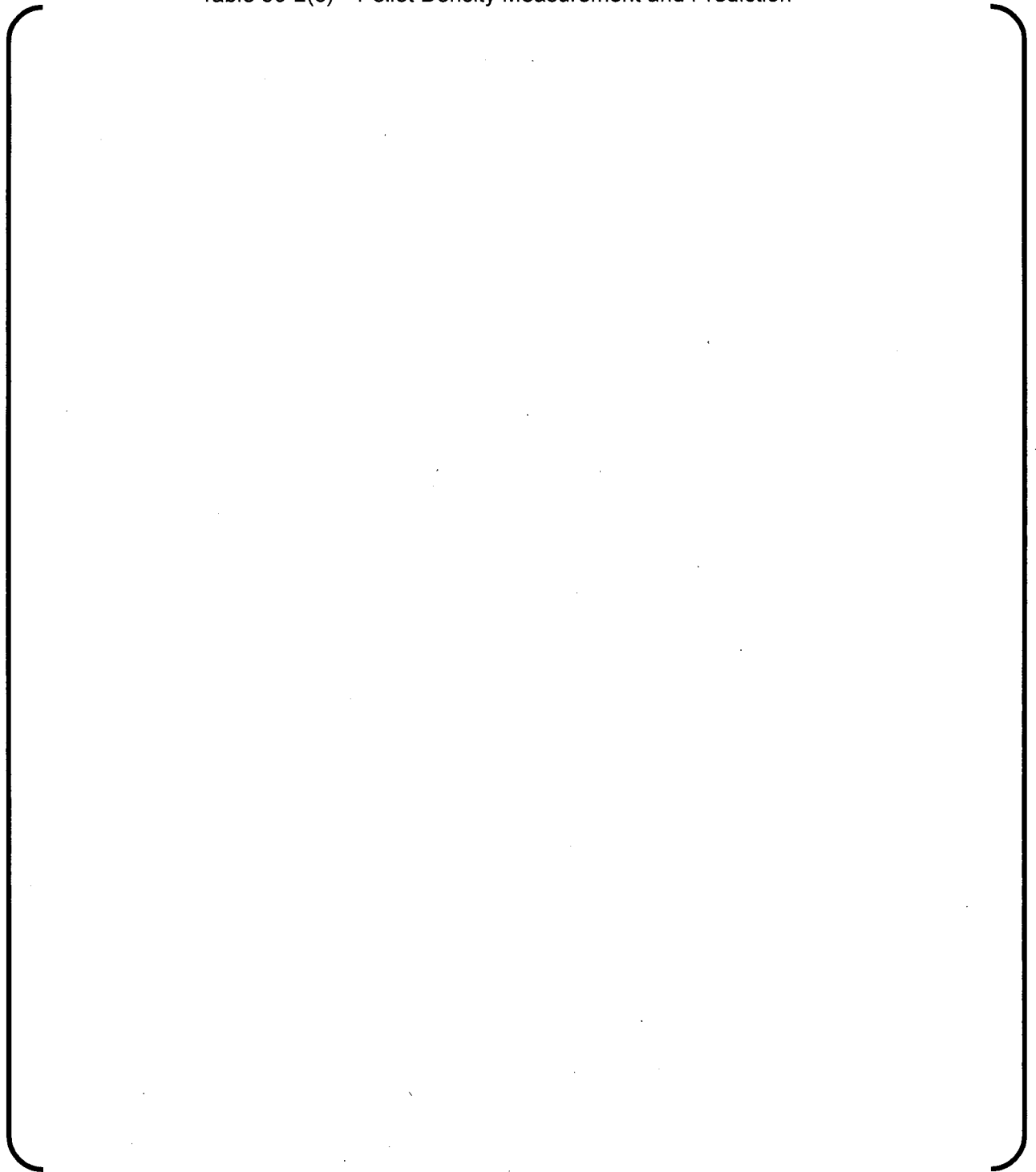
Table 36-2(3) Pellet Density Measurement and Prediction



Table 36-2(4) Pellet Density Measurement and Prediction



Table 36-2(5) Pellet Density Measurement and Prediction



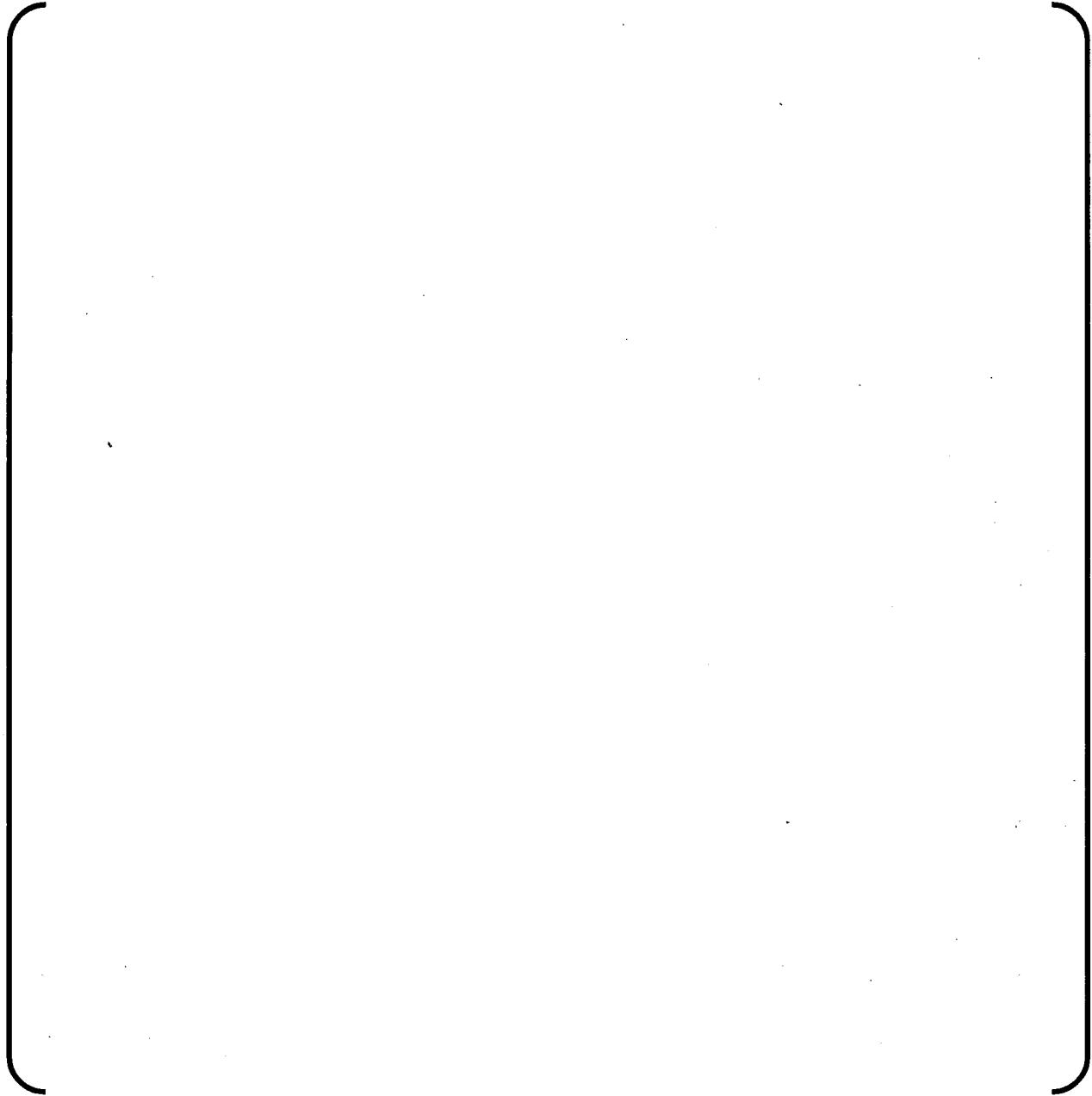


Table 36-3 Density bias effect on licensing analyses

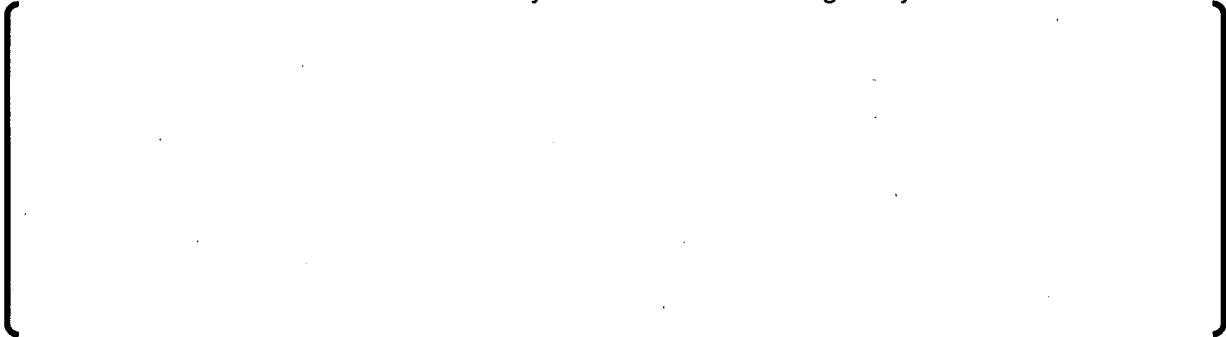
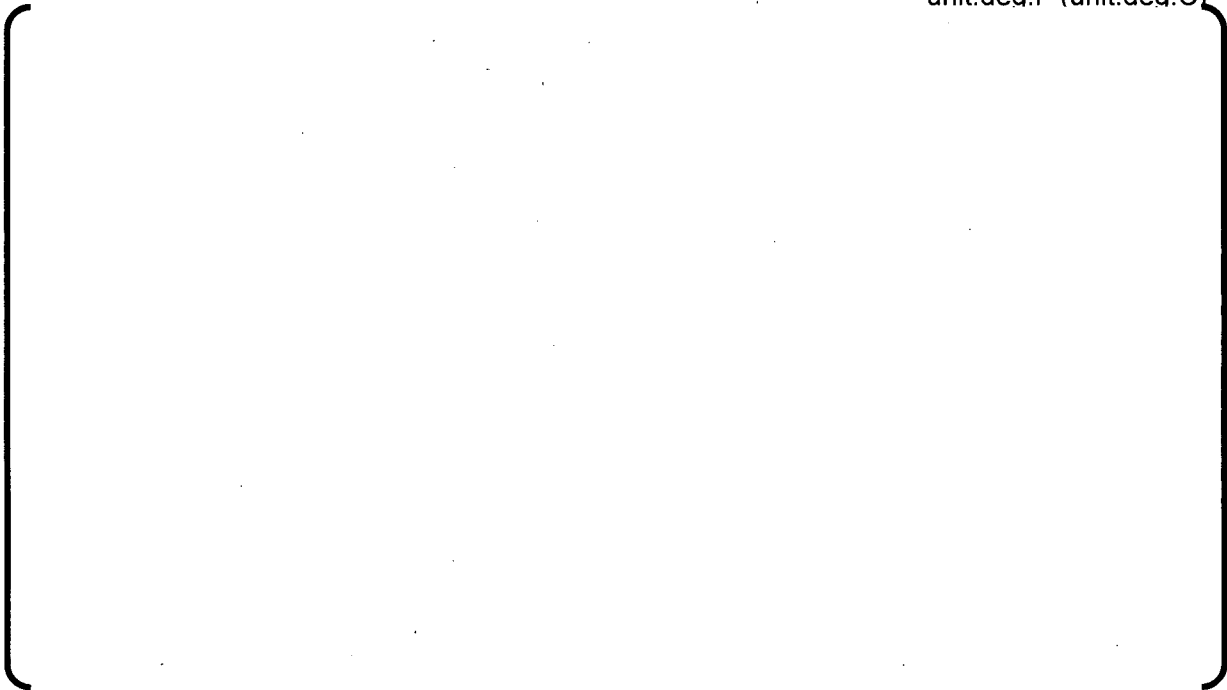


Table 36-4 Density bias effect on fuel centerline temperature uncertainties

unit:deg.F (unit:deg.C)



QUESTION-37

Provide those void volume and rod pressure data and FINE comparative predictions that are from full length commercial rods. Discuss how these measurements are performed on commercial fuel rods post-irradiation. Also, demonstrate that the uncertainty in the void volume predictions of commercial rods are covered by the uncertainty in those parameters used in licensing analyses that impact void volume predictions, such as fabrication, creep, fuel swelling, and axial rod growth account for the uncertainty observed in the void volume predictions.

RESPONSE-37

The measurement principle of the void volume and rod pressure is outlined below.

A schematic of the measuring system is shown in Figure 37-1. The system consists of two chambers (Chamber A and Chamber B), two valves (Valve A and Valve B), two thermometers (Thermometer A and Thermometer B) and one pressure gauge. As shown in Figure 37-1, the each volume of the components in this system are defined by the following variables.

V_x:fuel rod void volume

V_A:system volume from Chamber A to Valve A

V_B:system volume from ValveA to ChamberB and ValveB

The procedure of the measurement involves the following steps.

1. The entire system is evacuated.
2. The rod is punctured after the Valve A is closed and then the rod gas is expanded for Chamber A. Pressure and temperature are measured until the pressure equilibrates. The equilibrium pressure and temperature measured from Pressure Gauge and ThermometerA is recorded as P₁ and T₁, respectively. In this step, the rod gas is expanded in the volume of V_x and V_A.
3. The ValveA is opened after the ValveB is closed and then the rod gas is expanded for Chamber B. Pressure and temperature are measured until the pressure equilibrates. The equilibrium pressure and two temperatures measured from Pressure Gauge, Thermometer A and B is recorded as P₁, T₁ and T₂, respectively. In this step, the rod gas is expanded in the volume of V_x, V_A and V_B.
4. The fuel rod void volume is calculated by the following equation.

$$\frac{P_1(V_A + V_x)}{T_1} = \frac{P_2(V_A + V_x)}{T_2} + \frac{P_2V_B}{T_3}$$

$$\therefore V_x = \frac{\frac{P_2V_A}{T_2} + \frac{P_2V_B}{T_3} - \frac{P_1V_A}{T_1}}{\frac{P_1}{T_1} - \frac{P_2}{T_2}}$$

This equation is derived from the ideal gas equation.

5. The rod pressure is calculated by the following equation.

$$\frac{P_0 V_x}{T_0} = \frac{P_1 (V_A + V_x)}{T_1}$$
$$\therefore P_0 = \frac{P_1 \left(\frac{V_A + V_x}{V_x} \right)}{\frac{T_1}{T_0}}$$

Where, P_0 :Rod pressure, T_0 :Rod temperature

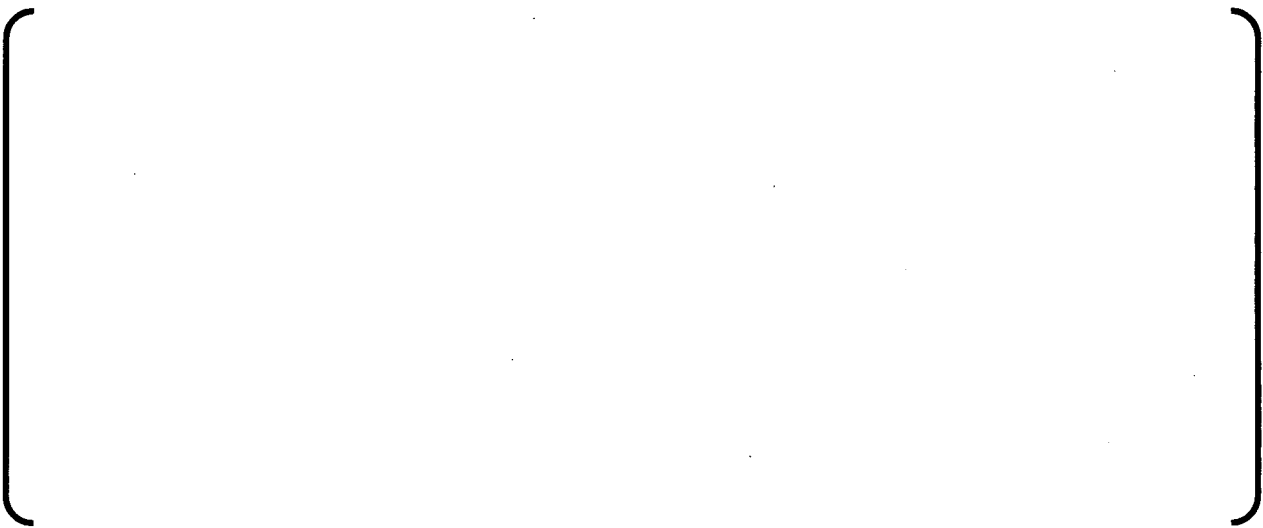


Table 37-1 (1) Void volume and pressure from full length commercial rods



Table 37-1 (2) Void volume and pressure from full length commercial rods

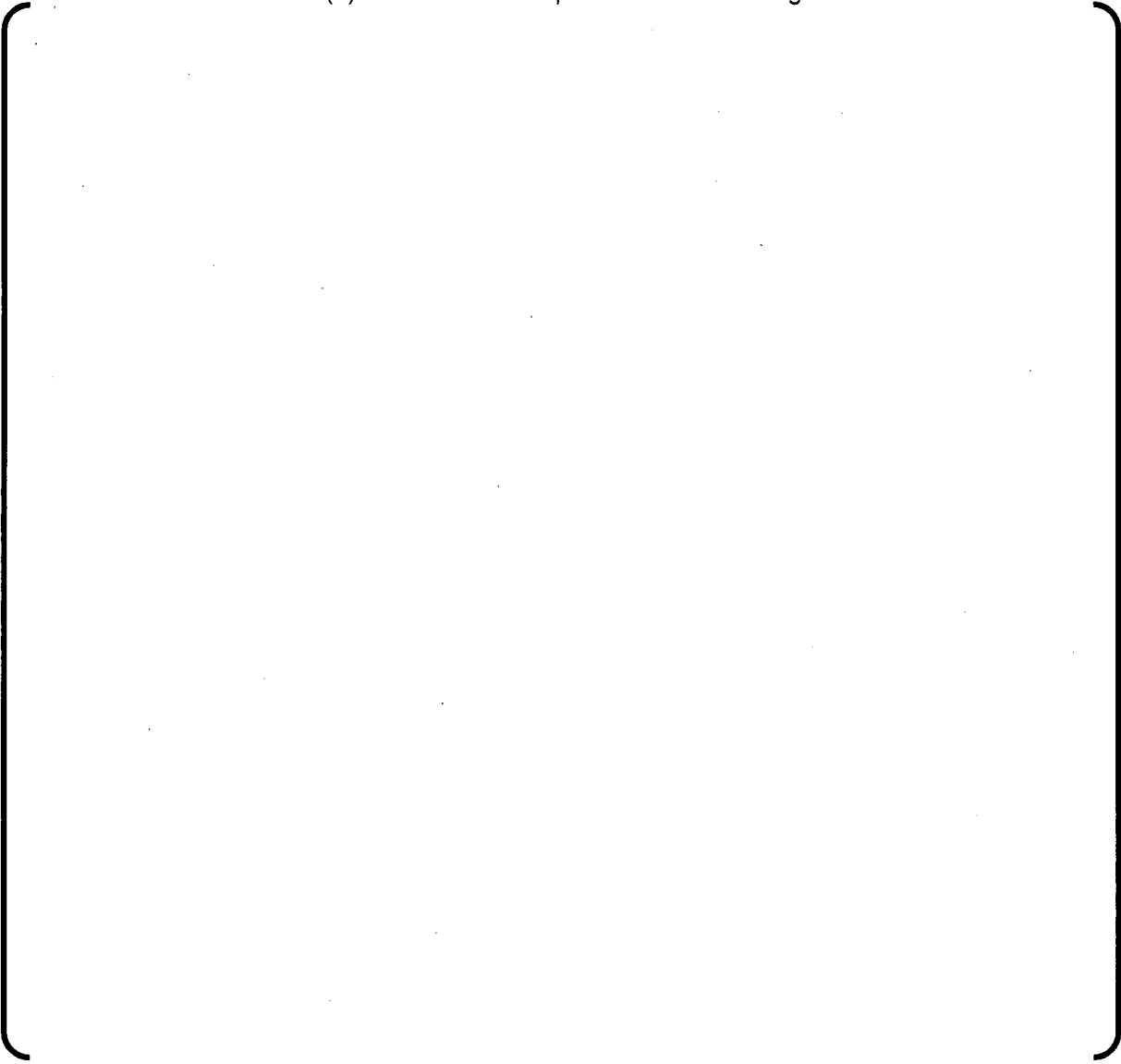
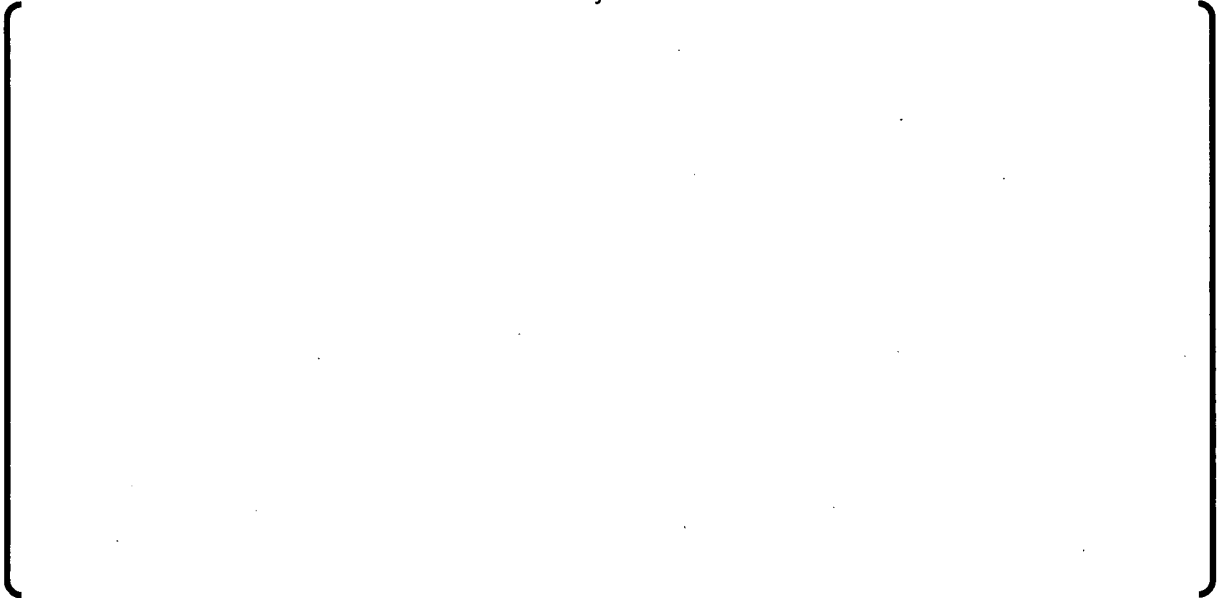


Table 37-2 Uncertainty Calculation of ZORITA 386



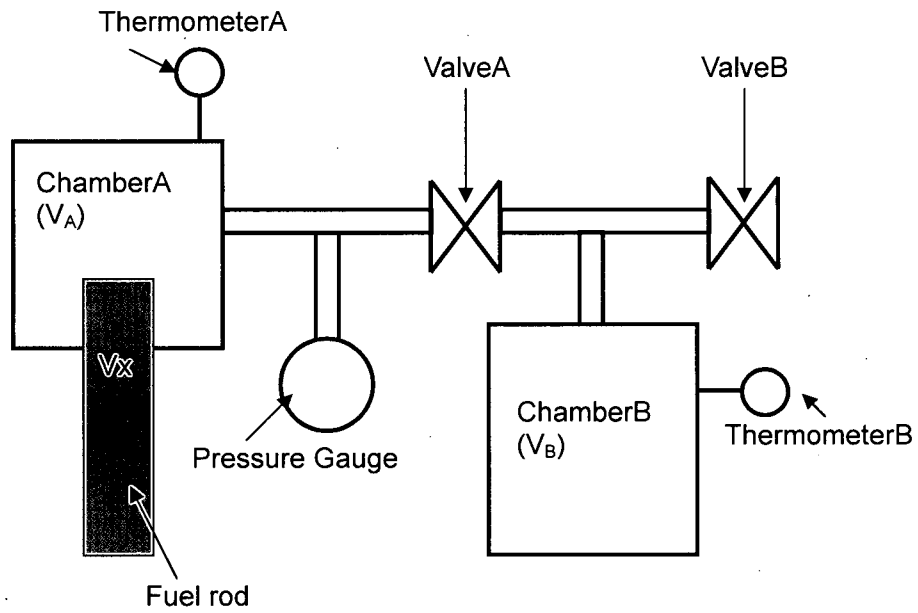


Figure 37-1 Fuel rod puncturing and fission gas collection systems

RAI 38

Section A.3.2.2.f discusses the fuel rods from Vandellos that achieved peak rod average burnups of 75 GWd/MTU. However, there is no FGR, cladding deformation, cladding corrosion, cladding hydrogen or rod growth data provided in the submitted report near this maximum burnup level. The current cladding corrosion, hydrogen, and rod growth data are only at burnup levels near 55 GWd/MTU while it has been requested to provide code approval to 65 GWd/MTU. Provide these higher burnup data along with FINE predictions of these data. Provide any additional FGR, oxide thickness, hydrogen and rod growth data that has been obtained since the submittal of this report that are applicable to validation of the FINE models. Also, are the oxide thickness, hydrogen and growth data from Ohi Unit 4 high burnup lead use assemblies (LUAs) (discussed in Section A.3.2.2.g) presented in this submittal with FINE predictions? If so, identify these data in Section 4. If not, provide those data taken from these LUAs along with the FINE predictions.

RAI 38 RESPONSE

As stated in the response to RAI 19a, MHI will change the burnup applicability range requested for the licensing of the FINE code to 62 GWd/MTU to be consistent with the US-APWR fuel design maximum rod burnup of 62 GWd/MTU.

It is possible to add the data of Vandellos rods irradiated for a fifth cycle, to up to approximately 75 GWd/MTU, to the FINE code validation database. However, as described below, these rods had been subjected to an atypically high power in their fifth cycle of irradiation, and the use of the data obtained from these high burnup Vandellos 2 rods requires a careful evaluation of the impact of this atypically high power in the fifth cycle on the fuel rod performance data obtained from these rods.

Oxide thickness, hydrogen content, pellet density, FGR, helium content, rod internal pressure, and rod growth data from the Ohi Unit 4 LUAs have already been included in the comparisons between the measured data and the FINE code predictions. The Ohi Unit 4 LUA data used in these comparisons have the rod ID prefix 04X1-KON4 in the data given in Reference 9a-1 Tables 4.3.2-1, 4.3.3-1, 4.3.4-1, 4.3.5-1, 4.3.6-1 and 4.3.7-1.

Some additional rod growth data from the Japanese commercial plants, Ikata Unit 1 and Ohi Unit 4, have become available since the Reference 9a-1 submittal. These additional data are shown in Figure 38-12 in this RAI response.

1. Vandellos Unit 2 Irradiation Programs

MHI has had three cooperative irradiation programs in the Vandellos Unit 2 reactor: the Segmented Rod Program, the Extension Irradiation Program, and the High Burnup Program. Brief descriptions of the relevant features of these three programs are:

(1) Segmented Rod Program and Extension Irradiation Program

The Segmented Rod Program started in 1991 and completed in 2001, achieving a maximum rod average burnup of about 57 GWd/MTU after 4 cycles of irradiation at Vandellos Unit 2. Both ZIRLO and MDA claddings were irradiated in the Segmented Rod program. The Segmented Rod program was followed by the Extension Irradiation Program, in which some of the rods from the Segmented Rod Program were transferred to a once burned fuel assembly, and irradiated for an additional fifth cycle of irradiation. Due to the higher reactivity of the neighboring fuel rods in this once burned assembly, the power and burnup gain of the rods in the Extension Irradiation Program was atypically high for fuel at these high burnups. Figure 38-1 shows the assembly powers for the fuel irradiated in the Extension Irradiation Program⁽³⁸⁻¹⁾.

(2) High Burnup Program

The High Burnup Program was irradiated in cycles 12 through 15 of Vandellos Unit 2, after the Extension Irradiation Program had been completed. Fuel rods with MDA cladding were irradiated for 4 cycles in the High Burnup Program, achieving a peak rod average burnup of approximately 70 GWd/MTU. These high burnups were achieved with the fuel irradiated in the same assembly throughout life, and the High Burnup Program fuel did not experience atypically

high rod powers in its last two cycles of irradiation. The power histories for all the High Burnup Program fuel rods are shown in Figure 38-2. Comparisons between the high burnup MDA cladding performance data from the Irradiation Extension Program and the High Burnup Program can therefore be used to assess the effect of the atypically high rod power of the Extension Irradiation Program fuel in its fifth cycle on oxide thickness, hydrogen content, FGR, and rod growth.

The Vandellos Unit 2 irradiation histories for the Segmented Rod Program, the Extension Irradiation Program and the High Burnup Program are summarized in Table 38-1.

Figure 1. Average power history of fuel assemblies with rods from the program

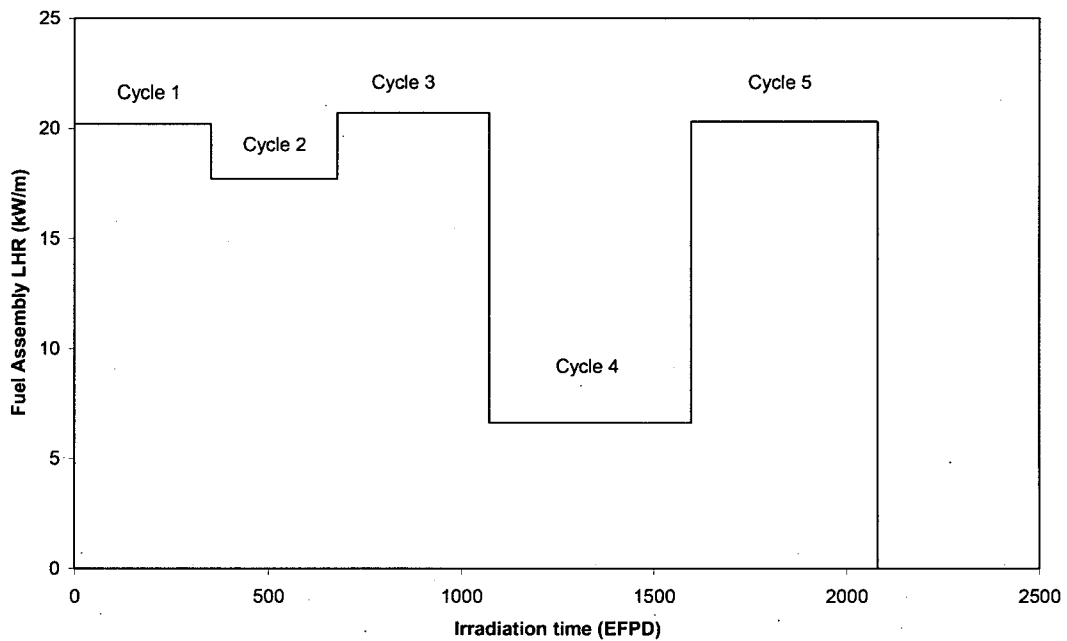


Figure 38-1 Average power history of Segmented Rod and Extension Irradiation Program fuel assemblies ⁽³⁸⁻¹⁾

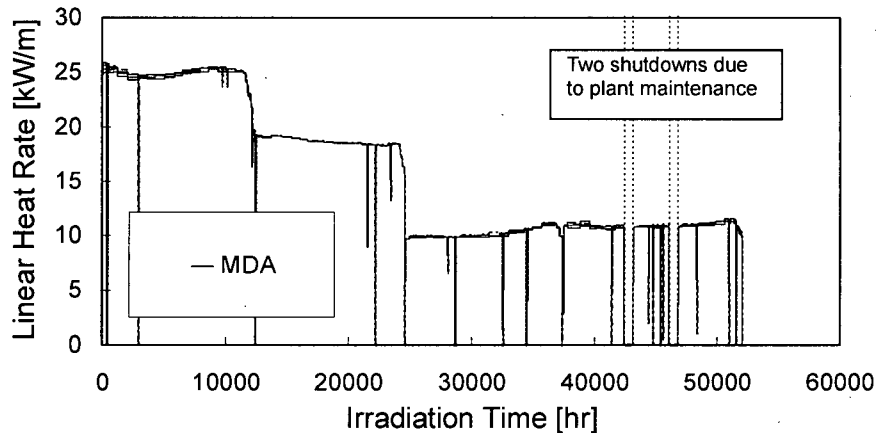


Figure 38-2 Power history of a rod with MDA cladding in the Vandellos Unit 2 High Burnup Program ⁽³⁸⁻²⁾

Table 38-1 Vandellos Unit 2 irradiation histories of the MHI irradiation programs



(3) Fuel Rod Performance Data Obtained in the Vandellos Unit 2 Irradiation Programs

Figures 38-3, 38-4, 38-5 and 38-6 show the cladding oxide thickness, fuel rod growth, fission gas release and hydrogen content data, respectively, obtained in these three Vandellos Unit 2 irradiation programs. The data for MDA cladding shown in Figures 38-3 and 38-4 have been included solely for the purpose of evaluating the impact of the atypically high power in the fifth cycle on the performance of the ZIRLO cladding fuel rods in the Extension Irradiation Program. As shown in Figure 38-5, some of the rods in the program were subjected to the additional irradiation in the R2 reactor in Studsvik, Sweden for ramp tests and for boiling capsule irradiation. The data in Figure 38-6 are consistent with those in Figure 38-3.



Figure 38-3 Corrosion data obtained in the Vandellos Unit 2 irradiation programs ^{(38-2),(38-3)}



Figure 38-4 Fuel rod growth data obtained in the Vandellos Unit 2 irradiation programs ^{(38-2),(38-3)}

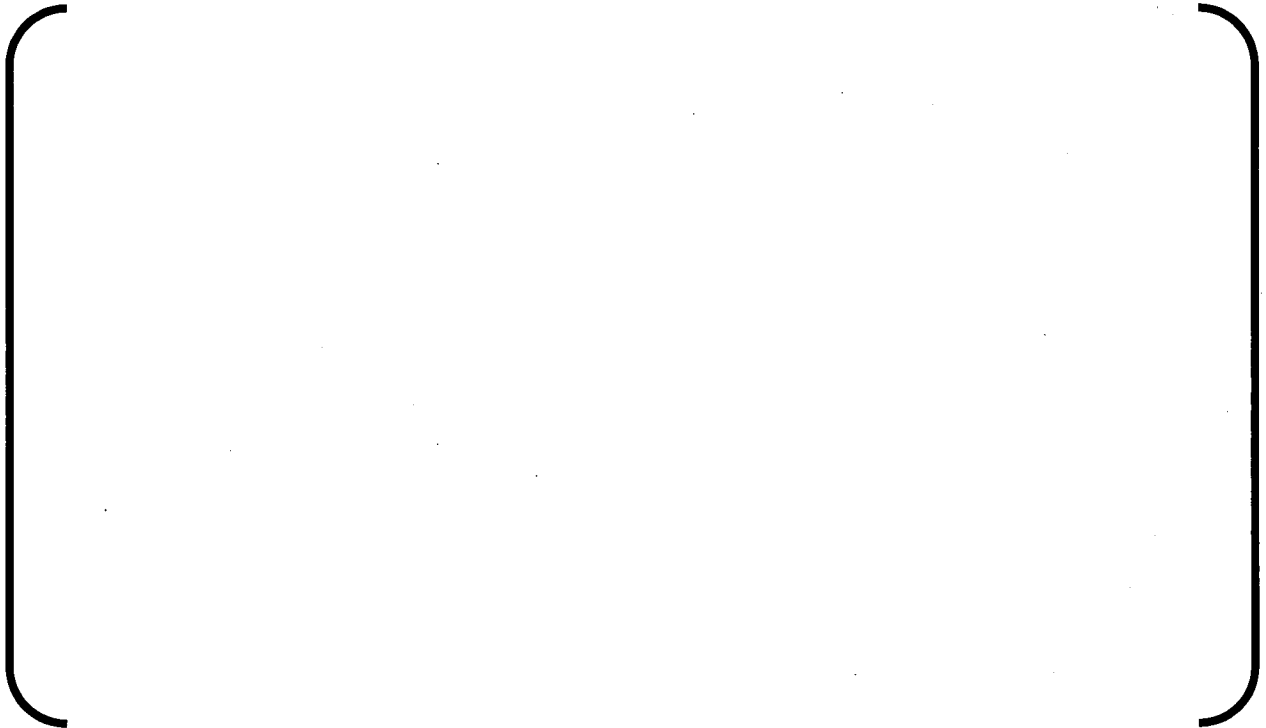


Figure 38-5 Fission gas release data obtained in the Vandellos Unit 2 irradiation programs

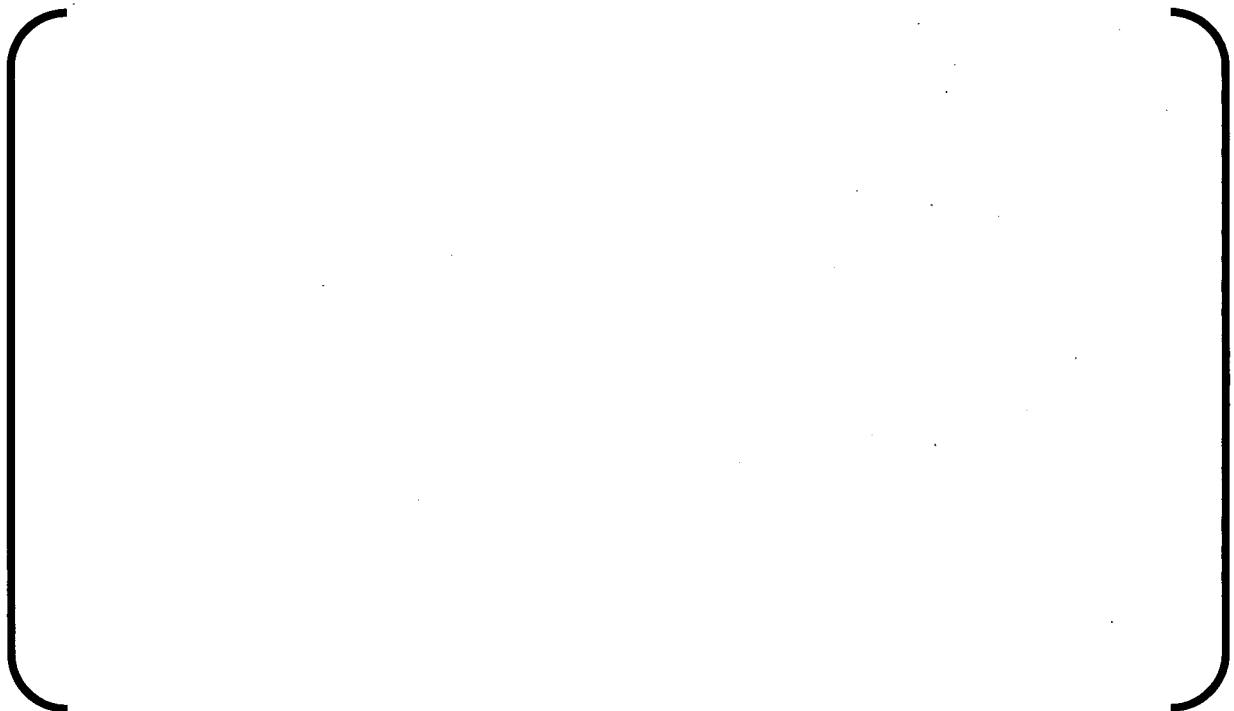


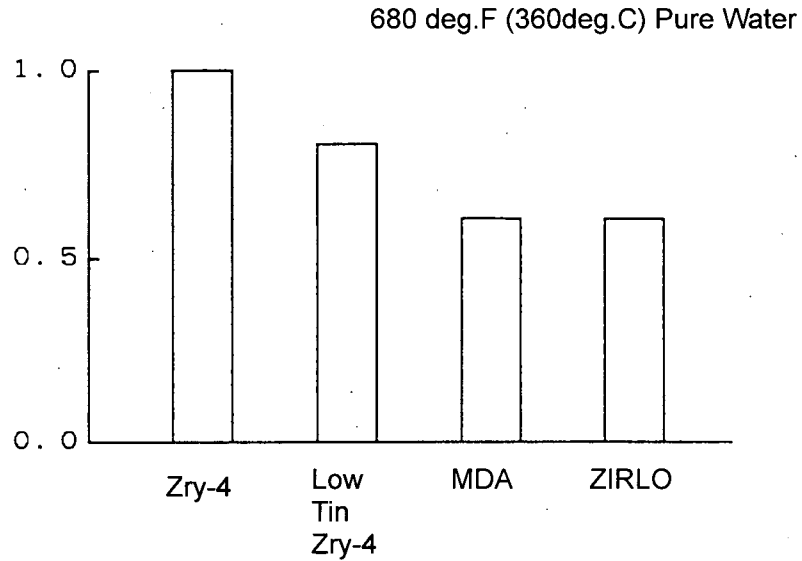
Figure 38-6 Hydrogen content data obtained in the Vandellos Unit 2 irradiation programs

2. Evaluation of the Cladding Corrosion Data

The FINE code corrosion model for ZIRLO has been developed from the FINE code Zry-4 corrosion model. The FINE code Zry-4 corrosion model has been verified with data up to 63 GWd/MTU burnup and oxide thicknesses up to 116 μm (4.6 mils). It is considered that the FINE code Zry-4 corrosion model is applicable within this data range.

The FINE code model for ZIRLO cladding corrosion is based on applying a multiplier to the Zry-4 corrosion rate. This multiplier is based on out-of-pile corrosion test results, which show that the corrosion resistance of ZIRLO is better than Zry-4, as shown in Figure 38-7. In addition, in the ZIRLO corrosion model the second transition, at the oxide weight gain WB, occurs at a lower value of WB { } compared with the value of { } used in the Zry-4 corrosion model. This additional change has been made because it is believed that this second transition is caused by a corrosion rate enhancement due to the hydrogen concentration at the cladding surface. The relation between the corrosion rate and hydrogen content for ZIRLO is consistent with that of Zry-4, as shown in Figure 38-8. Since ZIRLO has a higher hydrogen pickup fraction, 15%, compared with the 12% hydrogen pickup fraction for Zry-4 cladding, the threshold for the second transition has been reduced by a factor of 12/15 from the value used in the Zry-4 corrosion model.

Relative corrosion rate*



* Relative corrosion rate normalized to the rate of Zry-4
The corrosion rates are derived from the out-pile
corrosion test result from 180 to 780 days.

Figure 38-7 Out-of-pile corrosion test results

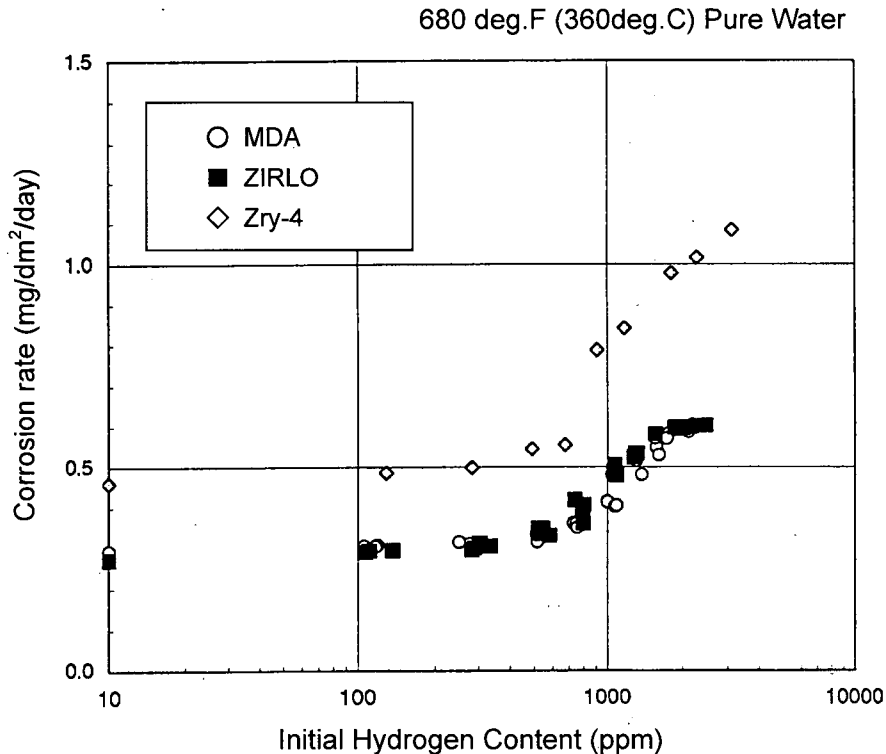


Figure 38-8 Relationship between corrosion rate and hydrogen content

The comparison between the FINE code ZIRLO corrosion model and the Extension Irradiation Program corrosion data is shown in Figures 38-9 and 38-10. The model significantly underpredicts the Extension Irradiation Program corrosion data. However, significant CRUD deposition was observed on the Extension Irradiation Program rods. A sensitivity study has been made to assess the impact of enhanced CRUD deposition on the corrosion predictions, and it has been found that agreement between the FINE code ZIRLO corrosion model and the data can be obtained if a CRUD thickness of { } is assumed for the fifth cycle of irradiation. References (38-2) and (38-3) report the existence of CRUD on the Extension Irradiation rods and the High Burnup Program rods after their first two irradiation cycles, but quantitative CRUD thickness data was not obtained in these Programs.

The FINE code ZIRLO corrosion model has also been used to predict the corrosion data for the MDA cladding in the Extension Irradiation and High Burnup Programs. CRUD formation on the High Burnup Program rods was observed after the first two cycles of irradiation, but this CRUD was ultrasonically cleaned from the rods prior to their irradiation for the third and fourth cycles. The comparison between these predictions and the MDA cladding data is also shown in Figures 38-11 and 38-12. Assuming no enhanced CRUD formation in the fifth cycle, the ZIRLO corrosion model underpredicts the Extension Irradiation Program MDA cladding corrosion data; assuming a CRUD thickness of { } the ZIRLO corrosion model is in agreement with the Extension Irradiation Program data; and, assuming no enhanced CRUD formation, the ZIRLO

corrosion model is in agreement with the High Burnup Program corrosion data after three and four cycles of irradiation. The ZIRLO corrosion model underpredicts the High Burnup Program MDA cladding corrosion data for the first two cycles of irradiation due to enhanced CRUD formation on these rods in these two cycles.

MHI has therefore concluded that the high oxide thicknesses measured on the ZIRLO and MDA cladding at the conclusion of the Extension Irradiation Program are anomalous and are caused by enhanced CRUD formation due to the atypically high powers experienced by these rods in their fifth cycle of irradiation. The high burnup cladding corrosion performance of the MDA cladding in the High Burnup Program is considered representative of MDA cladding performance for typical high burnup operating conditions. Since the ZIRLO cladding has the same corrosion performance as the MDA cladding in the Extension Irradiation Program, MHI has also concluded that the ZIRLO cladding corrosion data from the Extension Irradiation Program are not relevant to high burnup ZIRLO cladding corrosion performance for typical high burnup operating conditions.



Figure 38-9 Oxide thickness measured - predicted versus burnup



Figure 38-10 Oxide thickness measured - predicted versus measured oxide thickness

3. Evaluation of the Hydrogen Pickup Data

Hydrogen content measurements on cladding specimens from the Extension Irradiation Program have been done at Studsvik, using the hot extraction method. The results of these measurements are shown in Figure 38-11. The hydrogen pickup rate for the Extension Irradiation Program specimens is consistent with the FINE code 15% best estimate value. These data therefore support the FINE code ZIRLO hydrogen pickup rate model for burnups beyond 62 GWd/MTU.

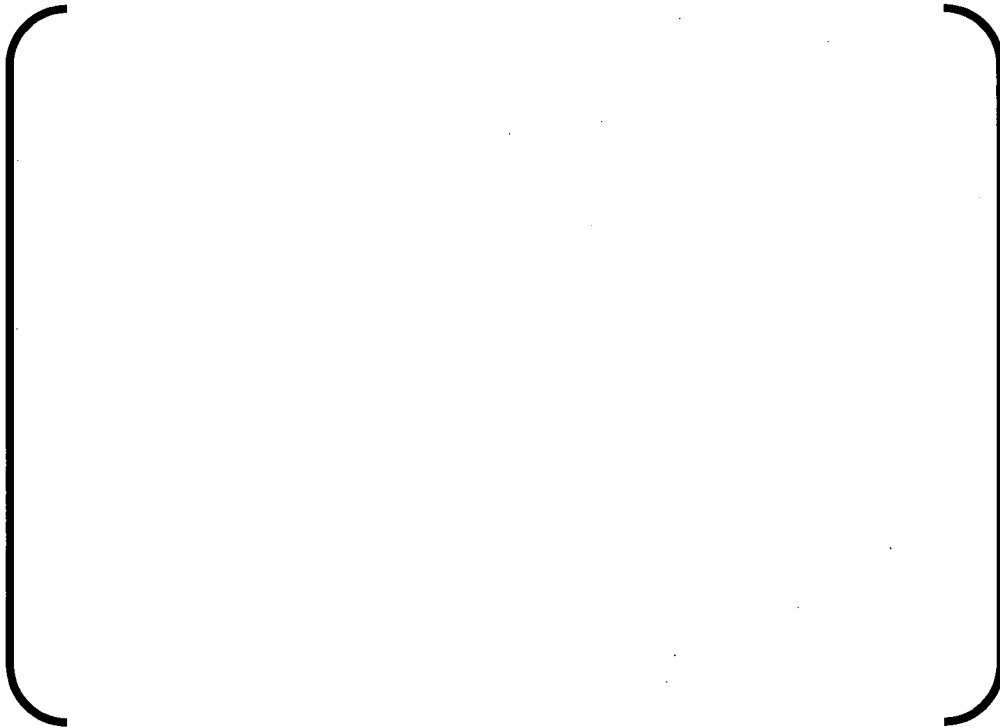


Figure 38-11 Hydrogen pickup rate

4. Evaluation of the Fuel Rod Growth Data

The MHI ZIRLO cladding fuel rod growth data, including the fuel rod growth data obtained in the Vandellos Unit 2 Segmented Rod and Extension Irradiation Programs and the fuel rod growth data recently obtained from the Ikata Unit 1 and Ohi Unit 4 plants, are shown in Figure 38-12. All the data for a fast fluence above 4×10^{25} n/m² are within the bounds of the FINE code ZIRLO cladding fuel rod growth model. The ZIRLO and MDA high burnup fuel rod growth data obtained from the Extension Irradiation Program are above the best estimate ZIRLO fuel rod growth model, but still within the bounds of the model. However, the MDA fuel rod growth data obtained from the High Burnup Program are in excellent agreement with the best estimate ZIRLO fuel rod growth model. This observation implies that the atypical fifth cycle power history for the Extension Irradiation Program affected the fuel rod growth as well as the cladding corrosion, leading to higher fuel rod growth than would occur for typical high burnup fuel operating conditions. Based on this evaluation, MHI has concluded that the FINE code ZIRLO cladding fuel rod growth model is valid for burnups well above 62 GWd/MTU



Figure 38-12 MHI ZIRLO and MDA cladding fuel rod growth data ⁽³⁸⁻³⁾

5. Evaluation of the fission gas release data

Comparisons between the Extension Irradiation Program fission gas release data and the FINE code fission gas release model are shown in Figures 38-13 and 38-14. Figure 38-13 shows the fission gas release measured-to-predicted ratios as a function of burnup and Figure 38-14 shows the fission gas release measured-to-predicted ratios as a function of the measured fission gas release. Results for some of the fission gas release data obtained in the Segmented Rod Program are also shown in these Figures. The FINE fission gas release model tends to underpredict the Extension Irradiation Program fission gas release data, but all but one of these results is within the factor of [] uncertainty for the FINE fission gas release model. In addition, the FINE fission gas release model overpredicts the Segmented Rod Program fission gas release data with measured fission gas releases above 10%. Based on these comparisons, MHI has concluded that the FINE code fission gas release model is applicable to rod burnups beyond 62 GWd/MTU.



Figure 38-13 Fission gas release measured-to-predicted ratios versus burnup



Figure 38-14 Fission gas release measured-to-predicted ratios versus measured fission gas release

REFERENCES

- (1a-1) "US-APWR Fuel System Design Evaluation", MUAP-07016-P (Proprietary) and MUAP-07016-NP (Non-Proprietary), February 2008.
- (1b-1) "Design Control Document for the United States Advanced Pressurized Water Reactor" R1, Mitsubishi Heavy Industries, Ltd., August 2008
- (2-1) "US-APWR Fuel System Design Evaluation", MUAP-07016-P (Proprietary) and MUAP-07016-NP (Non-Proprietary), February 2008.
- (3-1) W.J. O'Donnell and B.F. Langer, "Fatigue Design Basis for Zircaloy Components", Nuclear Science and Engineering 20 pp.1-12, 1964
- (4-1) "US-APWR Fuel System Design Evaluation", MUAP-07016-P (Proprietary) and MUAP-07016-NP (Non-Proprietary), February 2008.
- (5b-1) Nuclear Power Engineering Corporation, Year 2001 Report on Tests of High Burnup Fuels 2001 (PWR High Burnup Fuel Comprehensive Evaluation), March 2002.
- (6-1) "US-APWR Fuel System Design Evaluation", MUAP-07016-P (Proprietary) and MUAP-07016-NP (Non-Proprietary), February 2008.
- (7-1) "US-APWR Fuel System Design Evaluation", MUAP-07016-P (Proprietary) and MUAP-07016-NP (Non-Proprietary), February 2008.
- (8-1) "US-APWR Fuel System Design Evaluation", MUAP-07016-P (Proprietary) and MUAP-07016-NP (Non-Proprietary), February 2008.
- (9a-1) "Mitsubishi Fuel Design Criteria and Methodology", MUAP-07008-P (Proprietary) and MUAP-07008-NP (Non-Proprietary), May 2007

MHI's Responses to the NRC's RAI on
Topical Report MUAP-07008-P(0)
"Mitsubishi Fuel Design Criteria and Methodology"

UAP-HF-08299-NP (R0)

- (10-1) "US-APWR Fuel System Design Evaluation", MUAP-07016-P (Proprietary) and MUAP-07016-NP (Non-Proprietary), February 2008.

- (11-1) F. Garzarolli, et al., "The Main Causes of Fuel Element Failure in Water-Cooled Power Reactors", Atomic Energy Review 17 1(1979)

- (13-1) "Design Control Document for the United States Advanced Pressurized Water Reactor" R1, Mitsubishi Heavy Industries, Ltd., August 2008
- (13-2) "Thermal Design Methodology", MUAP-07009-P (Proprietary) and MUAP-07009-NP (Non-Proprietary), May 2007.

- (15-1) Davidson, S. L. and Nuhfer, D. L., "VANTAGE+ Fuel Assembly Reference Core Report," WCAP-12610-P-A (Proprietary), June 1990.
- (15-2) Suzuta, T. and Teramae, T., "Large Break LOCA Code Applicability Report for US-APWR," MUAP-07011-P(R0), July 2007.

- (16-1) "US-APWR Fuel System Design Evaluation", MUAP-07016-P (Proprietary) and MUAP-07016-NP (Non-Proprietary), February 2008.

- (17-1) "FINDS: Mitsubishi PWR Fuel Assemblies Seismic Analysis Code", MUAP-07034-P (Proprietary) and MUAP-07034-NP (Non-Proprietary), March 2008.
- (17-2) "Proving Test on the Seismic Reliability for Nuclear Power Plant", Nuclear Power Engineering Test Center, March 1987
- (17-3) H. Akiyama et al., "Seismic Test and Analysis for PWR Reactor Core Internals", ASME PVP-1989 Vol.182, Seismic Engineering-1989 Design, Analysis, Testing and Qualification Methods

- (22b-1) Idaho National Engineering and Environmental Laboratory, SCDAP/RELAP5/MOD3.3 Code Manual MATPRO-A Library of Materials Properties for Light-Water-Reactor Accident Analysis, NUREG/CR-6150, Vol.4, Rev.2, January 2001
- (22b-2) Idaho National Engineering Laboratory, MATPRO-VERSION 11 (REVISION 2) A HANDBOOK OF MATERIALS PROPERTIES FOR USE IN THE ANALYSIS OF

LIGHT WATER REACTOR FUEL ROD BEHAVIOR, NUREG/CR-0497 TREE-1280,
REV.2, August 1981

- (22b-3) Idaho National Engineering Laboratory, MATPRO-VERSION 11 A HANDBOOK OF MATERIALS PROPERTIES FOR USE IN THE ANALYSIS OF LIGHT WATER REACTOR FUEL ROD BEHAVIOR, NUREG/CR-0497 TREE-1280, February 1979

- (23a-1) R.A.Dean, "Thermal contact conductance between UO₂ and Zircaloy 2", CVNA-127, May 1962

- (23b-1) Westinghouse Electric Company, IMPROVED ANALYTICAL MODELS USED IN WESTINGHOUSE FUEL ROD DESIGN COMPUTATIONS, WCAP-8720, October 1976

- (25-1) U.S.Nuclear Regulatory Commission, Regulatory Guide 1.126

- (28-1) K. Bakker et al, "Determination of a Porosity Correction Factor for the Thermal Conductivity of Irradiated UO₂ Fuel by means of the Finite Element Method", Journal of Nuclear Materials, 226, 1995, pp.128-143

- (28-2) Shimomura et al."US-APWR Fuel System Design Evaluation", MUAP-07016-P, MUAP-07016-NP, February, 2008, Mitsubishi Heavy Industries, Ltd.

- (28-3) "Final Report of High Burnup Rim Project (HBRP)", March, 2001, Central Research Institute of Electric Power Industry.

- (32-1) D. W. Brite et al, EEI/EPRI Fuel Densification Program Final Report, March 1975

- (38-1) J.J. Serna, et. al., "Experimental Observations on Fuel pellet Performance at High Burnup," Proceedings of the 2005 Water Reactor Fuel Performance Meeting, Kyoto, Japan,

- (38-2) S. Watanbe, T. Kido and Y. Arakawa, "Performance of M-MDA™ cladding in the commercial reactor up to 73GWd/tU," Proceedings of the 2008 Water Reactor Fuel Performance Meeting, Seoul, Korea, October 19-22, 2008

- (38-3) S. Watanbe, et. al., "Post irradiation examinations on 67-75GWd/t rods for confirmation of the integrity and appropriate performance of the claddings for future,".

ATTACHMENT 1

FILES CONTAINED IN CD 1

CD 1: "Attachment of Responses to RAI's 1, 9, 12 and 18 of NRC Requests in
ML082760492 (UAP-HF-08299 Rev.0)"
-Proprietary information

Contents of CD

<u>File Name</u>	<u>Size</u>	<u>Sensitivity level</u>
• ReadMe.pdf (pdf format)	108KB	Proprietary
• FINE inputs:		
<RAI 1b response>		
- us24eq_Gr2_gg2mxbu-strain.dat	94KB	Proprietary
- us24eq_Gr2_gu2mxbu-strain.dat	94KB	Proprietary
<RAI 9d response>		
- us24eq_Gr1_gg2mxbu-press.dat	94KB	Proprietary
- us24eq_Gr1_gg2mxp1-press.dat	94KB	Proprietary
- us24eq_Gr1_gg2mxp2-press.dat	94KB	Proprietary
- us24eq_Gr1_gu2mxbu-press.dat	94KB	Proprietary
- us24eq_Gr2_gu2mxp2-press.dat	94KB	Proprietary
- us24eq_Gr3_uu2mxp1-press.dat	94KB	Proprietary
- us24eq_Gr4_gg3mxbu-press.dat	138KB	Proprietary
- us24eq_Gr4_gg3mxp1-press.dat	138KB	Proprietary
- us24eq_Gr4_gg3mxp2-press.dat	138KB	Proprietary
- us24eq_Gr4_gg3mxp3-press.dat	138KB	Proprietary
- us24eq_Gr4_gu3mxbu-press.dat	138KB	Proprietary
- us24eq_Gr4_gu3mxp1-press.dat	138KB	Proprietary
- us24eq_Gr4_gu3mxp2-press.dat	138KB	Proprietary
- us24eq_Gr4_gu3mxp3-press.dat	138KB	Proprietary
<RAI 12 response>		
- usap_cy1_en48_nominal_10GW.dat	4KB	Proprietary
- usap_cy2_en48_nominal_30GW.dat	5KB	Proprietary
- usap_cy2_en48_nominal_50GW.dat	5KB	Proprietary
<RAI 18 response>		
- usap_tcl-tavmax.dat	4KB	Proprietary

- FINE outputs:

<RAI 1b response>

- us24eq_Gr2_gg2mxbu-strain.OUT	19MB	Proprietary
- us24eq_Gr2_gu2mxbu-strain.OUT	17MB	Proprietary

<RAI 9d response>

- us24eq_Gr1_gg2mxbu-press.OUT	3.1MB	Proprietary
- us24eq_Gr1_gg2mxp1-press.OUT	3.1MB	Proprietary
- us24eq_Gr1_gg2mxp2-press.OUT	3.1MB	Proprietary
- us24eq_Gr1_gu2mxbu-press.OUT	2.8MB	Proprietary
- us24eq_Gr2_gu2mxp2-press.OUT	2.8MB	Proprietary
- us24eq_Gr3_uu2mxp1-press.OUT	2.8MB	Proprietary
- us24eq_Gr4_gg3mxbu-press.OUT	4.5MB	Proprietary
- us24eq_Gr4_gg3mxp1-press.OUT	4.5MB	Proprietary
- us24eq_Gr4_gg3mxp2-press.OUT	4.5MB	Proprietary
- us24eq_Gr4_gg3mxp3-press.OUT	4.5MB	Proprietary
- us24eq_Gr4_gu3mxbu-press.OUT	4.0MB	Proprietary
- us24eq_Gr4_gu3mxp1-press.OUT	4.0MB	Proprietary
- us24eq_Gr4_gu3mxp2-press.OUT	4.0MB	Proprietary
- us24eq_Gr4_gu3mxp3-press.OUT	4.0MB	Proprietary

<RAI 12 response>

- usap_cy1_en48_nominal_10GW.OUT	62KB	Proprietary
- usap_cy2_en48_nominal_30GW.OUT	73KB	Proprietary
- usap_cy2_en48_nominal_50GW.OUT	73KB	Proprietary

<RAI 18 response>

- usap_tcl-tavmax.OUT	62KB	Proprietary
-----------------------	------	-------------